Experimental Assessment of the Internal Flow Behavior of Supercritical Carbon Dioxide

by

David Yang

Submitted to the Department of Aeronautics and Astronautics
in partial fulfillment of the requirements for the degree of

Masters of Science

at the

MASSACHUSETTS INSTITUTE OF TECHNOLOGY
[September 2014]
August 2014

Signature redacted

Author .....
Department of Aeronautics and Astronautics
August 22, 2014

Signature redacted

Certified by .....
Zoltán Spakovszky
Professor of Aeronautics and Astronautics
Thesis Supervisor

Signature redacted

Accepted by .....
Paulo C. Lozano
Associate Professor of Aeronautics and Astronautics
Chair, Graduate Program Committee

Experimental Assessment of the Internal Flow Behavior of Supercritical Carbon Dioxide

by

David Yang

Submitted to the Department of Aeronautics and Astronautics
on August 22, 2014, in partial fulfillment of the
requirements for the degree of
Masters of Science

Abstract

This thesis presents an experimental assessment of the internal flow behavior of supercritical carbon dioxide. The investigation focused mainly on assessing condensation onset during rapid expansion of CO_2 into the two-phase region. An experimental blowdown test-rig with a modular test section was developed with the capability of operating a converging-diverging nozzle with a wide range of charge conditions. The test-rig demonstrated repeatable results with relative errors of less than 1 percent.

An innovative method to measure the speed of sound through the use of Helmholtz resonators was developed and investigated. Shock tube experiments and static high pressure air tests in the blowdown facility were conducted to determine the viscous damping in the resonators. The results indicate that a Helmholtz resonator neck Reynolds number of 10^6 is required for underdamped response. The speed of sound measurement technique was demonstrated at relevent Reynolds numbers and at static conditions in air, showing promise for blowdown testing in S-CO_2.

Blowdown experiments were conducted in supercritical CO_2 from charge conditions both away and near the critical point to sonic conditions in the two-phase region. To determine whether there was condensation onset, static pressure measurements were compared to theoretical and numerical models. Numerical models utilized the Span-Wagner equation of state extrapolated into the two-phase region to characterize the metastable state. Away from the critical point, for operating conditions typically encountered in S-CO_2 compressor stages, condensation was not observed. Near the critical point, results were inconclusive and future work is proposed to provide more conclusive assessment of condensation near the critical region.

Thesis Supervisor: Zoltán Spakovszky
Title: Professor of Aeronautics and Astronautics

Acknowledgments

There are many people to whom I owe gratitude for their support during my time so far at MIT. First, I express my deepest gratitude towards my advisor, Prof. Zoltán Spakovszky for his guidance, enthusiasm, and mentorship - I would not have been able to complete this thesis without his support and deep knowledge of fluid dynamics.

I am also grateful for the guidance and knowledge offered by Dr. Claudio Lettieri. His knowledge of thermodynamics and numerics have helped me through the many challenges I encountered during my work at the GTL. I won't soon forget his support.

I also offer my thanks to James Letendre, for his help and guidance on the experimental test-rig - without it, I would not have been able to put it together myself. His knowledge of piping and electronics proved to be invaluable during the construction process.

I would also thank Dr. Eisaku Ito and Akihiro Nakaniwa of Mitsubishi Heavy Industries for their continued support of this project and their feedback during our meetings together. Their questions and comments were greatly appreciated and provided me with valuable insight into turbomachinery design.

To all my friends at the Gas Turbine Laboratory, throughout MIT and beyond: your support throughout my time in Boston made the journey much more enjoyable than I could have ever imagined and I would not be here without all of you. In particular, I would like to thank the close friends I have met at MIT: Sebastien, Bobby, Irene, Margaret, Marc, Remí, Steven, Julie Andrew, David C., and Louis - I am honored to have made your acquaintance and will not forget our time together. I would also like to thank my close friends back home in Texas: Michael, Ryan, Mike and Eric, without your support, I would not have even been in a position to make it here today.

Finally, I express my lifelong gratitude for my parents for their unwavering support. I am only the man I am today because of their guidance throughout my life. All that I have accomplished has been a direct result of their care, devotion and love.

Contents

List of Figures

List of Tables

Nomenclature

Acronyms

BT	Blackman-Tukey
CCS	Carbon capture and sequestration
CFD	Computational fluid dynamics
CP	Critical point
CO_2	Carbon dioxide
HR	Helmholtz resonator
EOS	Equation of state
NIST	National Institute of Standards and Technology
RANS	Reynolds Averaged Navier Stokes
S-CO_2	Supercritical carbon dioxide
SDE	Spectral density estimation
ST	Shock tube
SW	Span-Wagner
TF	Transfer function

Symbols

A	Cross-sectional area
β	Reduced frequency
β_p	Volumetric thermal expansion coefficient

c	Speed of sound
c_p	Heat capacity at constant pressure
c_v	Heat capacity at constant volume
h	Specific enthalpy
HT	Heat transfer coefficient
f	Frequency
γ	Ratio of specific heats
Gr	Grashof number
κ	Thermal conductivity
k	Wave number
L	Duct length
μ	Dynamic viscosity
M	Mach number
$\dot{m}$	Mass flow rate
m_s	Isentropic temperature exponent
n_s	Isentropic exponent
Nu	Nusselt number
$\dot{Q}$	Heat flux rate
p	Pressure
ρ	Density
ϕ_{yu}	Cross density spectrum
ϕ_u	Power density spectrum
Pr	Prandtl number
R	Gas constant
Re	Reynolds number
s	Specific entropy
SA	Surface area
T	Absolute temperature
τ_{cl}	Condensation time scale ratio
u	Specific internal energy

V Volume

w Angular frequency

Z Compressibility factor

Subscripts

c Critical condition

D Diameter

L Axial length

t Stagnation quantity

Chapter 1

Introduction

1.1 Background

In recent years, global warming and rising carbon dioxide emissions have come to the forefront of public debate, with many thoughts on the best method to reduce future CO_2 emissions. Despite increased efforts to mitigate emissions through new technologies and the increased use of renewable energy sources, carbon based fuels remain the primary source of energy throughout the world, especially for power generation. Coal use accounts for roughly 25% of the world's energy supply and is responsible for 40% of carbon emissions; it remains the primary source of energy due to its wide-scale availability and relatively low cost [2]. With renewable energy sources projected to only account for roughly 20% of power generation by 2040 in the U.S [3], methods of carbon dioxide emission reduction from power generation will be increasingly important. One method of CO_2 emission mitigation that has been proposed is carbon capture and sequestration (CCS). CCS refers to the process of capturing CO_2 from carbon fuel combustion before it is released into the atmosphere, subsequently compressed to high pressure in order to reduce its specific volume and then stored, usually within aquifers or coal beds deep underground. The CO_2 is usually compressed to high enough pressures to reach the supercritical state, referring to the state where surface tension vanishes and the boundary between the liquid and gas phases disappears. In this supercritical state, CO_2 has a density with a similar magnitude to

that of the liquid state while expanding to fill the volume it is enclosed in, such as in the gaseous phase. The primary issue with CCS lies with the large quantity of CO_2 that must be compressed and the pressures it must be compressed to, for CCS to be viable. Energy requirements for CCS are generally around 20% of a power plant's output. Due to the significant proportion of a power plant's energy required for CCS, efficiency improvements can lead to dramatic reductions in operating costs and increase the viability of CCS.

Recently supercritical CO_2 (S-CO_2) has also received renewed interest as the primary operating fluid for electric power plant cycles, especially for nuclear and solar applications. S-CO_2 has unique thermodynamic properties that allow power cycles utilizing S-CO_2 to have thermal-to-electric conversion efficiencies up to 50% greater than conventional Brayton cycles [4]. With renewable energy costs representing the primary barrier to widespread use, further improvement of S-CO_2 turbomachinery design is essential and requires knowledge about the behavior of S-CO_2 within internal flow environments.

1.2 Motivation

CCS systems require CO_2 to be compressed to extremely high densities close to 1000 kg/m^3, requiring compressor outlet pressures in excess of 200 bar. In order to reach pressures of this magnitude, multiple compressor blocks are required with intercoolers situated in between the blocks to control maximum temperature rise and improve system efficiency. Due to the location of the critical point of CO_2 (73.7 bar, 304.1 K), the inlet conditions of each compressor block move successively closer to the critical point through the compression process. In particular, during compressor testing near the critical point, efficiencies below the design value and stability issues were observed [5]. These operability issues led to the establishment of a safety boundary for compressor operating points, which limits the performance that can be achieved by these CO_2 compressors. The location of the safety line, compressor blocks, and the critical point of CO_2, plotted on a T-s diagram, can be found in Fig 1-1. Due

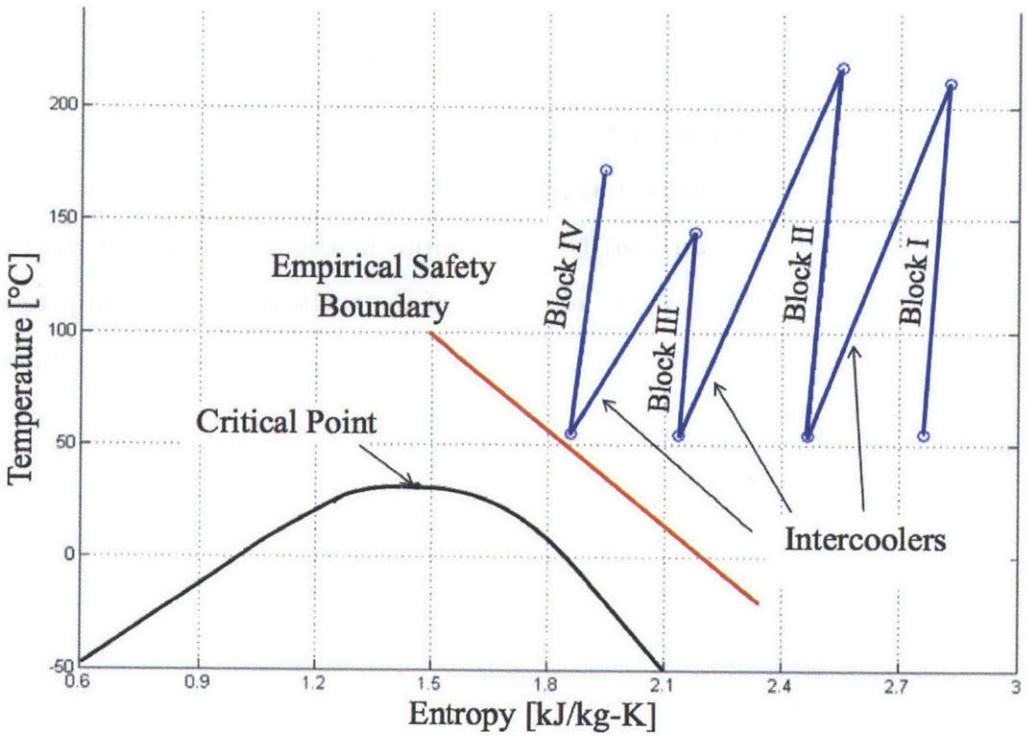

Figure 1-1: Compressor block operating points in relation to the critical point of CO_2.

to the lack of experimental data available during full-scale compressor operation and limited understanding of internal flow behavior of CO_2 , the root cause of the observed performance issues could not be identified. Further improvement of state of the art CO_2 compressors requires a rigorous investigation of the various real gas effects of CO_2 in high speed internal flow environments.

1.3 Problem Statement

The observed compressor stability and performance degradation issues were hypothesized to be caused by either aerodynamic issues or the presence of condensation within the compressor stages.

Current design tools of supercritical CO_2 compressors rely around CFD packages utilizing CO_2 equation of state models to provide the thermodynamic properties. While state of the art equation of state models for CO_2 are accurate within 1%, they are based on static measurements of CO_2 at equilibrium conditions [6]. However,

flow within turbomachinery is highly unsteady with dynamic changes in thermodynamic properties. The large gradients in flow variables inherent to turbomachinery are exacerbated near the critical point, where the thermodynamic properties of a fluid vary greatly with temperature and pressure. In this region, small errors in the calculation of the fluid state can lead to large errors in the estimation of inlet-to-outlet performance metrics, such as the efficiency of the turbomachinery compressor. Experimental assessment of the dynamic behavior of these equation of state models for internal flow applications is required in order to characterize design changes in turbomachinery performance with sufficient accuracy.

Additionally, due to the nature of the entropy generation process, it is generally preferable to carry out the compression of gases at as low of a temperature as possible since temperature has a direct effect on the amount of entropy produced for a given process [7]. The saturation temperature of CO_2 at the pressures generally encountered in CO_2 gas compressors ranges from 290 K to 304 K. Temperatures in this range are reached within compressor stages after the intercoolers when the internal flow is expanded over the leading edge of the compressor blades, leading to the possibility of localized condensation. Condensation is problematic for the operation of turbomachinery as it can lead to a reduction in machine efficiency, operating range, and affect stage matching characteristics [5]. In order to determine operating point limitations for CO_2 compressors, it is necessary to investigate the possibility of condensation in high speed internal flow situations near the two-phase region.

This thesis focuses on experimentally assessment of supercritical CO_2 condensation during rapid internal flow expansion into the two-phase region near and away from the critical point. New findings presented in the thesis include experimental static pressure measurements in a converging-diverging nozzle with comparisons to both numerical and theoretical estimates to determine whether or not condensation occurs during flow expansion to sonic conditions in the two-phase region. The knowledge of condensation possibility and the conditions at which it may occur, may allow S-CO_2 compressors to operate at lower temperatures and closer to the CP, increasing turbomachinery efficiency.

1.4 Review of Previous Work

1.4.1 Expansion of CO_2 Near the Critical Point

Despite the recent renewal in interest in CCS, there is a lack of experimental studies assessing the validity of current real-gas models for use in rapidly expanding flows near the critical point of CO_2. Theoretical and computational studies of the evolution of the isentropic exponent, n_s, and compressibility factor, Z, found that gradients in n_s are much greater near the critical point compared to away from the critical point. These studies also concluded that the magnitude of the n_s gradient had important consequences on turbomachinery efficiency and stability margin [5]. Additionally, the studies noted that further away from the critical point, n_s of supercritical CO_2 does not change much for an isentropic expansion and resembles the specific heat ratio for an ideal gas in the total-static isentropic compressible flow relations [5].

1.4.2 High Speed Internal Flow Condensation of CO_2

While there have been numerous studies concerning the condensation of supercritical steam in high speed internal flow environments, such as steam turbines [1, 8], there have been very few studies conducted for supercritical CO_2 condensation. Studies of high speed supercritical steam condensation have found that condensation tends to occur rapidly at a point well below the saturation temperature [1]. The fluid that exists below the saturation temperature/pressure but in the gaseous phase occupies a space that is known as the metastable state. Accurate modeling of fluid condensation in high speed flow relies on knowledge of the metastable region limits, and there is a lack of experimental measurements documenting the properties of CO_2 in the this state. An example of rapid condensation of steam in a converging-diverging nozzle experiment can be seen in Fig 1-2. The experiment was conducted with saturated steam at a stagnation pressure and temperature of 1 bar and 288.1 K respectively. These studies have also found that, due to the rapid nature of condensation, a large amount of heat is released into the flow within a very small space. This heat release

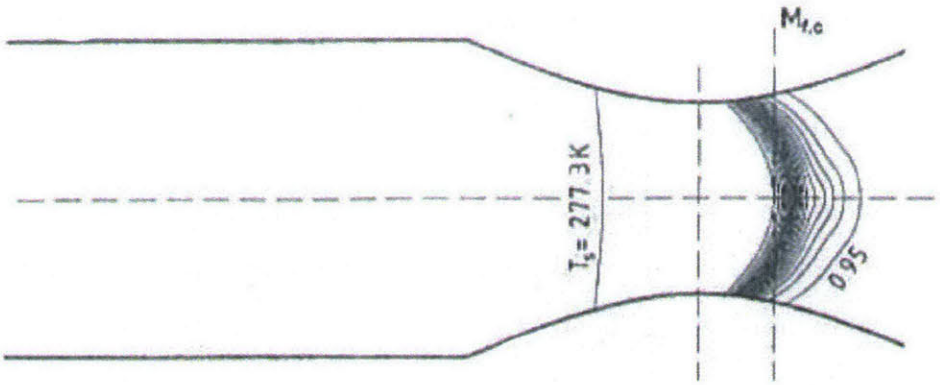

Figure 1-2: Isocontours of condensate mass fraction in relation to the saturation line for steam in a converging-diverging nozzle, taken from [1].

causes a significant rise in static pressure in the flow [1]. As a part of the present project, two-phase numerical calculation with steam as the working fluid was carried out in order to verify the pressure rise due to condensation as observed in [1]. The simulation was conducted using a converging-diverging nozzle and charge conditions were set such that the saturation line would be situated at the nozzle throat. The resulting pressure ratio distribution along the nozzle can be seen in Fig 1-3.

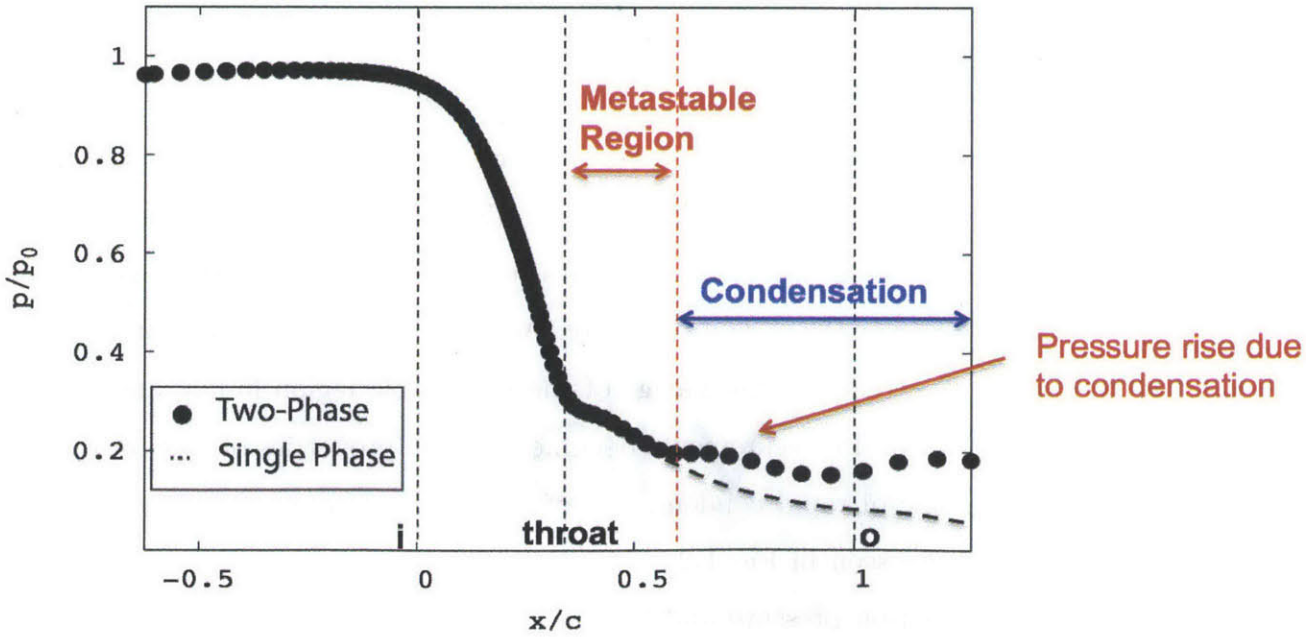

Figure 1-3: Pressure rise due to rapid condensation of steam compared to isentropic expansion in a converging-diverging nozzle. (Courtesy of Dr. C. Lettieri)

Additionally, it has been shown that a condensation onset of 0.1% moisture can be detected through static pressure measurements due to the condensation heat release for low pressure CO_2 [9].

Studies focusing solely on supercritical CO_2 condensation have been limited to theoretical analysis with focus on condensation timescales [5] due to the lack of experimental data of the metastable region of CO_2. The study found that far away from the critical point, condensation of supercritical CO_2 around compressor blades was inhibited due to the amount of time required for condensate particles to form, despite the fact that thermodynamic conditions were favorable for condensation; essentially, given the convection time of the fluid, the CO_2 did not stay in the condensation-favorable region long enough for condensation to occur [5].

1.5 Technical Approach

The lack of experimental data on CO_2 condensation and its metastable state led to the need for an experimental test-rig with the ability to measure the thermodynamic properties of CO_2 during rapid expansion into the two-phase region. Experimental assessment was carried out through a series of blowdown tests through a converging-diverging nozzle. The blowdown tests allowed static pressure measurements during expansion of CO_2 to sonic conditions. Through manipulation of the charge conditions, the tests allowed for measurements of the gaseous, supercritical, metastable and two-phase states of CO_2. Experimental measurements were compared to theoretical models and numerical calculations to determine if condensation occured during the expansion process.

1.6 Goals and Objectives

The primary goal of this thesis is to experimentally investigate the onset of condensation during rapid expansion of S-CO_2 into the two phase-region away and near the critical point. The specific objectives of the work are:

1. Design, build and demonstrate a laboratory scale blowdown test-rig to experimentally assess the internal flow behavior during rapid expansion of S-CO_2

2. Demonstrate the capability of the use of Helmholtz resonators to experimentally measure speed of sound

3. Compare experimental measurements of static pressure in the converging nozzle to both theoretical and numerical estimates so as to assess whether condensation occurs both away and near the critical point

4. Define the limits of safe CO_2 compressor operation

The potential payoffs include developing a novel, non-intrusive method to measure the speed of sound during fluid expansion for use in future experiments and to determine the limits of supercritical CO_2 compressor operating points, which may lead to a reduction in compressor operating costs and operability issues.

1.7 Key Contributions

The primary contributions of this thesis can be summarized as follows:

1. Demonstration of a blowdown test-rig that has the ability to reach a wide range of charge conditions, representative of the inlet conditions in current and future CO_2 compressors and to experimentally investigate rapid expansion of CO_2.

2. Measurement of nozzle static pressure distributions for rapid expansion of S-CO_2 into the two-phase region both near and away from the critical point. Comparison of experimental measurements to theoretical and numerical estimates show close agreement (within 3%) and condensation was not observed for expansion to sonic conditions away from the critical point.

3. Demonstration that numerical calculations utilizing SW EOS near the critical point show good agreement (within 1%) with experimental measurements outside of the two-phase region.

4. Experimental demonstration of speed of sound measurement through the use of a Helmholtz resonator at high Reynolds numbers and at static conditions. Several impediments to this measurement method were investigated; the primary issue that must be addressed is the attenuation of acoustic signals due to discontinuities in the cross-sectional area distribution along the flow path.

While the work focuses on supercritical CO_2 as the primary working fluid, the test-rig, methods of measurement and analysis tools are applicable to any real gas.

1.8 Thesis Organization

This thesis is organized as follows. Chapter 2 provides a description of the thermodynamic equation of state models for CO_2, with a focus on the Span-Wagner model. Non-equilibrium condensation is described with a focus on the condensation timescales. Numerical treatment of the metastable state is then described. Chapter 3 describes the design and development of the blowdown test-rig with a focus on sizing and heat transfer. Designs of the nozzle test section and inlet are also described. Chapter 4 describes a method for speed of sound measurement through the use of Helmholtz resonators. The HR design process is described with a focus on viscous damping. Chapter 5 provides an experimental assessment of the HR speed of sound measurement method with high pressure air. Signal processing methods are described and compared. Chapter 6 provides an experimental assessment of CO_2 condensation through comparison of static pressure measurements with theoretical and numerical models. Measurements from blowdown tests both away and near the critical point are provided and discussed. Chapter 7 provides concluding remarks and recommendations for future work.

Chapter 2

Numerical Modeling of Supercritical Carbon Dioxide

A large portion of the turbomachinery design process currently leverages numerical tools with the understanding that the numerical tools are able to model flow through turbomachinery with sufficient fidelity. Numerical simulation fidelity is dependent on a variety of factors, including accurate modeling of flow physics, fluid chemistry, and how a fluid's thermodynamic properties change when one property is perturbed. Knowledge of the fluid's thermodynamic behavior is provided to the numerical solver by what is known as the fluid's equation of state (EOS), such that the equation of state used and its accuracy is of utmost importance to numerical solver accuracy. The most common equation of state is the ideal gas equation, commonly used for fluids such as air. High pressure and supercritical CO_2 do not follow the ideal gas equation, because of real gas effects. The real gas equations of state are the subject of extensive research and many different real gas EOSs have been developed. Both general equations applicable to a wide array of real gases and specific equations tailored for specific fluids exist. Equations of the former type include the Benedict, Webb, and Rubin EOS (BWRS), Redlich-Kwong EOS (RKS), and Lee-Kesler EOS, with an extension by Plöcker, Knapp and Prausnitz (LKP) [10]. Of these EOS models, the LKP EOS performs the best for CO_2 at pressures from 50 to 250 bar away from the critical point [10], with errors of up to 8% in the primary thermodynamic properties near

the critical point [5], which is too large for turbomachinery design purposes. Specific equations of state reduce the error of general models such as the LKP EOS. The most recent and accurate EOS for CO_2 is the Span-Wagner equation of state [5].

2.1 The Span-Wagner Equation of State Model

The Span-Wagner EOS is formulated as a fundamental equation explicit in Helmholtz free energy as opposed to a pressure-explicit formulation as many of the older real gas EOS's [11]. The free energy equation was fitted to experimental measurements accumulated from selected sources of the thermal properties (density, pressure, temperature) in the single phase region and liquid-vapor saturation curve, speed of sound, specific isobaric heat capacity, isochoric heat capacity, specific enthalpy, and specific internal energy. In order to minimize the errors in formulation of the equation of state of CO_2 , the authors removed any experimental data sets that did not meet a minimum level of uncertainty. To retain accuracy near the critical point, several terms in the equation of state were dedicated to fitting the EOS to the data sets representing the critical point. While the SW EOS is empirical in nature for many of the thermodynamic properties, it still obeys the fundamental equations of fluid chemistry and physics [11]. The resulting equation of state is reported to be accurate within 0.05% in the density, 1% in the speed of sound, and 1.5% in the isobaric heat capacity, all of which are within their experimental uncertainty [6].

The main deficiency of the SW model for use in turbomachinery applications is that the experimental measurements the model is based on were conducted under static conditions. There is a lack of information to verify the accuracy of the model within a highly dynamic environment, with rapid changes in thermodynamic properties and accelerations. In addition, the model does not capture the metastable region that arises during rapid expansion through the saturation line. Both of these deficiencies limit the usefulness of the model for advanced design of supercritical CO_2 compressors and must be addressed for future turbomachinery design with CO_2 as the working fluid.

2.2 Condensation in High-Speed Flow

The occurance of condensation during high speed flow (M > 0.3) in external and internal environments, has been studied extensively in the literature with various fluids, particularly water steam. As noted in Section 1.4.2, condensation in high speed choked nozzle flow generally occurs at temperatures very suddenly far below the saturation temperature of the fluid. Condensation under these conditions is known as non-equilibrium condensation. In contrast, equilibrium condensation occurs at a fluid's saturation temperature and pressure. For non-equilibrium condensation, the region of a fluid that is below its saturation conditions without liquid particles is known as the metastable region. The differences between equilibrium and non-equilibrium condensation is represented on a pressure-temperature diagram in Figure 2-1. Path A to B represents an isentropic expansion at a temperature and pressure above that of the fluid's saturation line. Path B to C represents a fluid's thermodynamic process during equilibrium condensation, while path B to D represents the fluid's thermodynamic process during non-equilibrium condensation and represents the fluid's metastable state [12]. Fluid state E corresponds to the fluid's state after undergoing condensation from the metastable state. The difference in temperature between C and E represents the irreversibility as a result of non-equilibrium condensation. One of the main factors determining whether a fluid undergoes equilbrium or non-equilibrium condensation is the ratio of the time required for nucleation of liquid particles to the time a fluid particle resides in the region below the saturation temperature and pressure. The nucleation time is defined by

$$t_n = \frac{1}{J_{max} V}, \tag{2.1}$$

where V is the volume of fluid below saturation and J_{max} is the maximum normalized rate of nucleation. The normalized rate of nucleation is defined by

$$J = \left[\sqrt{\frac{2\sigma}{\pi m^3}} \frac{\rho_v^2}{\rho_l} \right] e^{\left(-\frac{\Delta G^*}{kT}\right)} \tag{2.2}$$

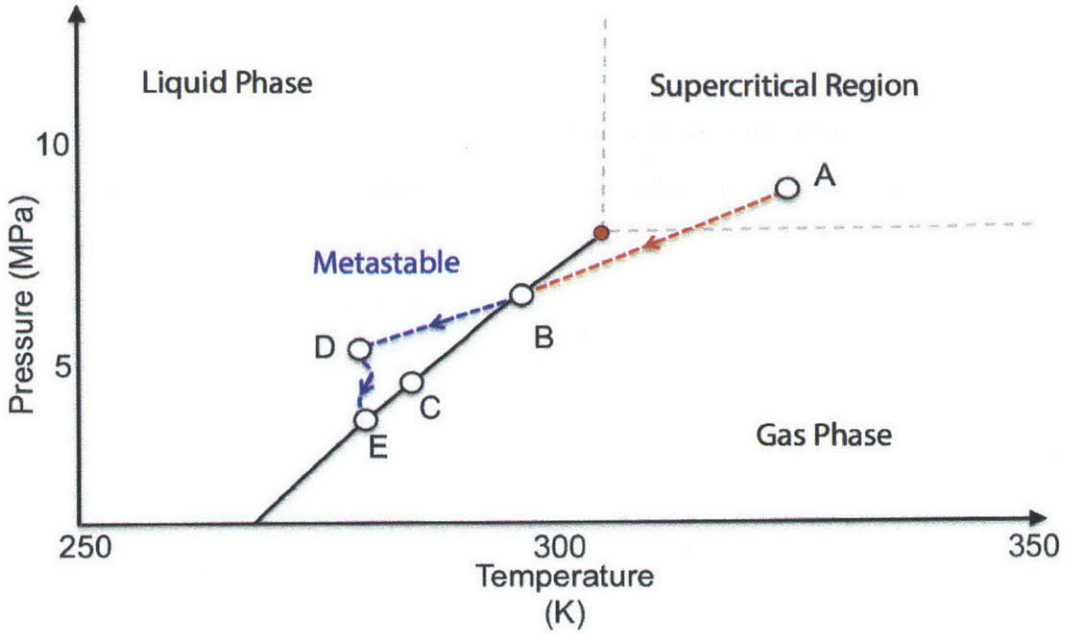

Figure 2-1: Pressure-temperature diagram showing difference between non-equilibrium and equilibrium condensation. (Courtesy of Dr. C. Lettieri)

$$\Delta G^* = \frac{4}{3}\pi r^{*2}\sigma$$

$$r^* = \frac{2\sigma}{\rho_t \left[g(p_v, T) - g(p_s, T)\right]}.$$

The residence time is defined as

$$t_r = \frac{l}{c_{avg}}, \tag{2.3}$$

where l refers to the spatial extent of the condensation region and c_{avg} is the average flow velocity. The definition of l for flow over an airfoil and flow within a nozzle is graphically represented in Figure 2-2. The ratio of the two timescales, τ_{cl}, becomes

$$\tau_{cl} = \frac{t_r}{t_n} = \frac{J_{max} V l}{c_{avg}}. \tag{2.4}$$

For equilbrium condensation, $\tau_{cl} >> 1$ at a fluid's saturation temperature and pressure, indicating that the fluid has ample time to nucleate while within the two-phase region. In contrast, $\tau_{cl} << 1$ during non-equilibrium condensation, indicating that a fluid does not have enough time to nucleate while within the two-phase region.

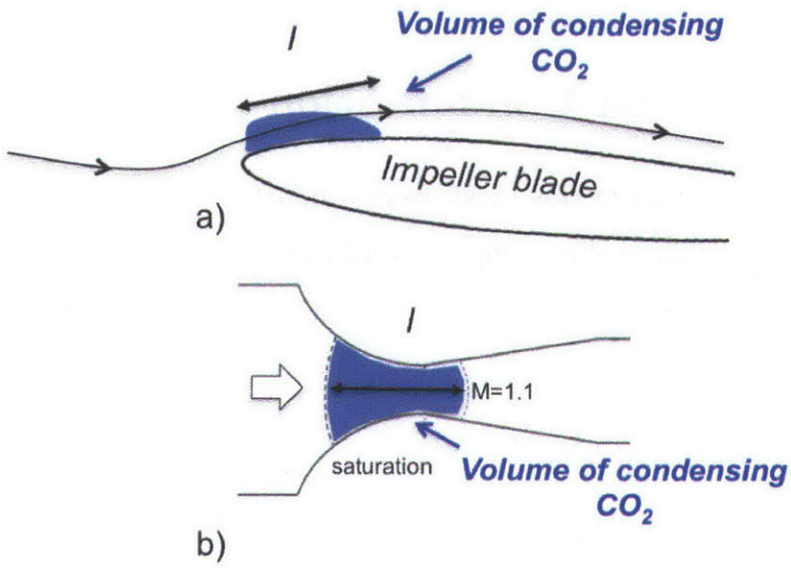

Figure 2-2: Graphic representation of condensation length scale and volume. (Courtesy of Dr. C. Lettieri)

For external flow conditions such as as in Fig 2-2 (a), $\tau_{cl} << 1$ suggests that a fluid passes through a region below saturation conditions without condensation. For internal flow situations such as shown in Figure 2-2(b), a fluid may continue to expand past its saturation point without condensing if τ_{cl} remains far below unity. However, the further the flow expands past its saturation point, t_n decreases until τ_{cl} becomes large enough for condensation to occur, such that a large amount of condensation can occur at once. The temperature at which this rapid condensation occurs, or point of maximum subcooling is known as the Wilson point [12]. Due to the thermodynamic losses associated with condensation, knowledge of the location of the Wilson point is important for the design of turbomachinery operating in the two-phase region. The location of the Wilson point varies depending on each specific application, making it impractical to determine its location through experimentation during turbomachinery design. While the Wilson point may be determined on an application-to-application basis numerically, the accuracy of numerical calculations depends on an accurate model of a fluid's thermodynamic properties in the metastable state. While there are numerous metastable tables available for water steam, to the author's knowledge, there are no such tables for CO_2.

2.3 Numerical Modeling of Supercritical CO_2 : Expansion and Condensation

All numerical calculations in this thesis were conducted with ANSYS CFX 14. This solver is based on a finite-volume approach utilizing an implicit compressible formulation with second order spatial discretization. The two equation $k - \omega$ shear stress transport (SST) turbulence model was used to close the Reynolds-averaged Navier-Stokes (RANS) equations. Calculations were all steady-state as will be discussed in Section 3.4. The thermodynamic properties of CO_2 were provided by the NIST formulation of the SW EOS, called REFPROP [13], in the form of lookup tables to increase computational speed. The lookup table implementation was validated with comparision to experimental measurements. Systematic refinement of the tables revealed that if table entries were resolved below 0.1 K in temperature and 0.1 bar in pressure, there were no appreciable differences in computational accuracy. Due to the lack of thermodynamic properties of CO_2 in the metastable region, CO_2 metastable properties were created by extrapolating thermodynamic properties near the two-phase region into the two-phase region with a cubic extrapolation scheme. The extrapolation technique is similar to what is employed by the IAPWS-97 steam property database and shown to work well for small extrapolations into the two-phase region [5]. An example of the extrapolation scheme for enthalpy as a function of temperature and pressure can be seen in Figure 2-3, which shows the smoothing of enthalpy across the saturation line into the two-phase region. The extrapolation scheme is shown to perform well away from the critical point later in the thesis. Near the critical point, extrapolation is challenging due to the sharp gradients in thermodynamic properties at the critical point. Determination of the proper treatment of the metastable properties in this region requires experimental validation.

Due to the high speeds present within the turbomachinery and relatively high density of the S-CO_2, the Reynolds number routinely reached magnitudes on the order of 10^7, which required careful grid refinements near the end walls to accurately capture the viscous effects for all calculations.

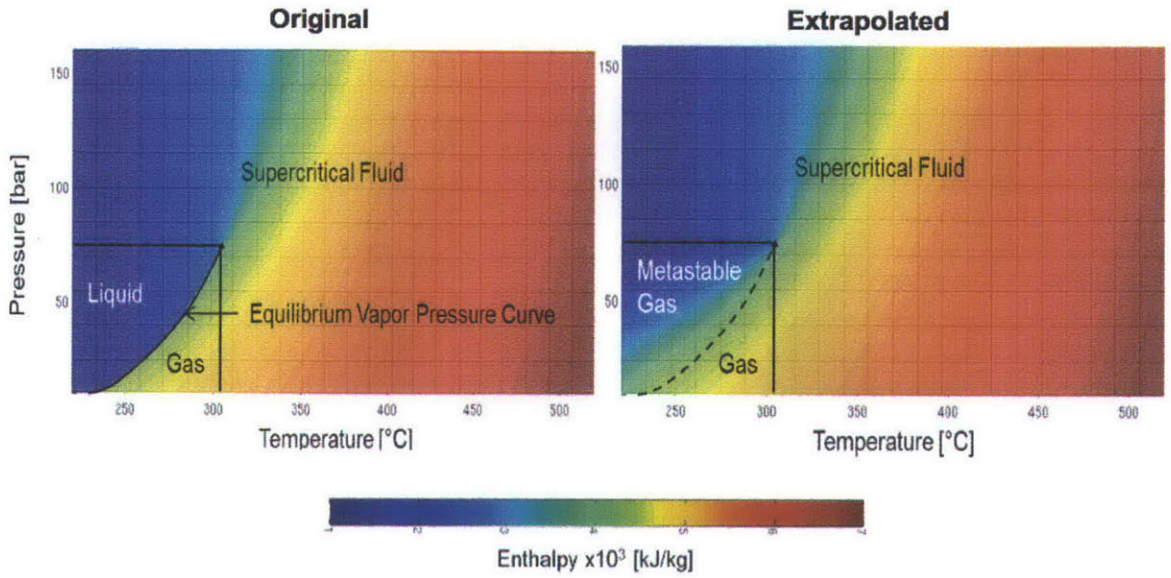

Figure 2-3: Extrapolation of enthalpy into the two-phase region of carbon dioxide. (Courtesy of N. Baltadjiev)

Chapter 3

Experimental Test-Rig Design and Setup

Investigation of the possibility of condensation of supercritical CO_2 during rapid expansion required the design of an experimental test-rig to measure thermodynamic properties during the expansion process. The main goals of the test-rig were to:

1. Achieve expansion of supercritical CO_2 to sonic conditions, similar to the rapid expansion of CO_2 around the leading edge of compressor blades,
2. Allow for high-fidelity, high frequency measurements of two thermodynamic properties during the expansion process to sonic conditions,
3. Ability to reach a wide-range of charge conditions, covering the pressures and temperatures of typical compressor inlet operating conditions.

3.1 Test-Rig Design and Benefits

A laboratory scale blowdown experiment was deemed as the simplest test-rig to meet all of the above goals. The designed test-rig consists of five main elements:

- Commercially available CO_2 bottles to supply the experiment with the working fluid

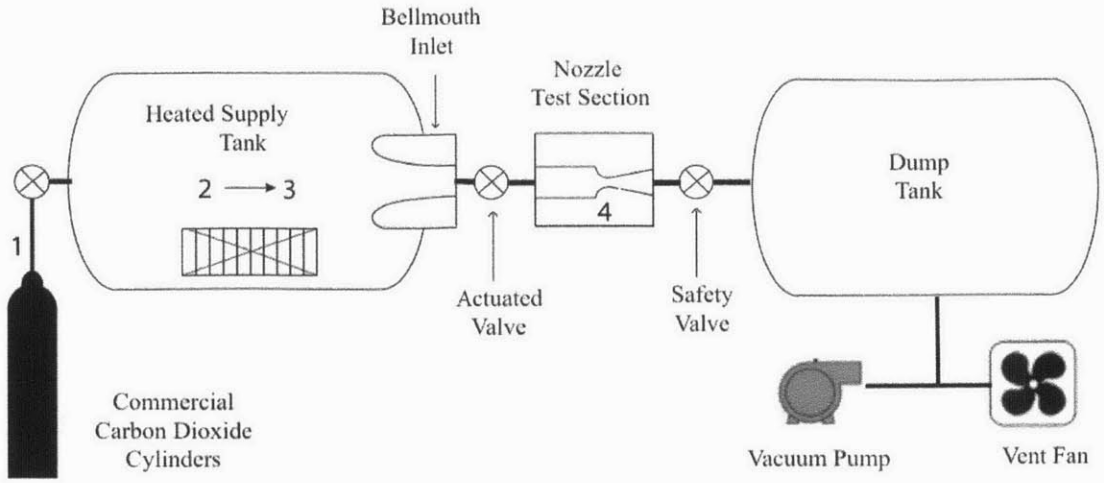

Figure 3-1: Diagram of experimental test-rig. (Courtesy of Dr. C. Lettieri)

- A heated charge tank
- A modular nozzle test section consisting of a converging-diverging nozzle with multiple measurement ports
- Bellmouth inlet to ensure uniform inflow to the nozzle test section
- Dump tank to control nozzle exit pressure

A diagram of the test-rig and connections between the main components are depicted in Figure 3-1. The test-rig allows for control of the charge conditions over a wide range of temperatures and pressures within the supercritical region of CO_2. The charge pressure and temperature are set by controlling the quantity of CO_2 used to fill the charge tank (density control) and amount of heat addition into the charge tank (temperature control). Limitations on charge temperature and pressure are set by the operating limits of the charge tank and test section. Charge conditions (pressure, temperature) are monitored with a high fidelity pressure transducer and type-K thermocouple positioned inside of the charge tank.

As noted previously, characterization of two thermodynamic properties is required to calculate the thermodynamic state of supercritical CO_2 using the SW EOS, while characterization of three thermodynamic properties allows for full characterization of

Blowdown Test	Charge Pressure (bar)	Charge Temperature (K)
1	68.1	315
2	74.6	315
3	89.1	315
4	93.7	315

Table 3.1: Charge conditions for typical blowdown tests.

the thermodynamic state without use of any EOS. Due to the high pressure environment of the experimental test-rig, it was determined that the simplest thermodynamic measurements were of static pressure and speed of sound along the nozzle contour. The speed of sound measurement method is described in Chapter 4. The initial design of the nozzle test section focused on conducting the measurement of speed of sound and static pressure in the converging section, where the Mach number is below unity. However, due to the modular nature of the test section, it allows for future experiments to be conducted with alternate focii.

3.2 Thermodynamic Description of CO_2 During A Typical Blowdown Test

Experimental assessment of the rapid expansion of CO_2 was conducted with four blowdown tests, each with different charge conditions. A wide range of charge conditions were chosen to examine the differences between rapid expansion both away and near the critical point. The charge conditions chosen for the blowdown tests are tabulated in Table 3.1.

The thermodynamic state of the CO_2 during test 4, from fill bottles to nozzle throat, is shown on a temperature-entropy diagram in Fig 3-2. The thermodynamic process of the CO_2 during a typical blowdown test is as follows:

- Liquid CO_2 is transferred from commercially available CO_2 bottles at 62.1 bar and 295 K (1) to the charge tank until the charge tank is at 49.7 bar and 287 K (2) in a constant enthalpy (isenthalpic) process

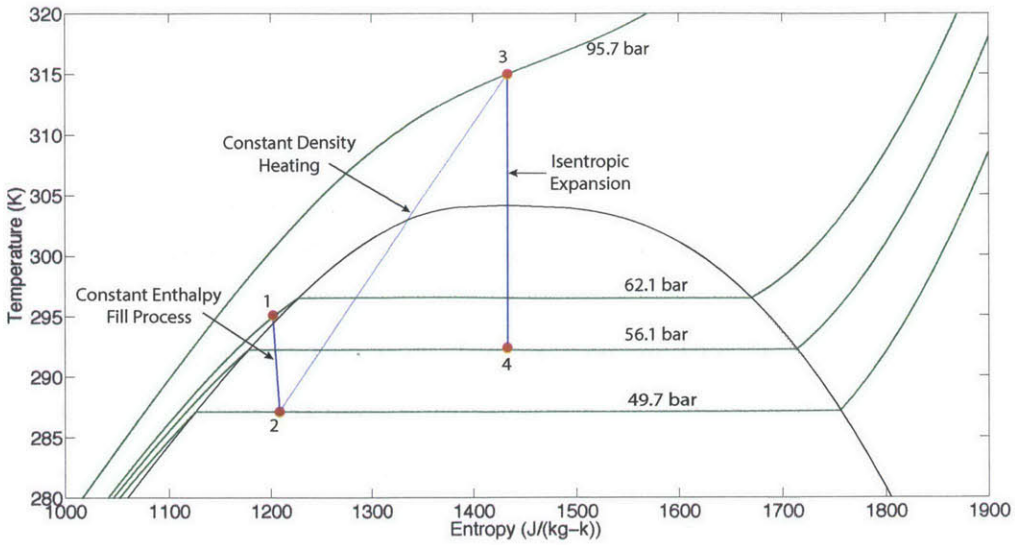

Figure 3-2: T-s diagram of experimental test-rig, from fill to nozzle throat condition for critical point expansion test.

- The filled charge tank is heated until it reaches a pressure of 95.7 bar and temperature of 315 K (3) in a constant density (isochoric) process
- CO_2 in the charge tank is expanded isentropically in the nozzle test section to a throat pressure of 56.1 bar at sonic conditions (4)

Measurements available during the blowdown process from (3) to (4) include:

- Temperature and pressure within the charge tank
- Static pressure and speed of sound along the nozzle in the converging section

With the SW EOS and the available measurements, it is possible to characterize the full thermodynamic state of CO_2 during blowdown and inside the charge tank, as long as the process it outside of the metastable region. At the nozzle throat, it is possible to determine the isentropic exponent without use of the SW EOS due to knowledge of the Mach number and the use of the isentropic relations developed in [5]. The equation of interest is repeated here,

$$\frac{p_t}{p} = (1 + \frac{n_s - 1}{2} M^2)^{\frac{n_s}{n_s - 1}}. \tag{3.1}$$

Knowledge of the mach number, charge pressure, and static pressure allows for direct calculation of the isentropic exponent, n_s.

3.3 Test-Rig Design Considerations

The experimental blowdown test-rig design was conducted with several considerations in mind in order to simplify the experimental data analysis while meeting the goals stated in Section 1.6. Specific design considerations included:

- Test-rig size such that multiple blowdown tests could be conducted with minimal charge tank pressure loss
- Determination whether blowdown could be characterized as isothermal or adiabatic for model analysis purposes
- Ensuring that a sufficient number of fluid flow through times occurred during each blowdown test such that each test could be considered quasi-steady
- Nozzle inlet designed such that uniform flow entered the converging-diverging nozzle to ensure the flow could be approximated as one-dimensional
- Nozzle test section designed to allow for the placement of Helmholtz resonators along the nozzle contour for measurement purposes
- The need for acoustic actuators inside of the charge tank to excite the Helmholtz resonators
- The need for a mixing motor inside of the charge tank to ensure there was no stratification in charge tank fluid
- Nozzle-charge tank interface designed to allow for the routing of a thermocouple and electrical wires through a high pressure (greater than 100 bar) differential. The electrical connections and thermocouple were required to allow for measurement of pressure and temperature of the charge tank fluid during testing,

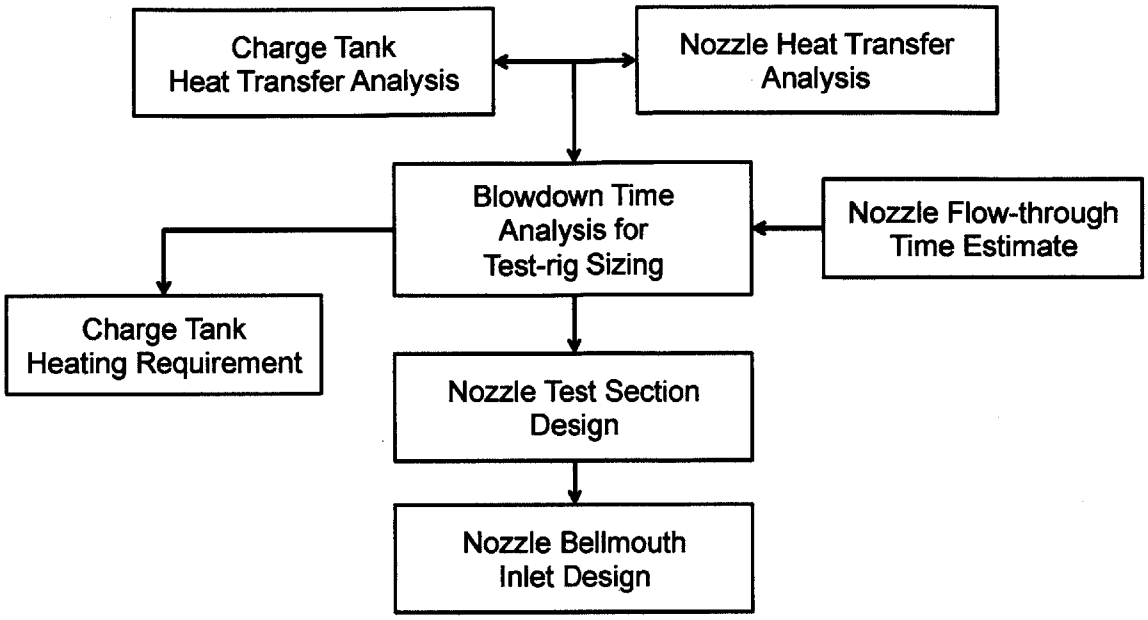

Figure 3-3: Experimental test-rig design process

as well as allow for the use of the mixing motor and acoustic actuators within the charge tank.

The test-rig design process is summarized in the flow chart in Fig 3-3.

3.4 Test-Rig Sizing

Test-rig sizes (charge tank volume, nozzle throat diameter) were set to ensure that the blowdown process considered quasi-steady, which was defined as minimal charge tank pressure drop (1%) during each individual blowdown test. The required blowdown test time was set by the flow through time of the nozzle test section. With a flowthrough time on the order of 10^{-4}seconds and a minimum of 500 flowthrough times per test to ensure that the flow had enough time to reach a quasi-steady state, the minimum test time was calculated to be 0.5 seconds. Calculation of 1% charge tank pressure drop time first required a heat transfer analysis to be conducted to determine if the blowdown process was adiabatic or isothermal.

3.4.1 Heat Transfer Analysis

Analysis of heat transfer into the experimental test-rig required apriori knowledge of the means of heat transfer possible during blowdown. Investigation of the test-rig and its insulation revealed two main locations of distinct heat transfer: natural convection within the charge tank due to temperature changes, and forced convection in the nozzle due to the high-speed flow. Each of these two locations were investigated independently. Quantiative limits on heat transfer for the isothermal and adiabatic processes were set by the number of transfer units (NTU) that characterizes the blowdown process [14]. The definition of NTU is shown in Eq 3.2 where HT is the heat transfer coefficient of the charge tank, SA is the surface area of the charge tank, c_v is the constant-volume heat capacity of the fluid contained within the charge tank and $\dot{m}$ is the mass flow out of the charge tank.

$$NTU = \frac{(HT)(SA)}{c_v \dot{m}} \tag{3.2}$$

A blowdown process with $NTU < 0.7$ can be considered adiabatic while $NTU > 7$ indicates an isothermal blowdown process [14].

3.4.1.1 Charge Tank Heat Transfer

The heat transfer coefficient of the charge tank was calculated from the definition of the Nusselt number,

$$HT = \frac{Nu_D \kappa}{D}, \tag{3.3}$$

where Nu_D is the Nusselt number based on tank diameter, D is the diameter of the tank, and κ is the thermal conductivity of the enclosed fluid. Numerous empirical heat transfer equations exist in literature for the natural convection Nusselt number within an enclosed, cylindrical space, similar to the shape of most pressure vessels; the equation chosen was Eq 3.4 [15]. Eq 3.4 is empirical in nature and the limits of its use are:

- $0.5 < \frac{L}{D} < 2.0$

- $5.0 < Pr < 80000$
- $8.0x10^5 < Ra_D < 4.0x10^{10}$

$$Nu_D = 0.524 Ra_D^{1/4} \tag{3.4}$$

Where Ra_D is the Rayleigh number based on diameter of the enclosed fluid. The formulation of Ra_D is

$$Ra_D = Gr_D Pr \qquad Gr_D = \frac{g\beta_p(T_{wall} - T_{fluid})D^3}{\nu^2}, \tag{3.5}$$

where Gr_D is the Grashof number based on diameter, Pr is the Prandtl number of the enclosed fluid, g is the gravitational constant, β_p is the volumetric thermal expansion coefficient, T_{wall} is the tank wall temperature, T_{fluid} is the temperature of the enclosed fluid, and ν is the kinematic viscosity of the enclosed fluid. The above assumes the following:

- The enclosed fluid is uniform throughout at any given time (bulk fluid assumption)
- The tank wall temperature remains constant over time (isothermal tank walls)
- Tank modeled as vertical cylinder with hemisphere terminations for surface area calculation

Additionally, due to the fact that the fluid contained within the charge tank decreases in temperature during the blowdown process, it was necessary to calculate the temperature and update NTU of the charge fluid over time during blowdown (seen in Eq 3.5). Calculation of the temperature change of the charge fluid during blowdown required the additional assumptions:

- Blowdown process considered quasi-steady
- Tank volume of 0.4 m^3 and nozzle throat diamter of 5 mm
- Nozzle throat contiuously choked

- Nozzle throat n_s and Z equal to charge tank values

With these assumptions, conservation of mass and energy could be applied to the charge tank during the blowdown process,

$$\frac{\partial \rho_t}{\partial t} = -(\frac{2}{1+n_s})^{\frac{n_s+1}{2(n_s-1)}} \frac{A}{V} \sqrt{n_s Z_t R T_t \rho_t}, \tag{3.6}$$

$$\frac{d}{dt}(\rho_t V u_t) = -\dot{m} h_{M=1} + \dot{Q}, \tag{3.7}$$

where ρ_t is the density of enclosed fluid at any given time, A is the area of the nozzle throat, V is the volume of the charge tank, Z_t is the compressibility factor of enclosed fluid. R is the gas constant of CO_2, $\dot{m}$ is the mass flow rate through the nozzle throat, and $\dot{Q}$ is the heat flux rate into the charge tank due to natural convection. $\dot{Q}$ is calculated from Eq 3.3 and the definition of the heat transfer coefficient such that,

$$\dot{Q} = \frac{(HT)(T_{wall} - T_{fluid})}{dt}. \tag{3.8}$$

Eqs 3.6, 3.7 and 3.8 were numerically intergrated with respect to time to yield charge tank fluid temperature and pressure for a range of L/D of the charge tank from 1 to 10 during blowdown. From the calculated tank fluid temperature and pressure histories, the NTU time history was calculated for blowdown times ranging from 0 to 20 seconds. The resulting NTU history is plotted in Fig 3-4.

Fig 3-4 shows that the blowdown process can be considered adiabatic for up to 2 seconds, well within the required test time of 0.5 seconds.

3.4.1.2 Nozzle Heat Transfer

Similar to the calculation of the charge tank heat transfer coefficient, the forced convection heat transfer coefficient calculation utilized empirical equations. Few forced convection equations exist for flow through nozzles in the literature, however many exist for straight duct flow. To utilize the available relations, the following assumptions were made:

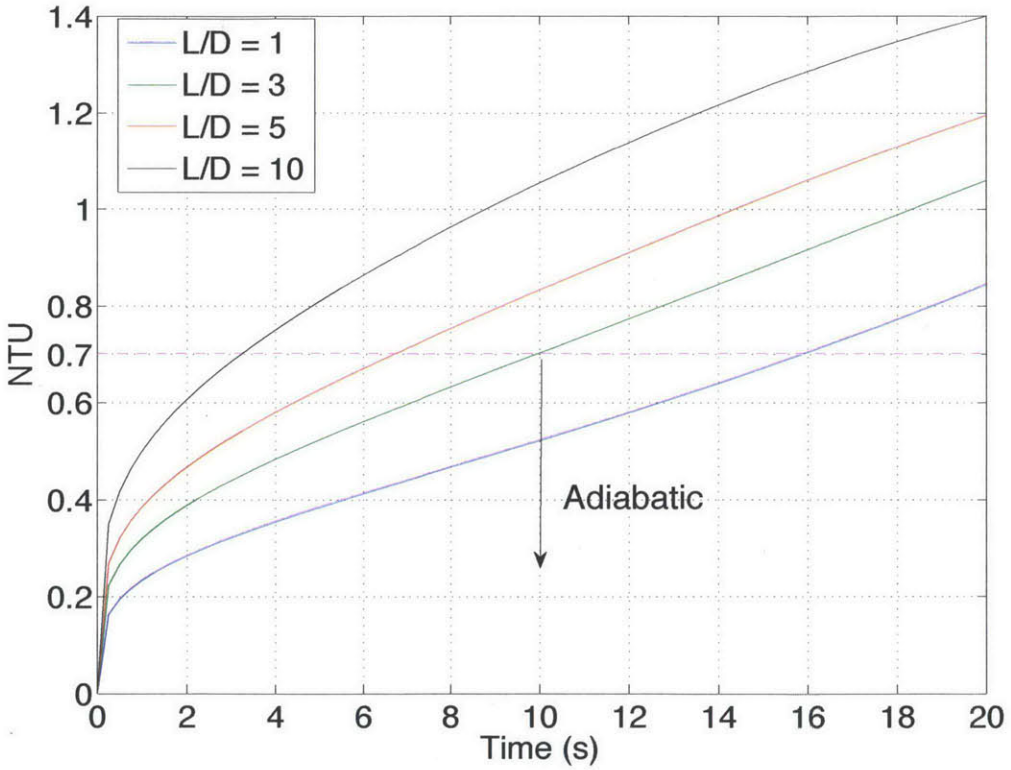

Figure 3-4: NTU of charge tank as a function of slenderness ratio and blowdown time.

- The nozzle geometry was modeled by a straight circular duct with equal length and wetted area,
- Flow within straight pipe duct treated as uniform.

Calculation of nozzle test conditions with Eq 3.1 and the SW EOS indicated that flow within the nozzle had a maximum Reynolds number of 10^7 and a maximum Prandtl number of 300. Due to the high Reynolds number, the flow in the straight pipe model was assumed to be turbulent. An appropriate empirical equation for the Nusselt number for turbulent flow within a straight pipe can be found in [16]:

$$Nu_D = \frac{(\xi/8)Re_D Pr}{K_1 + K_2(\xi/8)^{1/2}(Pr^{2/3} - 1)} \tag{3.9}$$

$$K_1 = 1 + 3.4\xi \qquad K_2 = 11.7 + 1.8Pr^{-1/3}$$

$$\xi = \frac{1}{(1.83ln(Re_D) - 1.64)^2}$$

The above equations assume:

- Fully-developed flow
- Turbulent flow
- Isothermal walls
- Constant thermodynamic property values of flow within duct

The range of applicability of the equations are:

- $10^4 < Re_D < 5x10^6$
- $0.5 < Pr < 2000$

While the Reynolds number of the flow under investigation was higher than the given limits, Eq 3.9 was still used to provide an order of magnitude estimate for the heat transfer within the nozzle. The Nusselt number and resulting NTU of the flow within the nozzle were evaluated using the minimum, maximum and average Reynolds and

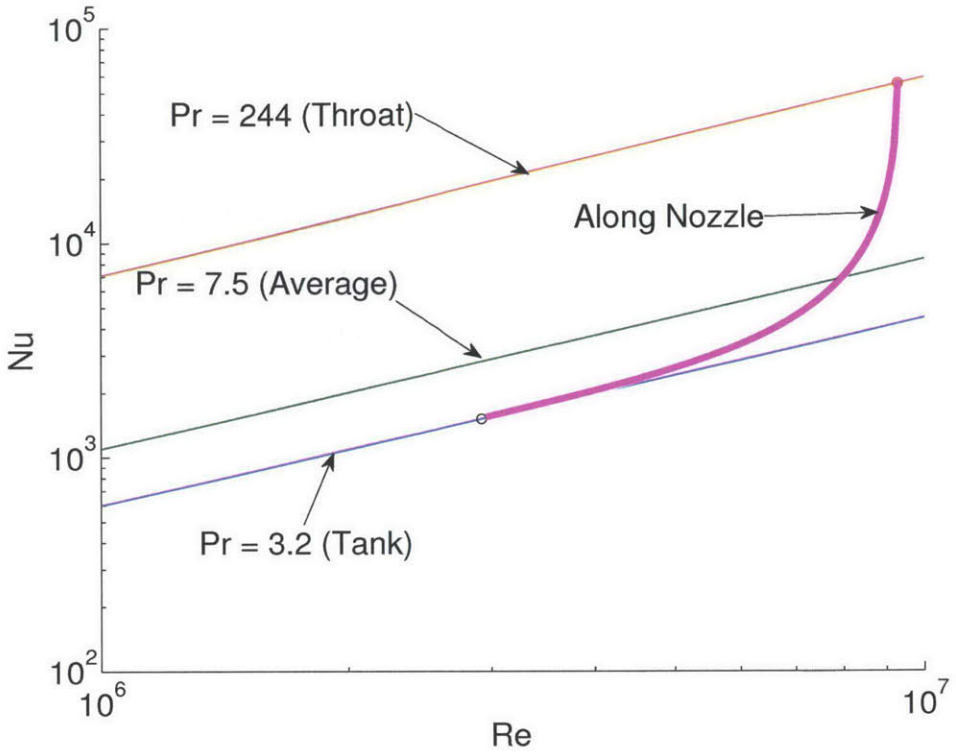

Figure 3-5: Nusselt number of straight pipe model using thermodynamic properties along actual nozzle.

Prandtl numbers calculated within the nozzle. The Nusselt number of flow using the thermodynamic properties found along the nozzle during blowdown is plotted in Fig 3-5. NTU values of the straight pipe model using the minimum, maximum, and average thermodynamic conditions in the calculated nozzle flow were found to be 0.002, 0.578, and 0.007 respectively. With NTU always below 0.7 and the results of Section 3.4.1.1, the blowdown process was considered adiabatic when calculating the blowdown time of the test-rig.

3.4.2 Blowdown Time Analysis

The primary variables that controlled whether the blowdown process could be considered quasi steady were mass capacitance and mass flow from the charge tank. The physical parameters that were associated with these variables were charge tank volume and nozzle throat diameter respectively. Mass capacitance and out flow also

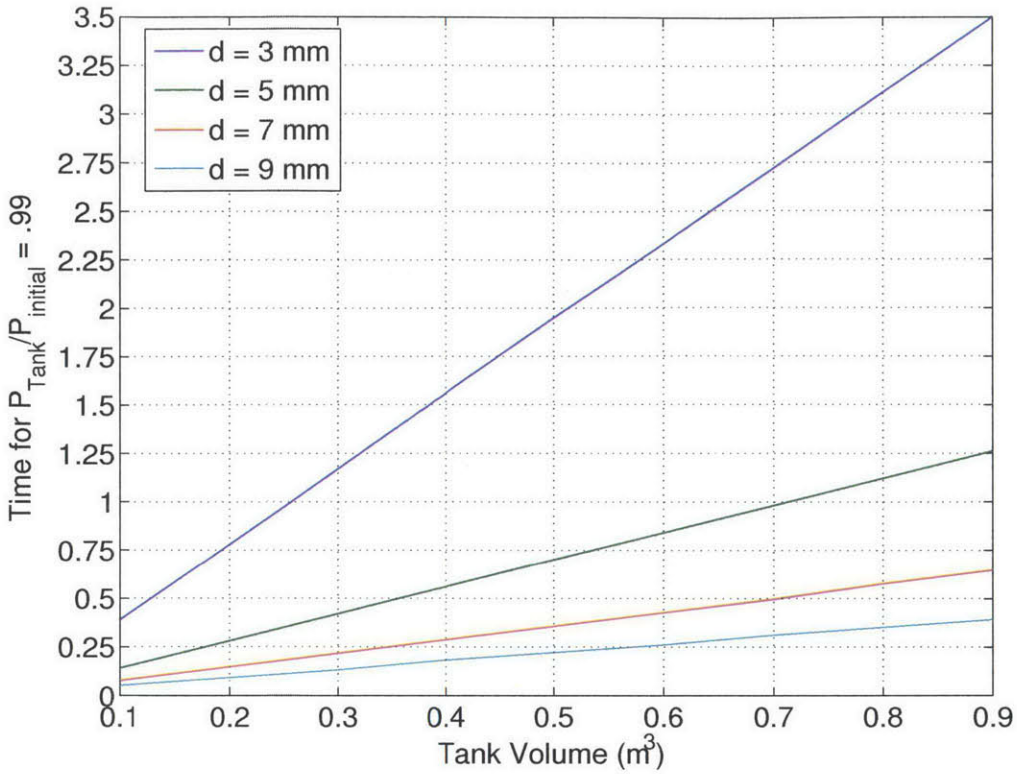

Figure 3-6: Time for 1% charge tank pressure drop as a function of nozzle throat diamter and charge tank volume.

control the number of tests that could be conducted for a single fill process. The performance metric used to quantify the ratio of mass capacitance to mass outflow was the time for charge tank pressure to drop one percent. Calculation of charge tank pressure during blowdown was done using Eqns 3.6 and 3.7, with $\dot{Q} = 0$ since the blowdown process was concluded to be adiabatic. The time for charge tank pressure to drop 1% for charge tank volumes of 0.1 m^3 to 0.9 m^3 and nozzle throat diameters of 3 mm to 9 mm are computed in Fig 3-6.

Combined analysis of Fig 3-6 and available commercial options yielded a charge tank volume of 0.44 m^3 and nozzle throat diameter of 5 mm, allowing for a 1% pressure drop time of 0.65 seconds, above the required 0.5 seconds for testing.

3.5 Nozzle Test Section and Bellmouth Section Design

The design of the nozzle test section and bellmouth focused on achieving desirable aerodynamic characteristics while limited by the measurement requirements, safety requirements, and manufacturing constraints. Addtionally, to maintain the modular nature of the test section, an actuated valve was placed in between the bellmouth and test sections to control flow. Placement of the valve introduced flow area discontinuities and placed additional constraints on the test-section design.

3.5.1 Bellmouth Section Design

Goals for the bellmouth design were the following:

- Allow for routing of electrical cables from inside charge tank to outside through pressure differential,
- Induce uniform flow into the nozzle test section. Primary sources of nonuniformity include significant velocity gradients (total pressure) or flow separation.

The bellmouth section is attached directly to the charge tank through a threaded opening, with part of the bellmouth inside of the charge tank and part of it outside of the tank. Due to the high pressures inside of the charge tank, the size of the opening was limited to 50 mm. As a result of the limited size of the charge tank opening, the primary constraint on the design process was designing a bellmouth contour of sufficient aerodynamic efficiency while allowing for enough space for the electrical cable routing duct. Bellmouth design has been studied in the literature with an effective design being that of an elliptical contour [17]. The bellmouth design used was a double radius design, which closely mimiced an elliptical contour. To ensure that the design was of sufficient efficiency without flow separation or overspeed bubbles along the contour, a numerical calculation of flow through the bellmouth was conducted with ANSYS CFX. The Mach number distribution along the bellmouth

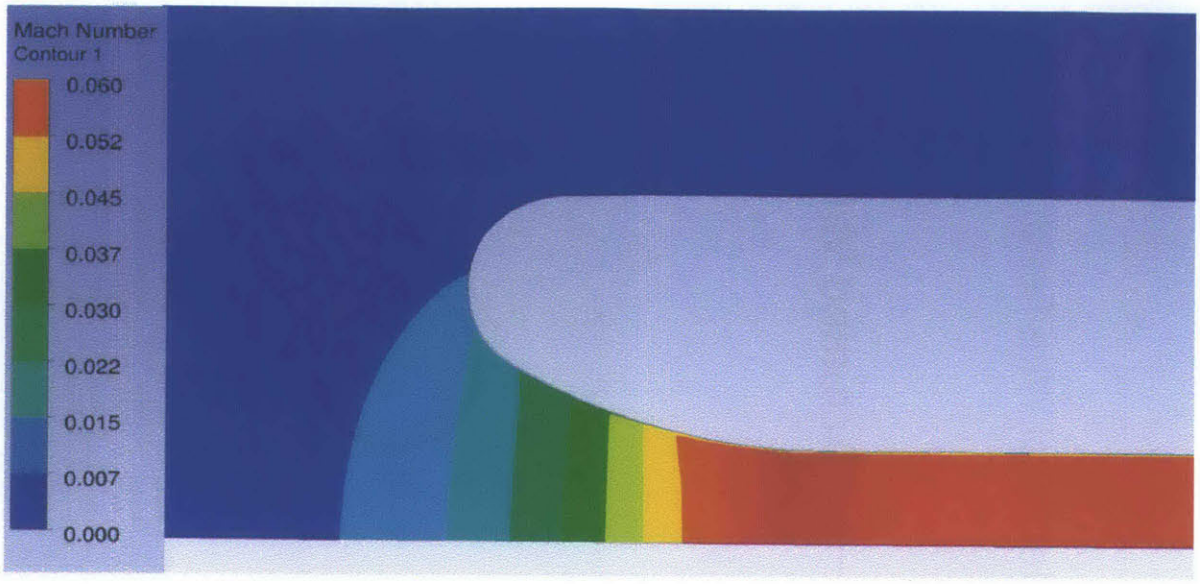

Figure 3-7: Mach number distribution around double radius bellmouth design.

contour is shown in Fig 3-7, which shows no flow separation or overspeed along the contour, with a uniform Mach number distribution through the inlet.

A duct connecting the part of the bellmouth inside of the charge tank and the part outside of the charge tank was added to allow for routing of the electric wiring required for the mixer motor, acoustic actuators, pressure transducer in the charge tank, and charge tank thermocouple. The final bellmouth technical drawing is shown in Fig 3-8.

3.5.2 Nozzle Test Section Design

Goals for the nozzle test section design were the following:

- Ensure any flow non-uniformities generated as a result the flow area discontinuity caused by the actuated valve were mixed out by the entry to the converging nozzle

- Generate quasi 1-D flow through the converging nozzle, with straight Mach contours

The main constraint on nozzle test section design was manufacturing capability, primarily bore depth. To ensure uniform flow enters the converging nozzle section, the

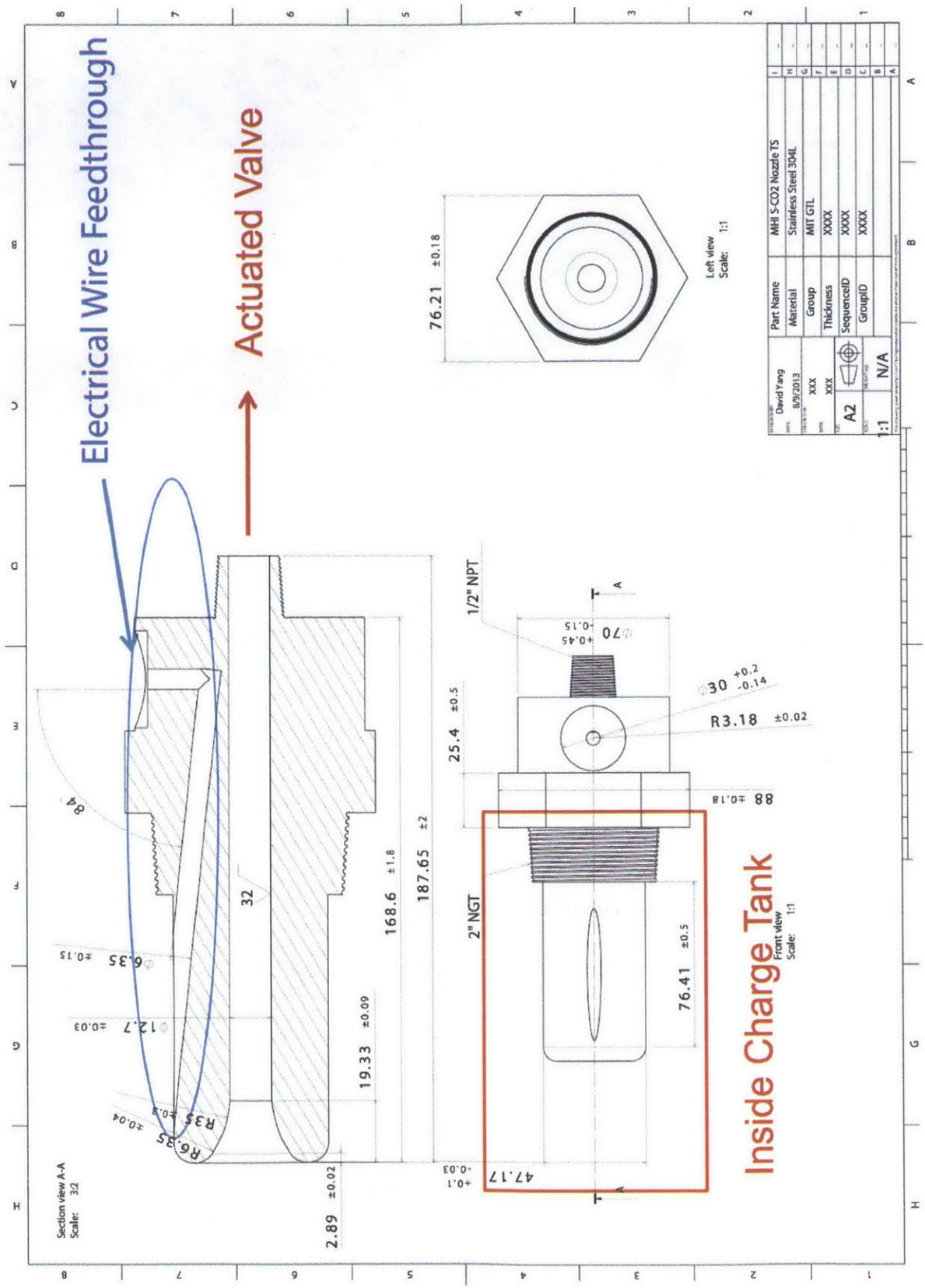

Figure 3-8: Technical drawing of bellmouth inlet duct.

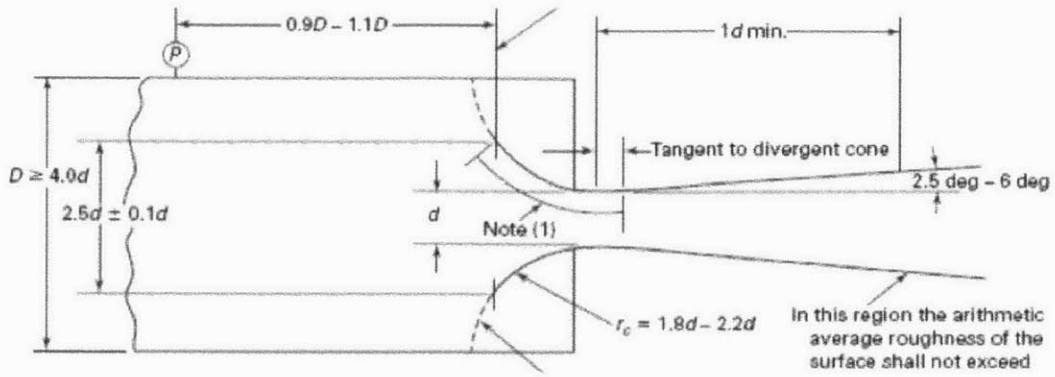

Figure 3-9: Geometry for converging-diverging nozzle.

length to diameter ratio of the straight duct upstream of the converging nozzle was set to ten to mix out any flow non-uniformities before the flow enters the converging section. Due to the length of the upstream duct, the converging nozzle contour was limited to simple designs as a result of manufacturing constraints. The geometry for the converging-diverging nozzle was obtained from the ASME standard for venturi nozzles to ensure the contour was of sufficient aerodynamic efficiency. The design consists of a single radius converging section and a conical diverging section with constant angle [18]. Fig 3-9 shows the geometry used. The pressure transducers were uniformly distributed in the axial direction along the converging nozzle contour. Pressure measurement locations and reference numbers are depicted in Fig 3-10. Measurement location 0 was positioned further upstream of the converging nozzle to avoid any upstream influence caused by the sharp corner. Aerodynamic performance of the ASME design was assessed through CFX. The Mach number distribution for choked flow in the converging-diverging nozzle can be seen in Fig 3-11. Pressure measurement locations are shown in black[1]. The numerical calculation shows that the simple radius converging section yields curved Mach contours, indicating the existence of 2-D flow in the nozzle. The numerical simulation also indicated the presence of oblique shocks within flow in the conical diverging section for supersonic flow, shown in Fig 3-12. Due to focus of the blowdown tests on the converging section and the added complexity required to eliminate the oblique shocks, the diverging section geometry

[1]There are 3 measurement ports for additional pressure transducers positioned in the diverging section.

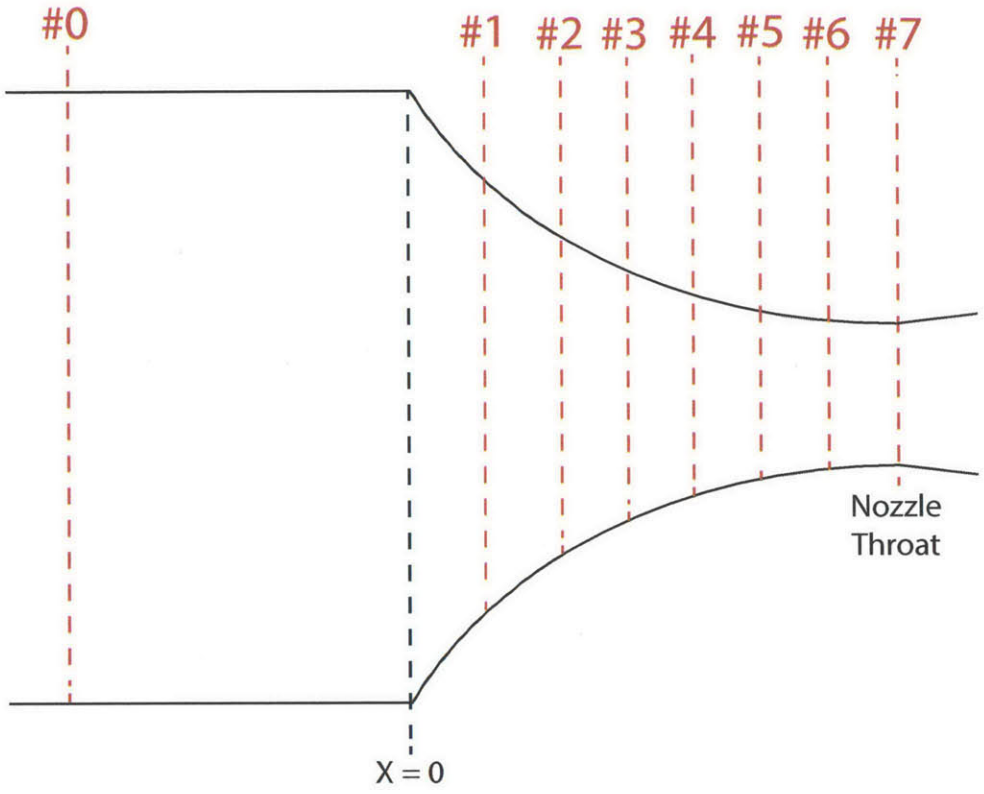

Figure 3-10: Pressure measurement locations and reference numbers

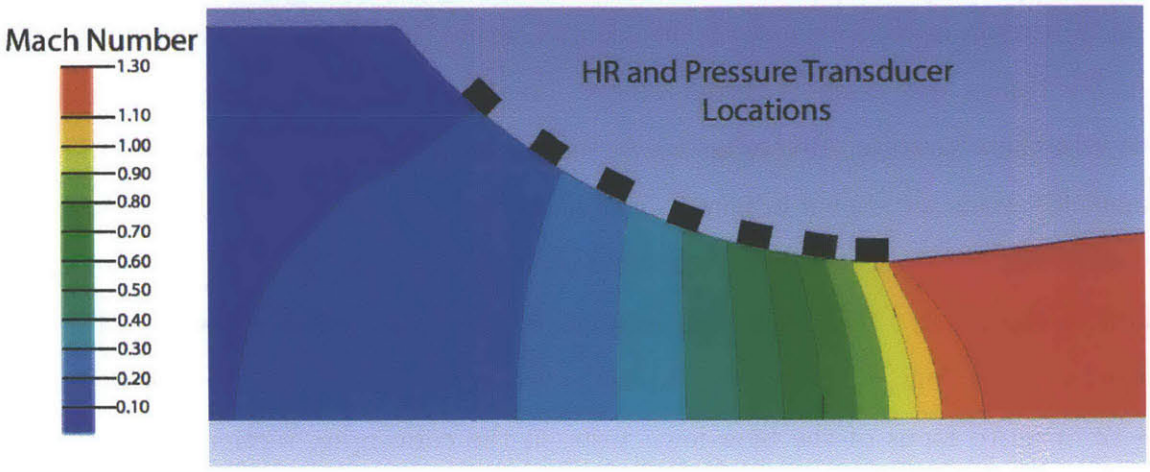

Figure 3-11: Mach number distribution in converging-diverging nozzle.

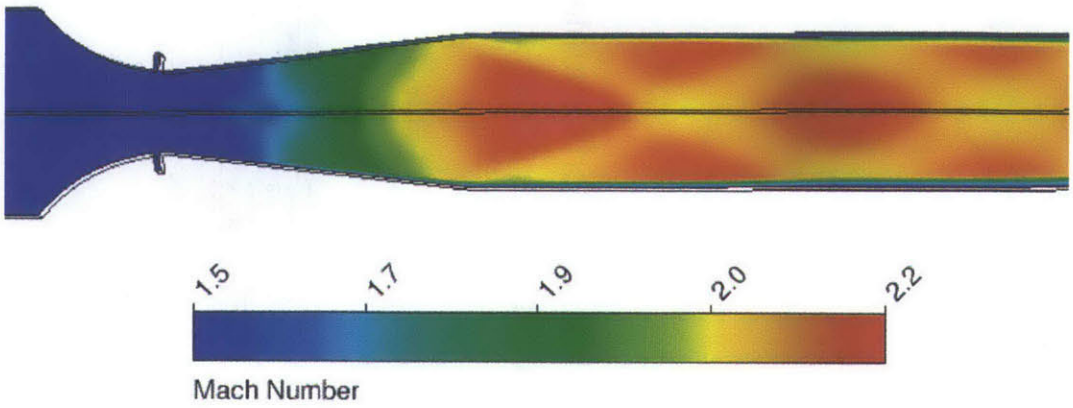

Figure 3-12: Oblique shocks present in nozzle diverging section. (Courtesy of Dr. C. Lettieri)

was unchanged for the final design. Other geometries were investigated in order to attempt to achieve 1-D flow in the converging section, however manufacturing constraints led to the single radius converging nozzle to be adopted for the final design. The final nozzle test section technical drawing is shown in Fig 3-13.

3.6 Experimental Test-Rig Components

The experimental test rig consists of identical charge and dump tanks, each with a capacity of 440 liters, pressure rating of 170 bar, and temperature rating of 375 K. The tanks were built with carbon steel according to ASME high pressure vessel standards and pressure tested by the manufacturer. A safety blowoff was built into each tank in the event of an overpressure. Both tanks were held to steel stands by nylon straps to both ensure they did not move during testing and to provide a torque to the tanks during assembly. The charge tank stand was bolted to the ground while the dump tank stand was attached to rails to allow for a variable amount of space between the tanks in order to allow for additional sections or instrumentation. Charge tank heating was applied by 12 heater tapes wrapped around the tank in a

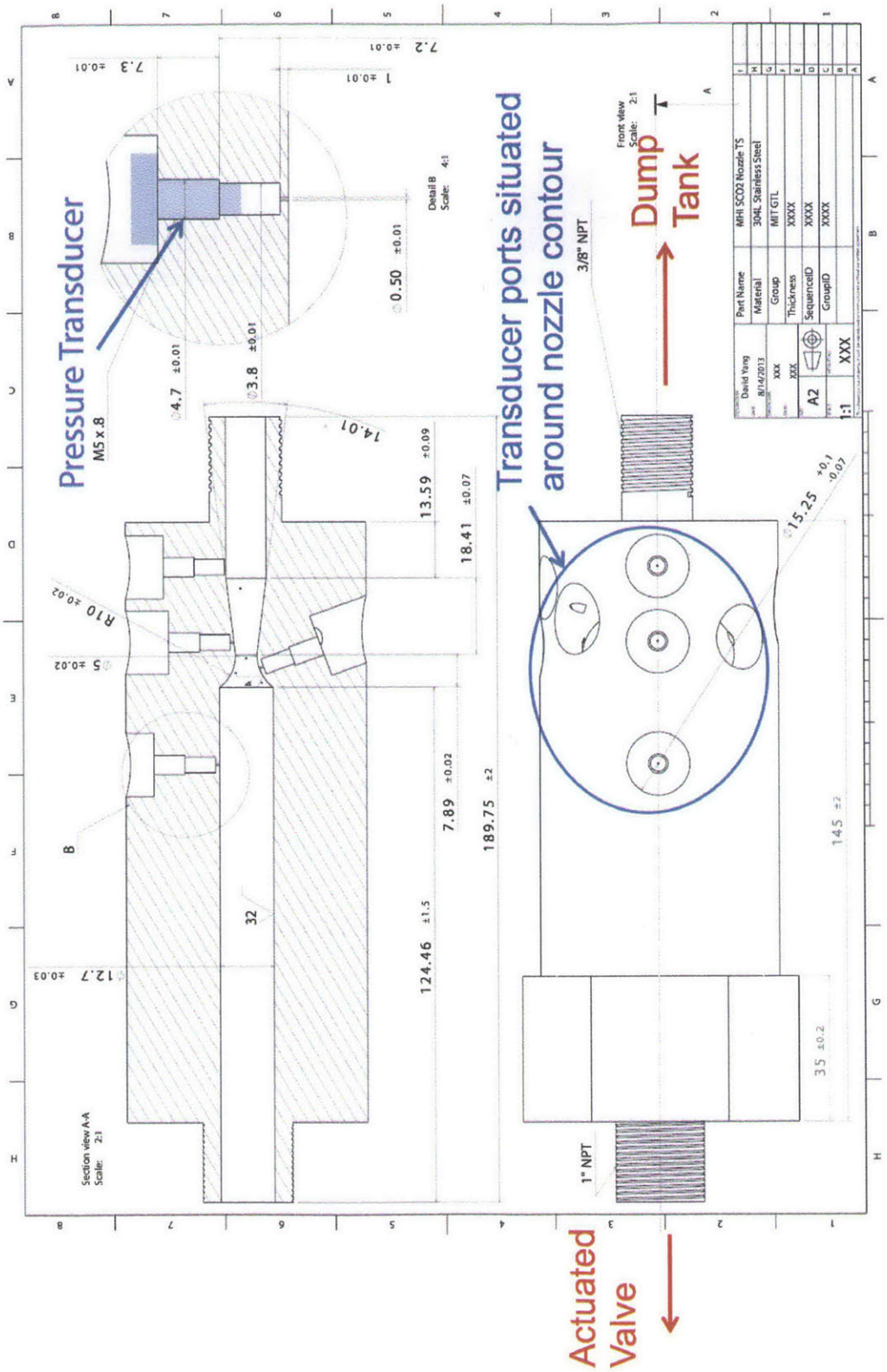

Figure 3-13: Technical drawing of test section with converging-diverging nozzle.

spiral configuration such that uniform heat flux was applied to the tank. Each tape had a maximum heating capacity of 1150 watts for a total of 13.8 kW. One inch of fiberglass insulation is applied to the charge tank surface to reduce heat flux from the charge tank to the environment. Eleven thermocouples were attached to the outside of the charge tank surface to monitor charge tank temperature distribution. The charge and dump tank configurations are depicted in Fig 3-14. Additionally, the dump tank was connected to a .002 millibar vacuum pump and blowoff line. Both were used to evacuate the tank in between tests to ensure no outside fluid was trapped in the test section during testing.

The connection between the tanks included several elements other than the bellmouth and test sections, including an actuated valve situated between the bellmouth and test sections, a manual valve positioned downstream of the test section, a union piece to allow for rotational freedom and a flex pipe to allow for slight misalignments between the two tanks. A labeled picture of the piping setup can be seen in Fig 3-15. The internal flow path is shown in Fig 3-16. The actuated valve has an opening time of 0.4 seconds, closing time of 0.25 seconds, powered by 8 bar air, and controlled through an electrical signal from outside of the test cell for safety reasons. Both valves are of the ball valve type to minimize the influence of each valve on flow through the bellmouth and test sections. All piping elements are constructed out of stainless steel to avoid brittle fracture and ensure that their thermal expansion coefficients are equal.

Filling of the charge tank is accomplished by connecting the charge tank to commercially available carbon dioxide bottles, each with a 50 L capacity at a pressure and temperature of 62 bar and 294 K respectively. The connection pipe is a 8 mm inner diameter copper pipe, insulated to avoid heat transfer to the fluid during transfer. A regulator manifold is situated in between the CO_2 bottles and the charge tank to control fill pressure and ensure no overpressure was supplied to the charge tank.

During testing, control of the test-rig was done through a custom NI LabVIEW interface, depicted in Fig 3-17. The interface shows the pressure readings from the pressure transducers along the test section and charge tank, the temperature readings

(a) Charge tank configuration.

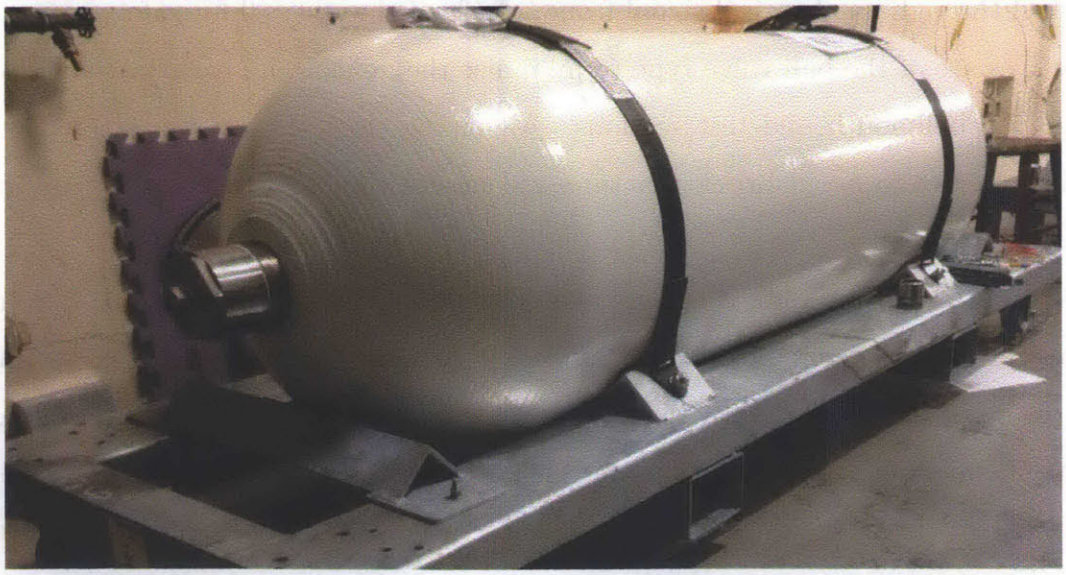

(b) Dump tank configuration.

Figure 3-14: Charge (a) and dump (b) tank configurations.

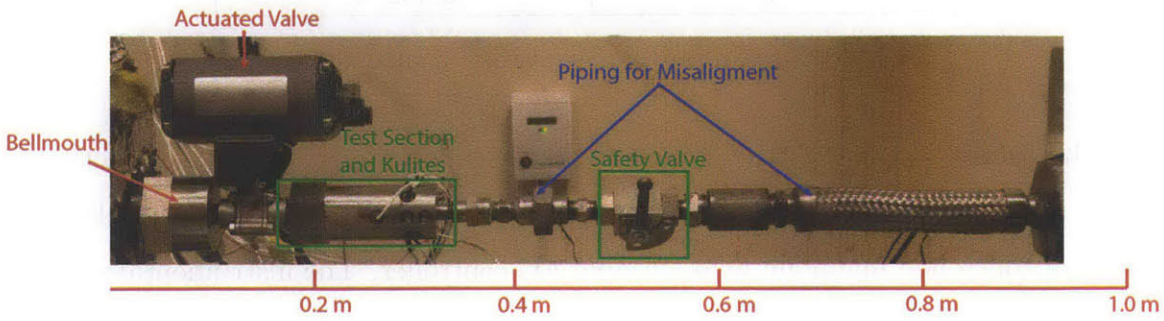

Figure 3-15: Piping setup between the charge and dump tanks.

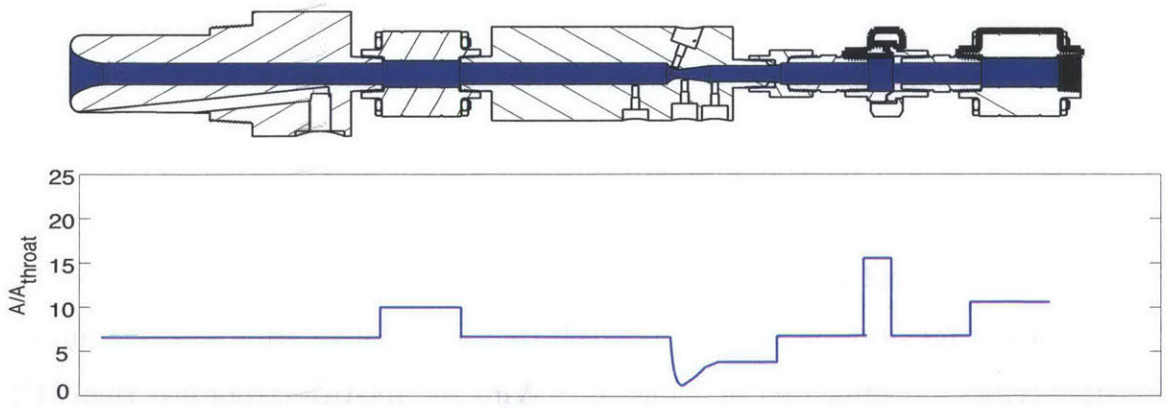

Figure 3-16: Internal flow path of piping

Blowdown Test Number	Maximum Relative Error
1	0.048 %
2	0.050 %
3	0.043 %
4	0.052 %

Table 3.2: Maximum relative errors of blowdown tests

from the thermocouples on the charge tank, and allows for control of the actuated valves, mixer motor, and acoustic actuators inside of the charge tank. The heating tapes are controlled manually by a variable AC controller. The instrumentation connections are diagrammed Fig 3-18. To maintain experimental test-rig safety, multiple CO_2 sensors were placed within the test cell, near the control computer, and CO_2 fill bottles.

3.7 Blowdown Test Repeatibility and Error Analysis

To determine the error of the pressure measurements, back-to-back blowdown tests were conducted at identical charge conditions fo the 4 charge conditions tabulated in Table 3.1 with CO_2 as the working fluid. Pressure measurements from the two tests were compared and the maximum relative error was calculated for each test. Relative error was defined as

$$Error_{rel} = \frac{|p_2 - p_1|}{p_1}, \tag{3.10}$$

with subscripts 1 and 2 referring to separate blowdown tests. p_1 was chosen as the smaller of the pressure measurements, such that the relative error was maximized. Relative errors are tabulated in Table 3.2. With the relative errors less than .1%, the pressure measurements taken during blowdown tests can be considered to be free of spurious or random effects. Additionally, with errors much less than the expected static pressure change due to condensation, it is expected that condensation would be detectable through the static pressure measurements.

Figure 3-17: LabVIEW control interface

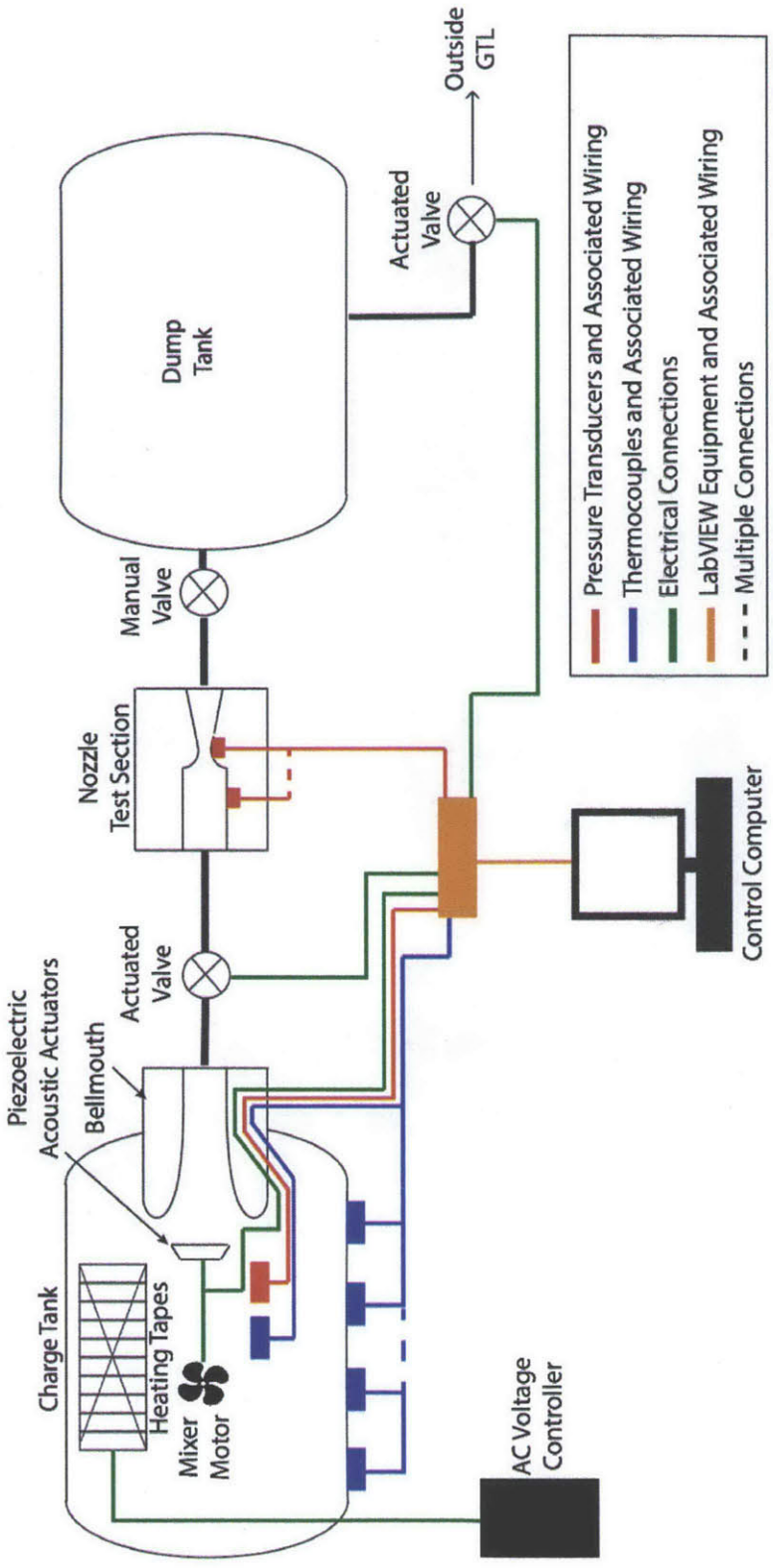

Figure 3-18: Instrumentation diagram

Chapter 4

Speed of Sound Measurement Methodology

As mentioned in Section 2.1, for full characterization of the thermodynamic state of real gas CO_2 with the SW EOS, two thermodynamic properties must be measured. Static pressure was chosen as the first property to be measured due to the simplicity of its measurement. Optical flow measurements are challenging at high pressure and at the small scales involved such that speed of sound was chosen as the second property to be measured. A method of measurement of speed of sound using Helmholtz resonators was devised and is described.

4.1 Helmholtz Resonator Method of Speed of Sound Measurement

The speed of sound measurement method utilized the resonant properties of Helmholtz resonators, as the Helmholtz resonance frequency depends on a fluid's speed of sound. The relevent variables of the Helmholtz resonator and configuration is shown in Fig 4-1. A fast response pressure transducer forms the endwall of the Helmholtz resonator plenum to measure pressure oscillations. The resonance frequency of a Helmholtz

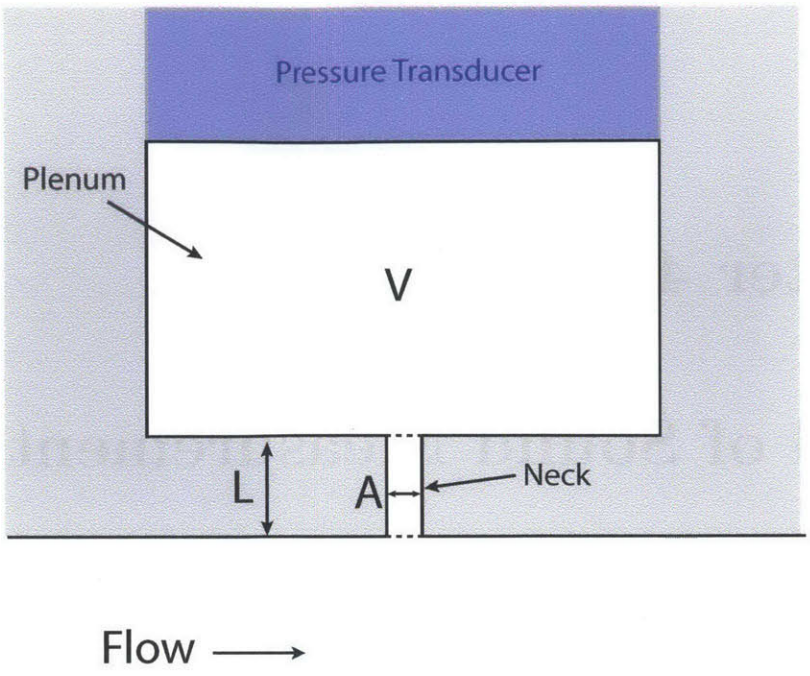

Figure 4-1: Helmholtz resonator geometry.

resonator (HR) is

$$f_H = \frac{c}{2\pi}\sqrt{\frac{A}{VL}}, \tag{4.1}$$

where f_H is the resonance frquency in Hz, c is the speed of sound of the fluid within the pleum of the Helmholtz resonator, A is the cross-sectional area of the duct or neck of the HR, V is the plenum volume, and L is the length of the HR neck. From Eq 4.1, the speed of sound can be calculated if the geometry of the HR and resonance frequency are known. HRs were placed along the nozzle contour and excited by piezoelectric acoustic actuators placed upstream, inside of the charge tank. The acoustic actuators were input with multiple linear frequency sweeps. The dynamic response of each HR was measured by the end wall pressure transducers and the resulting TF (from acoustic actuator input to HR response) of each HR was calculated through spectral analysis. The resonance frequency of each HR is determined by the gain peak and phase roll-off of the HR TFs. The TF calculation process is depicted in Fig 4-2. The range of the input frequency sweep was set to cover the range of expected HR

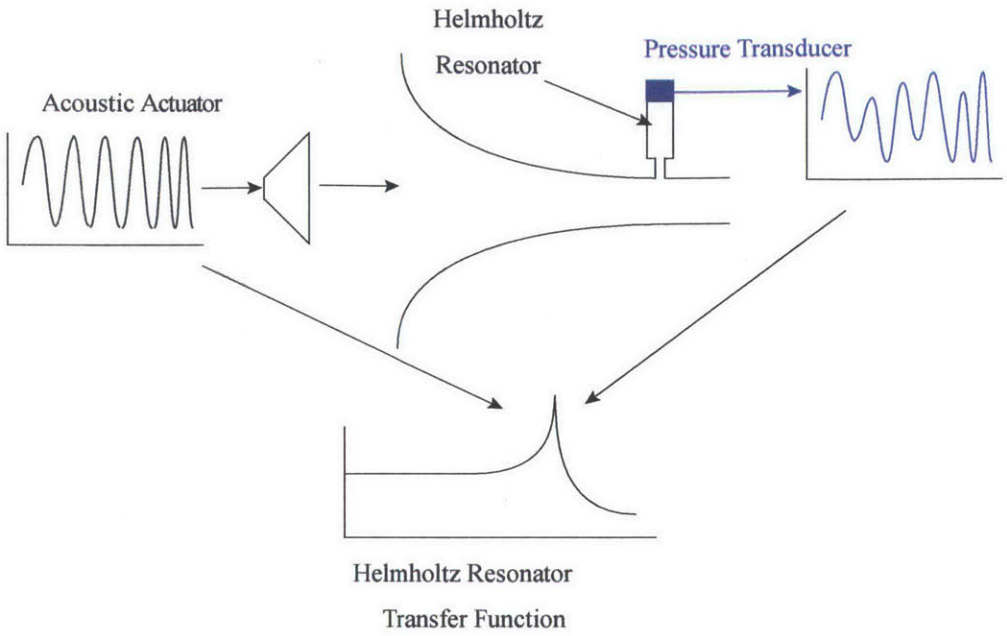

Figure 4-2: Helmholtz resonator forced response experiment.

frequencies, with a 750 Hz buffer in each direction. Expected HR frequencies were calculated by estimating the fluid speed of sound through the SW EOS.

4.2 Speed of Sound Measurement Error

Errors in the Helmholtz resonator method of speed of sound measurement are possible from the following sources:

1. Errors in Helmholtz resonator geometry due to manufacturing errors
2. Errors in identification of HR frequency response gain peak frequency

Error source #1 is controlled in the manufacturing process through dimension tolerance specification. The minimum tolerances in HR dimensions specified during the manufacturing process for L, D, and H were 1%, 2% and .14% respectively. Isolated from the other two error sources, the manufacturing geometry tolerance error results in a 2% maximum error in the speed of sound method. Error source #2 refers to the error in identification of the resonance frequency from the HR frequency response and is discussed further in Section 5.2.

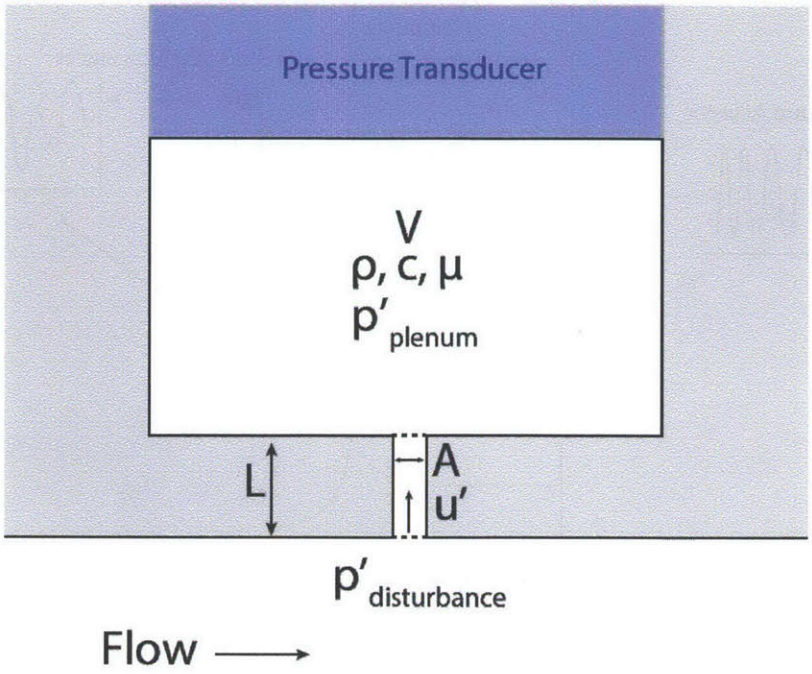

Figure 4-3: Helmholtz resonator model parameters.

4.3 Helmholtz Resonator Model

A frequency response model of the HR was developed in order to guide the design of each HR. The primary model parameters are depicted in Fig 4-3.

Assumptions taken in the development of the model were:

1. HR neck length is small compared to the wavelengths of interest such that it can be taken as compact

2. Compression in the HR plenum is isentropic

3. There is no mean flow through the HR neck

4. The HR neck is adiabatic

With these assumptions, the governing equations of the HR dynamics are reduced to a force balance on the fluid in the HR neck and the unsteady, isentropic compression

of the fluid within the HR plenum:

$$\rho L\frac{\partial u'}{\partial t} + \xi L u' = p'_{disturbance} - p'_{plenum}, \tag{4.2}$$

$$\frac{\partial p'_{plenum}}{\partial t} = \frac{\rho c^2 A}{V} u'. \tag{4.3}$$

The viscous damping term, $\xi L u'$, is used to account for boundary layer effects in the neck and was formulated such that Eq 4.2 remains a linear PDE. The viscous term,

$$\xi = K\frac{32\mu}{D^2}, \tag{4.4}$$

was formualted based on fluid resistance in Hagen-Poiseuille flow [19]. With HR frequencies on the order of 1000 Hz, the reduced frequency, β, was calculated to be greater than unity and unsteady effects were expected to be significant. To account for these unsteady effects, ξ included an empirical factor K. Determination of the value of K and significance of unsteady effects in the HR neck are discussed in further detail in Section 4.4.

In order to develop the transfer function for the HR in the frequency domain, the Laplace transform was applied to Eqs 4.2 and 4.3 with $s = j\omega$, resulting in:

$$\rho L s U' + \xi U' = P'_{disturbance} - P'_{plenum}, \tag{4.5}$$

$$s P'_{plenum} = \frac{\rho c^2 A}{V} U'. \tag{4.6}$$

Solving for the ratio of P'_{plenum} and $P'_{disturbance}$ yields the transfer function for the HR,

$$\frac{P'_{plenum}}{P'_{disturbance}} = \frac{\rho c^2 A}{\rho c^2 A + sV(\rho L s + \xi)}. \tag{4.7}$$

The result is a 2nd order system with a natural frequency represented by Eq 4.1 with damping controlled by ξ. A comparison between the frequency response of undamped, underdamped, and overdamped responses can be seen in Fig 4-4. The peak in gain reduces in magnitude as damping ratio is increased, until the damping ratio becomes

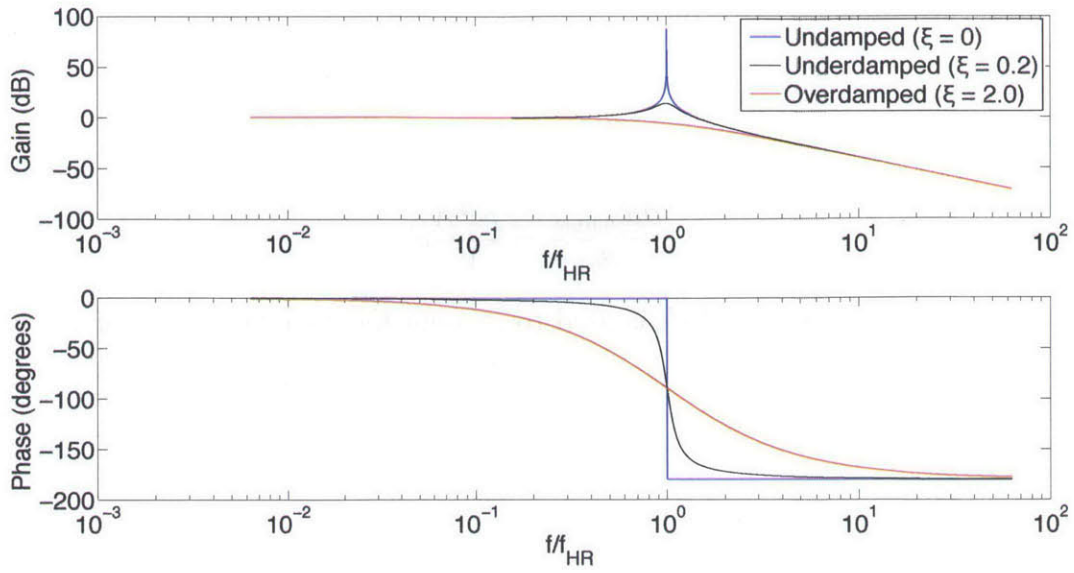

Figure 4-4: Bode plot for an undamped, underdamped, and overdamped HR response.

larger than unity, at which point, the gain peak disappears. Additionally, widens the phase roll off as well.

4.4 Helmholtz Resonator Viscous Damping Analysis

With viscous damping having a significant effect on the HR frequency response characteristics, it was essential to identify the factors affecting HR damping to ensure that the HR was underdamped during testing. Viscous damping was investigated through a theoretical scaling analysis of fluid flow in the HR neck and an experimental study of HR dynamics in the shock tube facility at the GTL.

4.4.1 Theoretical Analysis of Unsteady Effects on Damping in Helmholz Resonator Neck

The theoretical analysis of fluid flow in the HR neck focused on determining the significance of unsteady effects in relation to viscous and intertial forces. A scaling analysis of the unsteady, 1-D Navier-Stokes (N-S) equation was conducted. In

cylindrical coordinates, the N-S equation reduces to

$$\frac{\partial u}{\partial t} = -\frac{1}{\rho}\frac{\partial p}{\partial z} + \frac{\mu}{\rho}[\frac{1}{r}\frac{\partial}{\partial r}(r\frac{\partial u}{\partial r})] \tag{4.8}$$

The non-dimensional terms corresponding to each term in the N-S equation are shown in Table 4.1.

Term	$\frac{\partial u}{\partial t}$	$\frac{1}{\rho}\frac{\partial p}{\partial z}$	$\frac{\mu}{\rho}[\frac{1}{r}\frac{\partial}{\partial r}(r\frac{\partial u}{\partial r})]$
Non-dimensional scaling	$\beta = \frac{\omega L}{u}$	1	$\frac{1}{Re_D}\frac{L}{D}$

Table 4.1: Non-dimensional groups for Eq 4.8.

The ratio of the magnitudes of the unsteady term, β, and the viscous term, $\frac{1}{Re_D}\frac{L}{D}$, is known as the Womersley number [20], α,

$$\alpha^2 = \frac{\beta}{\frac{1}{Re_D}\frac{L}{D}} = \frac{\omega D^2}{4\nu}. \tag{4.9}$$

Put another way, the Womersley number represents the ratio of transient inertial forces to steady viscous forces. At high frequencies, such that $\alpha > 1$, the magnitude of total viscous damping is greater than the viscous damping in steady flow. The increase in viscous damping is the result of the formation of a Stokes layer in an unsteady flow [21], which has a much greater velocity gradient and thus higher shear stress within the fluid. The magnitude of the shear stress limits the velocity of fluid within the neck which limits the fluid's ability to respond to rapid changes in force, such as those present in an oscillatory flow. A comparison between the velocity profile in unsteady flow and Hagen-Poiseuille flow is depicted in Fig 4-5. A quantitative relationship between the non-dimensional parameters and HR damping ratio was required to ensure the HR response was underdamped. The quantitative scaling relationship was developed through experimental measurements on a sample HR connected to a shock tube and is discussed next.

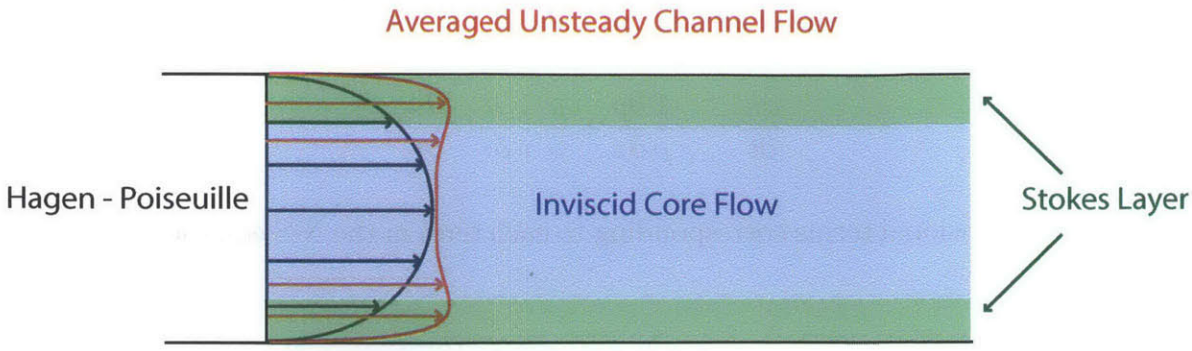

Figure 4-5: Comparison between unsteady Stokes layer and Hagen-Poiseuille flow.

4.4.2 Experimental Investigation of Helmholtz Resonator Response

Experimental investigation of the dependence of Helmholtz resonator dynamics on the various non-dimensional parameters was accomplished at the shock tube facility at the GTL. The shock tube allowed for measurement of the HR's impulse response. From the impulse response, the damping ratio was calculated and compared as a function of various non-dimensional parameters.

4.4.2.1 Shock Tube Experimental Setup

For the shock tube tests, an Helmholtz resonator was installed to the cylindrical shock tube with the face of the HR configured such that the neck opening was flush to the shock tube wall to avoid the generation of additional shocks resulting from geometric discontinuities. The HR geometry was set such that the expected HR frequency was 1 kHz. Two pressure transducers were used during testing, one attached to the HR plenum and one reference transducer mounted flush to the shock tube wall in the driven section. The natural frequency for both transducers was above 100 kHz, much higher than the resonance frequency of the HR. Both of the measured signals was unfiltered and the error of the transducers was found to be ± 0.03 bar. The general setup of the experiment is depicted in Fig 4-6. The shock tube had a 50 mm diameter with the driven and driver sections having an equal length. The diaphragm

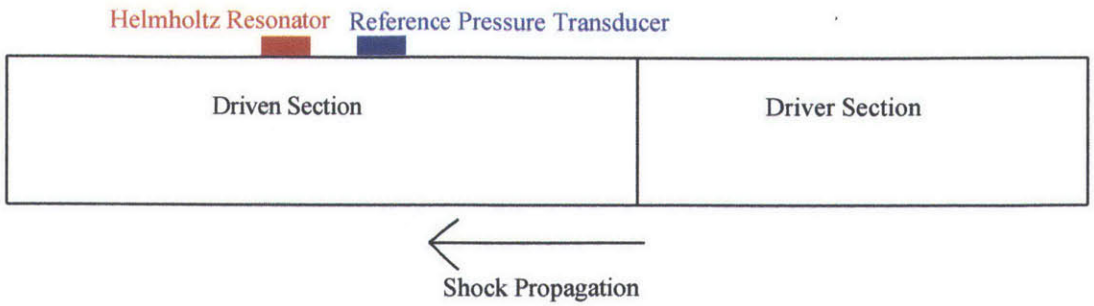

Figure 4-6: Shock tube experiment setup.

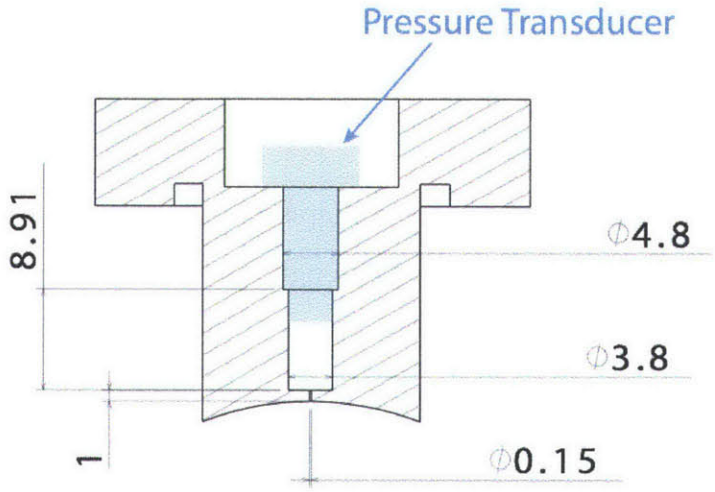

Figure 4-7: Initial HR geometry for shock tube tests, light blue indicates pressure transducer.

used in testing was constructed from aluminum foil and allowed for control of the shock pressure ratio, with shock pressure ratios ranging from 1.2 to 2.5. Working fluid during testing was dry air. The HR geometry used in the impulse response tests is shown in Fig 4-7

4.4.2.2 Experimental Procedure and Parameters Varied

The scaling analysis conducted in Section 4.4.1 indicated that the major non-dimensional parameters of interest for HR damping were the neck Reynolds number, Womersley number, and slenderness ratio, L/D. In order to vary these parameters, the diaphragm pressure ratio and HR duct diameter were altered between shock tube tests. Combinations used are tabulated in Table 4.2. For each shock tube test the driver

Shock Tube Test Number	Diaphragm Pressure Ratio	HR L/D
1	1.55	6.66
2	1.26	4.44
3	1.28	3.33
4	1.29	1
5	1.5	4.44
6	1.41	3.33
7	1.5	1
8	1.62	3.33
9	1.66	3.33
10	1.65	1
11	1.62	1

Table 4.2: Combinations of diaphragm pressure ratio and HR duct diameter used.

section pressure was increased until the diaphragm burst and the end cap was removed such that the shock propagating through the shock tube exited the tube after passing past the pressure transducers.

4.4.2.3 Shock Tube Test Results and Discussion

The first shock tube test was conducted with a diaphragm pressure ratio of 1.55 with a HR L/D of 6.66, resulting in a Reynolds number of 4800, based on HR neck diameter. Pressure histories for the reference pressure transducer and HR pressure transducer during the first test are plotted in Fig 4-8. Shock wave reflections follow the initial pressure step and are shaded in gray. τ is the sound travel time through the shock tube and defined as

$$\tau = \frac{l_{ST}}{c_{sound}}. \tag{4.10}$$

For the initial ST test, the HR pressure lagged significantly behind the shock tube pressure, indicating an overdamped HR response. The damping ratio of the test was calculated through use of the HR model by adjusting the K factor until the model response agreed with the experimental HR response. An example of the matched pressure histories can be seen in Fig 4-9. The damping ratio calculated from the adjusted HR model was 22.15, verifying that the HR was severely overdamped. Damping ratios from the subsequent ST tests were calculated in a simlar manner and tabulated

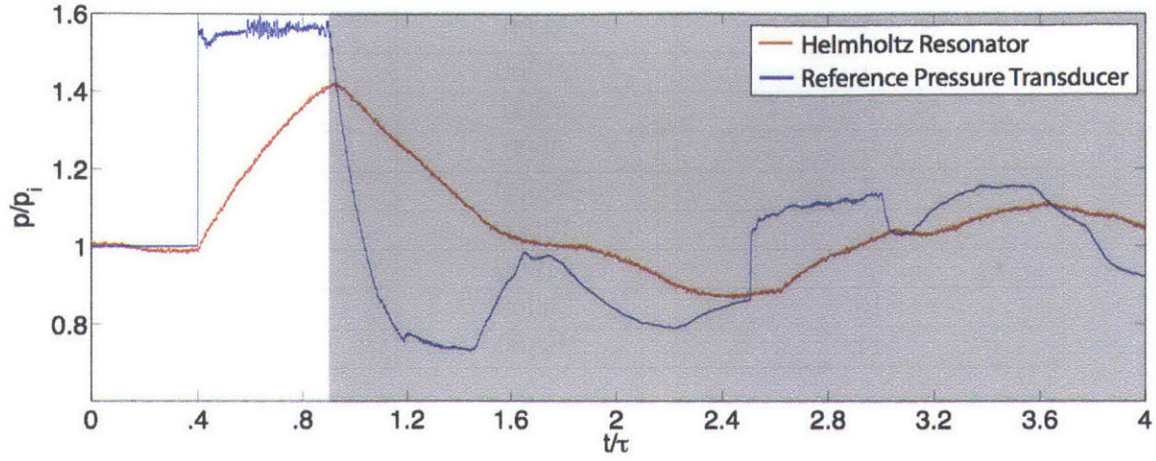

Figure 4-8: Pressure history for HR and flush pressure transducers during shock tube test 1.

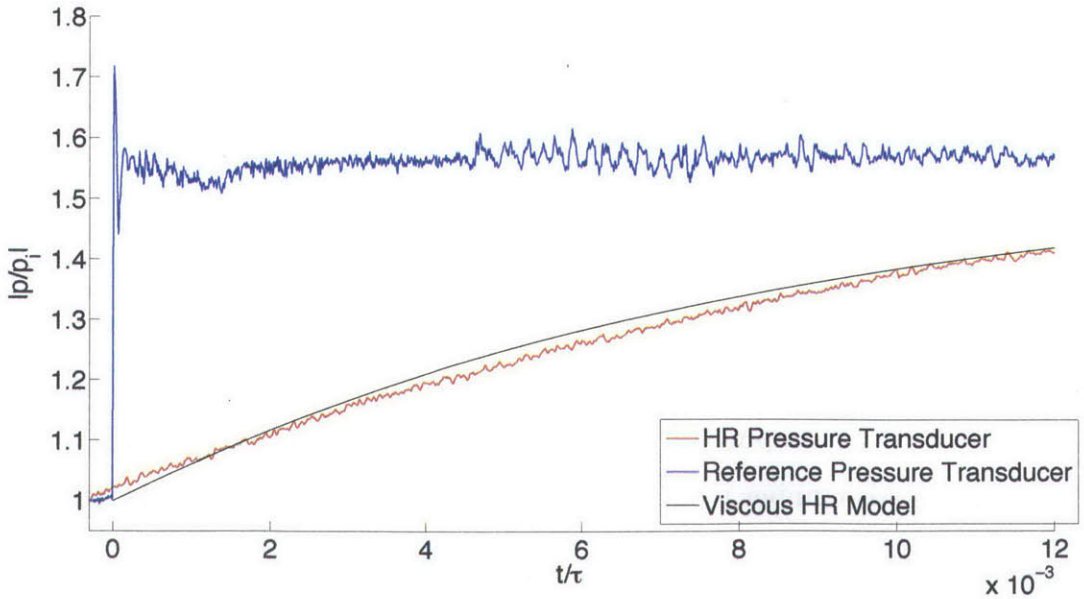

Figure 4-9: Experimental HR pressure history and HR model estimated pressure history.

Shock Tube Test Number	Reynolds Number	HR Damping Ratio
1	4800	22.15
2	6100	12.13
3	8000	9.27
4	27200	3.30
5	7300	13.38
6	9000	8.74
7	32500	3.10
8	10600	10.27
9	11000	9.65
10	36000	2.98
11	35800	3.26

Table 4.3: Reynolds numbers and damping ratios for shock tube tests.

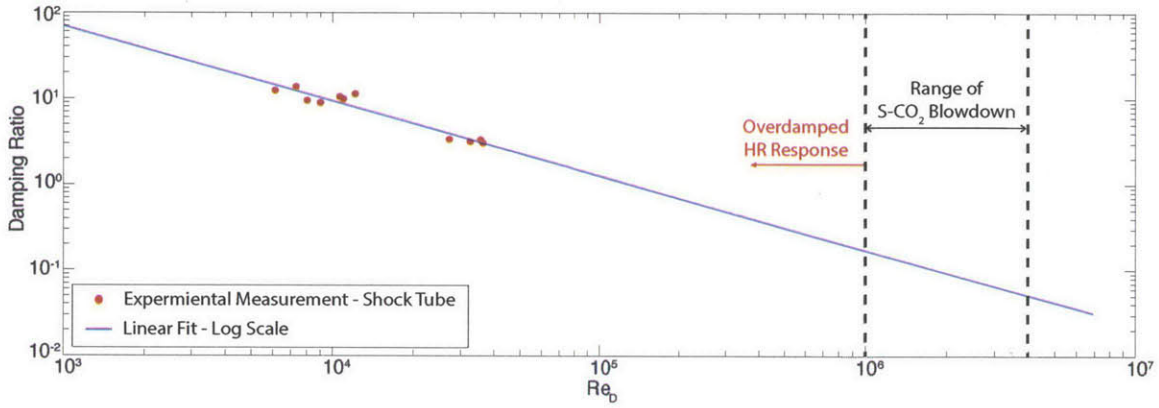

Figure 4-10: HR damping ratio as a function of Reynolds number.

in Table 4.3 along with the corresponding Reynolds numbers. The HR damping ratio as a function of Reynolds number is plotted in Fig 4-10. Examination of Fig 4-10 revealed a strong dependence of the HR damping ratio on HR neck Reynolds number. Based on the available experimental information, an underdamped response of the HR was calculated (damping ratio < 1) to be achievable at a Reynolds number of 10^6. This Reynolds number requirement became the driving factor in the HR design.

4.5 Helmholtz Resonator Design and Sizing

The requirements driving Helmholtz resonator design were the following, in order of importance:

1. HR to have an underdamped response during the CO_2 blowdown tests
2. HR plenum diameter equal to pressure transducer face diameter
3. HR neck length such that maximum number of resonators can be placed along nozzle contour

Requirement #1 was controlled solely by the HR neck diameter and CO_2 fluid properties. With the fluid properties are set by test conditions, the HR neck diameter is the only variable that could be manipulated and was set to 0.5 mm in order to meet requirement #1, resulting in a Reynolds number of 1.2 million during CO_2 testing. Requirement #2 was set by the pressure transducers used in testing and equal to 3.8 mm. Requirement #3 was set to maximize the limited amount of physical space available and set to 1 mm HR neck length to allow for eight pressure transducers to be positioned along the converging nozzle contour. The last degree of freedom, the plenum depth, was set by the design frequency of the HR.The design frequency was chosen to be 1500 Hz, resulting in a plenum depth of 6.9 mm. The final HR geometry can be seen in Figure 4-11. All HRs along the nozzle contour followed this geometry.

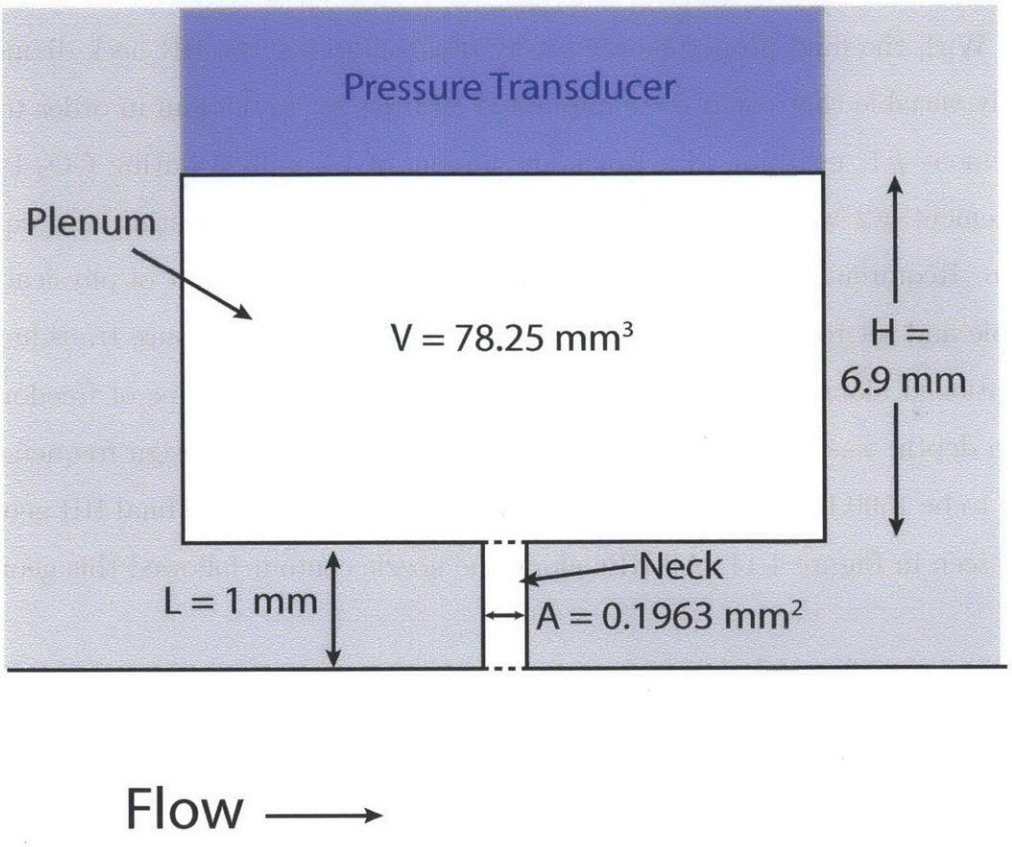

Figure 4-11: Final HR geometry (Note: not to scale).

Chapter 5

Experimental Assessment of Helmholtz Resonator Based Speed of Sound Measurement

To verify the speed of sound measurement method and Helmholtz resonator design methodology, an experimental study was conducted with high pressure air. The assessment was conducted on the same test-rig used for the blowdown tests, described in Chapter 3.

5.1 Experimental Setup and Procedure

Calculation of speed of sound by the Helmholtz resonator method required the transfer function of the HR to be calculated for each test. As mentioned in Section 4.1, transfer function calculation was accomplished by forcing the HRs with a linear frequency sweep and recording the dynamic response. A simple diagram illustrating the forced response method is shown in Fig 5-1. The acoustic forcing was provided by eight acoustic actuators positioned upstream of the bellmouth entrance. Each actuator was rated to emit a sound pressure of 93 dB in the frequency range of interest and were connected in parallel. A function generator and amplifier were used to provide the input signal to the acoustic actuators. The input signal chosen varied between

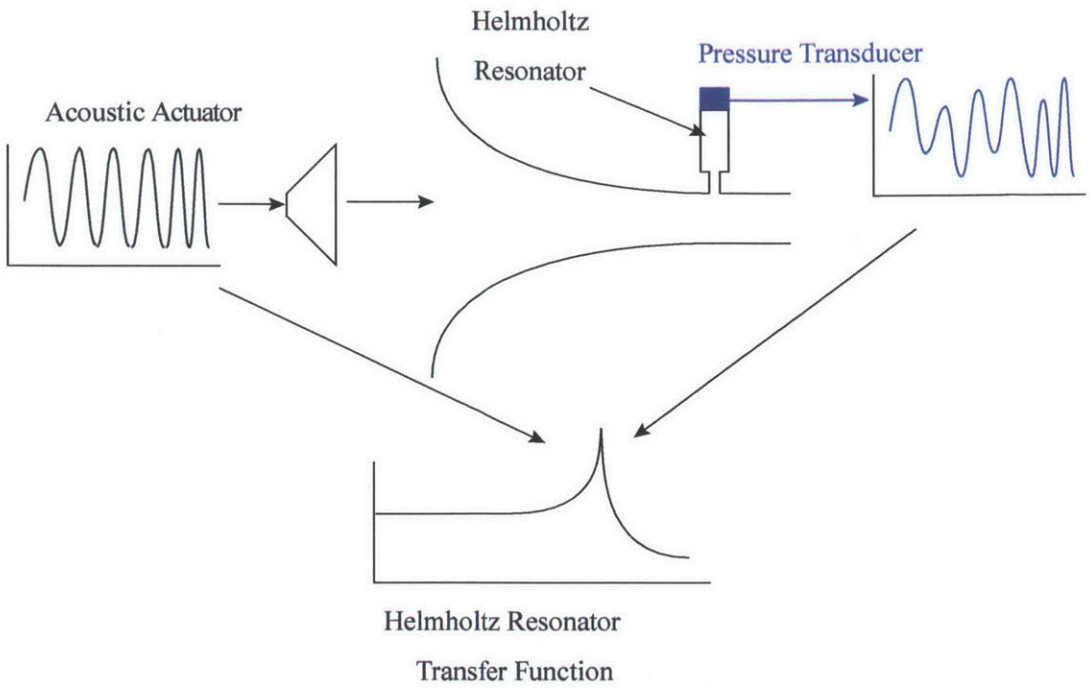

Figure 5-1: Transfer function estimation from forced excitation.

tests, but in all cases was a linear chirp signal from a pre-determined start to end frequency. By using a linear frequency sweep, it was possible to record the frequency response of the HRs over a wide range of frequencies with a single test. Response of the pressure transducers attached to the HRs were recorded simultaneously along with the input signal. All data was recorded at a frequency high enough such that the Nyquist frequency was at least twice as large as the largest frequency input to the acoustic actuators.

To maintain a linear relationship between the input signal and HR response, the initial speed of sound measurement verification focused on no flow (static) testing to remove any acoustic non-linearities that would result from convective flow effects. Static testing was accomplished by opening the actuated valve while keeping the downstream valve closed, subjecting the HRs and pressure transducers to the charge tank fluid while not allowing any flow through the nozzle test section.

To match the Reynolds number present in S-CO_2 testing, maintain test safety, and simplify calculations by removing real gas effects, high pressure air was used during HR SoS verification testing. The air pressure was set such that the Reynolds number

based on HR neck diameter and air speed of sound was 10^6. The air was kept at room temperature for a large enough time such that the air inside the charge tank was at equilibrium and uniform for all tests.

5.2 HR Transfer Function Estimates

Transfer function estimation is a well researched area in the field of signal processing. Many algorithms have been developed to calculate system transfer functions, each with its own set of benefits and weaknesses. Such algorithms have been applied to a wide variety of fields, from gas turbine dynamics to electrical circuits [22]. One of the main approaches to TF estimation is known as spectral density estimation (SDE), which aims to determine the frequency response characteristics of the system by calculating the power content of a signal as a function of frequency. While there are many techniques in order to accomplish SDE, almost all of them attempt to achieve high resolution in the frequency response estimation while minimizing noise that is inherently present in data taken from experimentation. Two well-known techniques are known as Welch's method and the Blackman-Tukey method, each of which were utilized for estimating the HR frequency response dynamics in testing. Welch's method was implemented through user-written code while the Blackman-Tukey method was implemented through the built-in MATLAB function "spa." Both of these methods are based on smoothing the empirical transfer-fucntion estimate (ETFE), which is the ratio of the Fourier transform of the output signal to the the Fourier transform of the input signal. Definition of the discrete Fourier transform U_N, for a signal $u(t)$ is

$$U_N(\omega) = \frac{1}{\sqrt{N}} \sum_{t=1}^{N} u(t) e^{-i\omega t}. \tag{5.1}$$

While the ETFE can be a useful tool for investigating the frequency response of a system, the ETFE is greatly affected by noise due to its poor variance properties [22] and generally performs poorly with most experimental datasets. To reduce the variance of the ETFE, SDE utilizes what are known as the cross density spectrum and power density spectrum estimates. The cross density spectrum represents the mag-

nitude of correlation between two-signals at each frequency while the power density spectrum represents the power content of a single signal at each frequency. General formulations for the cross density spectrum, ϕ_{yu}, and power density spectrum, ϕ_u, are:

$$\phi_{yu}(\omega) = \sum_{\tau=-\infty}^{\infty} R_{yu}(\tau)e^{-i\tau\omega}, \tag{5.2}$$

$$\phi_u(\omega) = \sum_{\tau=-\infty}^{\infty} R_u(\tau)e^{-i\tau\omega}, \tag{5.3}$$

with,

$$R_{yu}(\tau) = \lim_{N\to\infty} \frac{1}{N} \sum_{t=1}^{N} y(t)u(t-\tau),$$

$$R_u(\tau) = \lim_{N\to\infty} \frac{1}{N} \sum_{t=1}^{N} u(t)u(t-\tau).$$

The transfer function, $G(\omega)$, between $y(t)$ and $u(t)$ is

$$G(\omega) = \frac{\phi_{yu}}{\phi_u} \tag{5.4}$$

For numerical calculations, the cross density spectrum and power density spectrum calculations can be simplified by utilizing the properties of the Fast Fourier Transform (FFT), such that the calculation for the cross density spectrum and power density spectrum reduce to

$$\phi_{yu} = \frac{FFT(y(t)) * conj(FFT(u(t)))}{N^2}, \tag{5.5}$$

$$\phi_u = \frac{FFT(u(t)) * conj(FFT(u(t)))}{N^2}. \tag{5.6}$$

5.2.1 Coherence Function

For experimental forced response datasets there is often an open question on whether or not a system is being forced enough to generate a measurable response. Additionally, there are many factors which may affect how a system responds to a forcing signal that are independent of the system's inherent frequency response. These ad-

ditional factors may introduce non-linearities to the system's response. In order to determine whether enough forcing was applied to a system or determine whether a system's response was directly related to the input signal at different frequencies, a function known as the coherence function is often used.

The coherence function or coherency spectrum is a non-dimensional, frequency-dependent metric that represents the correlation between an input and output signal. A value of one represents perfect correlation, while a value of zero represents no correlation between the two signals [22]. The formulation of the coherence function is

$$\kappa_{yu} = \sqrt{\frac{|\phi_{yu}(\omega)|^2}{\phi_y(\omega)\phi_u(\omega)}} \tag{5.7}$$

The coherence spectrum was used throughout the HR verification tests to determine whether the HR frequency response dynamics were captured by the pressure transducers or additional forcing was required.

5.2.2 Welch's Method

Welch's method aims to reduce the variance and influence of noise of the ETFE at the expense of frequency resolution [23]. While reduced frequency resolution is generally undesirable, the reduced variance is often well worth the tradeoff. Welch's method takes the following steps to improve the ETFE:

1. The input and output signal are split into overlapping segments of equal length; typical overlap is 50%. A graphical representation of the split and overlap process can is shown in Fig 5-2.

2. Each segment is "windowed." A wide variety of window functions exist, each with its own set of benefits. A list and description of several popular windowing functions can be found in [22]. The windowing function applied for the HR verification tests was the Hanning window. The formulation of the Hanning window is

$$w(n) = 0.5(1 - cos(\frac{2\pi n}{N-1})), \tag{5.8}$$

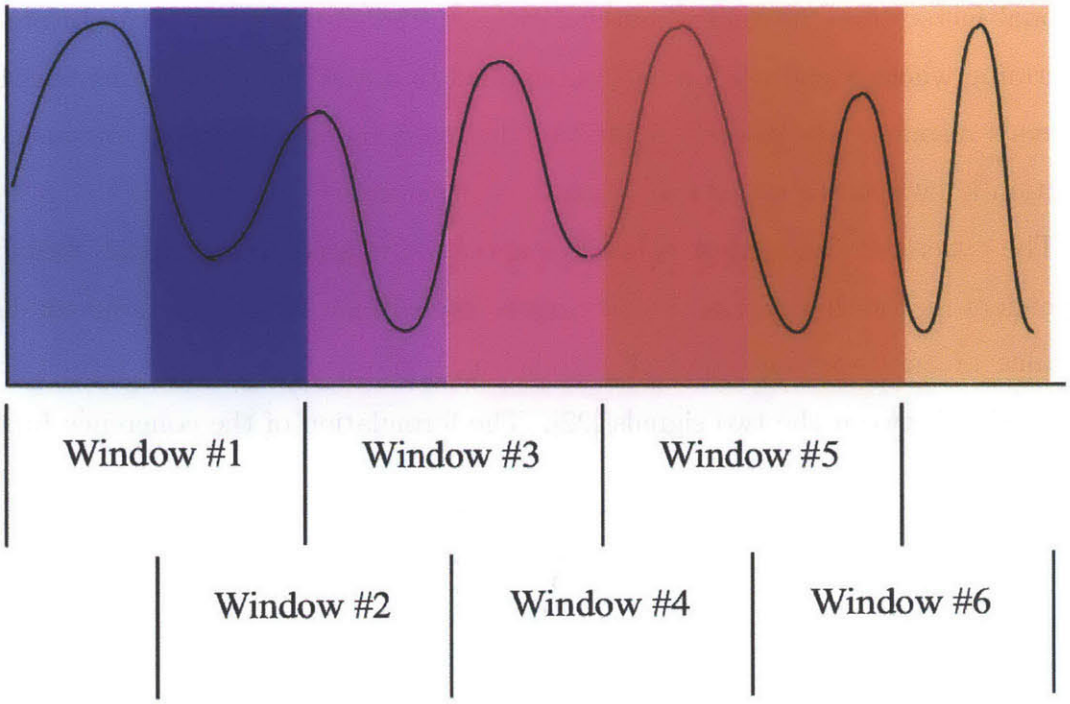

Figure 5-2: Welch method of signal split and overlap.

and is graphically represented in Fig 5-3.

3. The TF is calculated for each segment pair and the frequency response is averaged among all window pairs to obtain the final TF estimate

The two main properties of the resulting TF estimate, frequency resolution and smoothing, are controlled by the choice of window length, with small windows favoring smoothing and larger windows favoring frequency resolution. Window length was varied for each test until an acceptable balance was achieved. Window length was approximately 100,000 samples for each test.

5.2.3 Blackman-Tukey Method and MATLAB "spa" Function

Similar to the Welch method, the Blackman-Tukey (BT) method [24] aims to reduce the variance in the ETFE at the cost of frequency resolution, but does so in a different manner. The key differences between the two methods are:

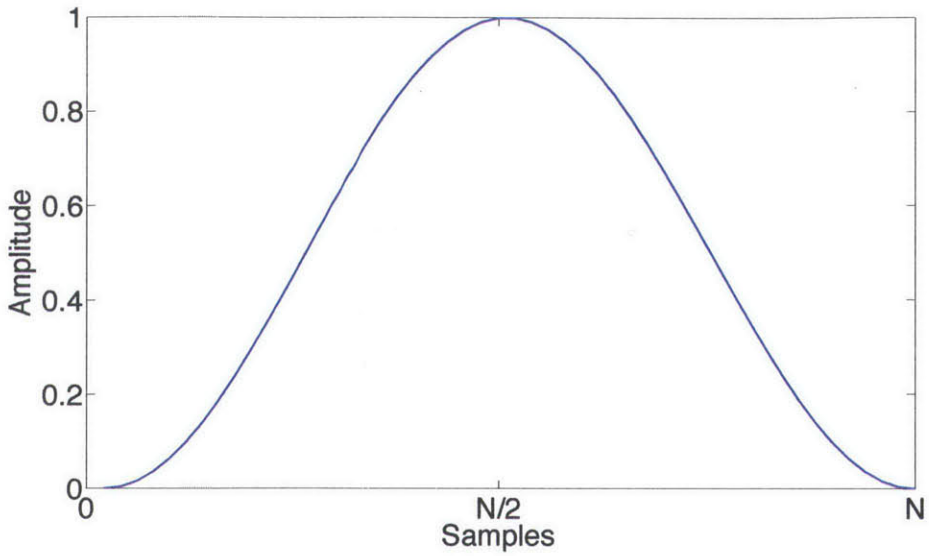

Figure 5-3: Hanning window as a function of samples.

1. The BT method utilizes the entire length of the signals without splitting them,

2. Window functions are used in the BT method, but are applied after the Fourier transform is applied to the signals (the window used was the Hanning window).

A detailed description of the mathematical formulation of the BT method and benefits can be found in [25]. MATLAB has a built-in function known as "spa" that applies the BT method to a pair of signals to compute an estimate of the transfer function. This function was utilized to compare the BT method to Welch's method.

5.2.4 Comparison Between the Welch and Blackman-Tukey Methods

A simple test case was conducted in order to qualitatively determine how the choice of window size affected the TF estimates calculated by the Welch method and MATLAB "spa" function. The test case consisted of an input signal $u(t)$, an output signal $y(t)$, a known TF, $G(\omega)$, and a white noise function $o(t)$. Formulations for the input signal, known TF, and output signal are shown in Eqs 5.9, 5.10 and 5.11 respectively. The TF function was formulated such that its value varied linearly with frequency since

the input signal's frequency varies linearly with time.

$$u(t) = Chirp(100\ Hz, 1500\ Hz, 50\ seconds) \tag{5.9}$$

$$G(t) = 1 + 0.1t \tag{5.10}$$

$$y(t) = G(t)u(t) + o(t) \tag{5.11}$$

The corresponding transfer function in the frequency domain becomes

$$G(\omega) = 1 + \frac{\omega}{560\pi}. \tag{5.12}$$

$u(t)$ and $y(t)$ are simulated in MATLAB with a data acquistion frequency of 5000 Hz. The amplitude of the white noise function was set to 1000% of the the amplitude of $u(t)$ to simulate an absolute "worst case" scenario and emphasize differences between the two methods. The input and output signals were input to the MATLAB "spa" function and Welch's method with window sizes ranging from 2000 to 20,000 samples. A comparison of both functions as well as the true TF is shown in Fig 5-4. While all of the estimates follow the true TF as a mean-line, their frequency resolutions and noise characteristics vary greatly as expected. The Welch method with 20,000 sample windows performs very poorly, with noise dominating the frequency response. Welch's method with 2000 sample windows performs better with much less noise, however still exhibits significant variations from the true TF. For the simple test conducted, the Blackman-Tukey method in the form of the "spa" function performs the best, closely following the true TF with very little noise. Further reduction in window size for the Welch method was conducted to determine if the noise could be mitigated further, with the number of samples per window set to 200. A comparison between the 200 sample window Welch method, 2000 sample window Welch method, "spa" function, and true TF is shown in Fig 5-5. The 200 sample window Welch method performs much better compared to the 2000 sample Welch method, closely following the "spa" estimate and much closer to the true TF. However, the 200 sample per window Welch method also exhibits much less frequency resolution compared to

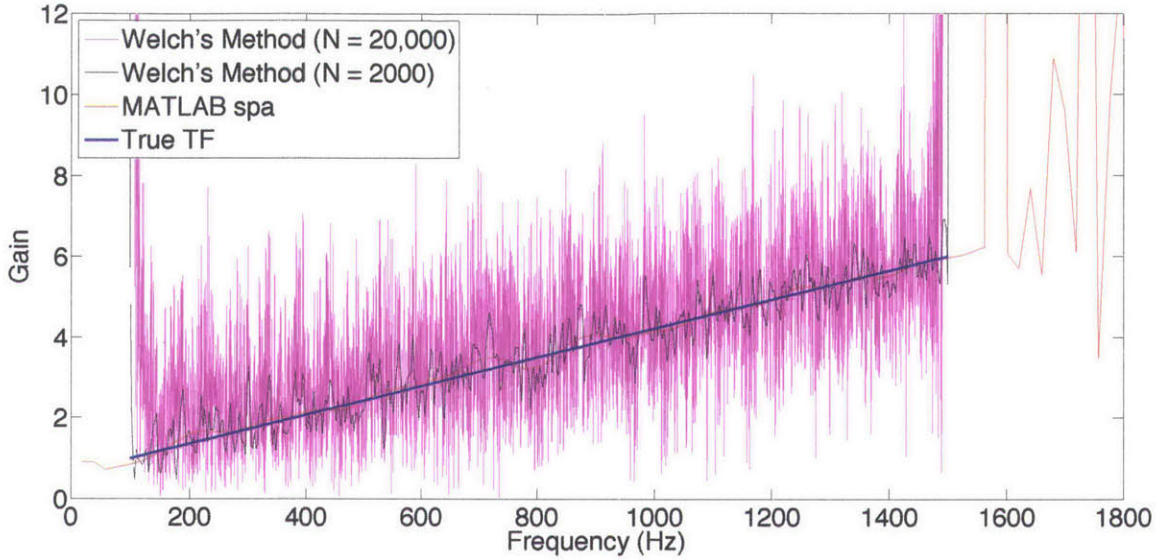

(a) Full frequency range.

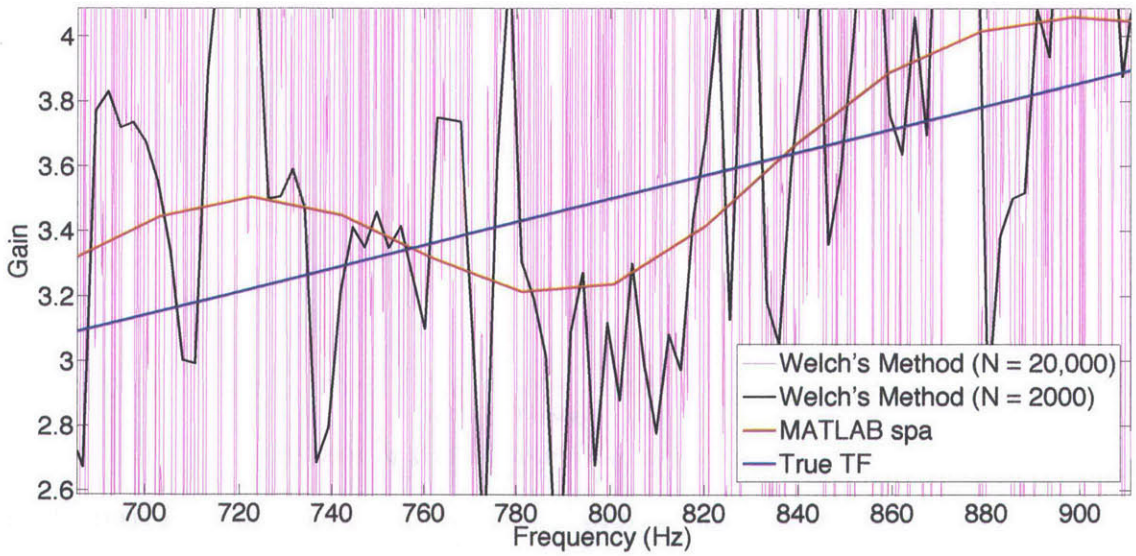

(b) Zoomed in, range from 700 to 900 Hz.

Figure 5-4: Comparision between MATLAB "spa" and Welch's method.

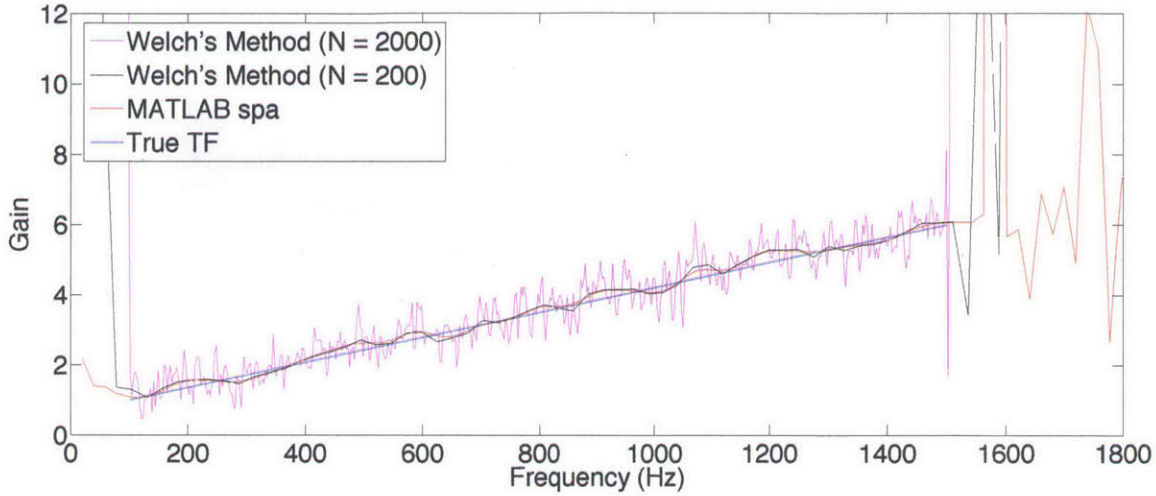

(a) Full frequency range.

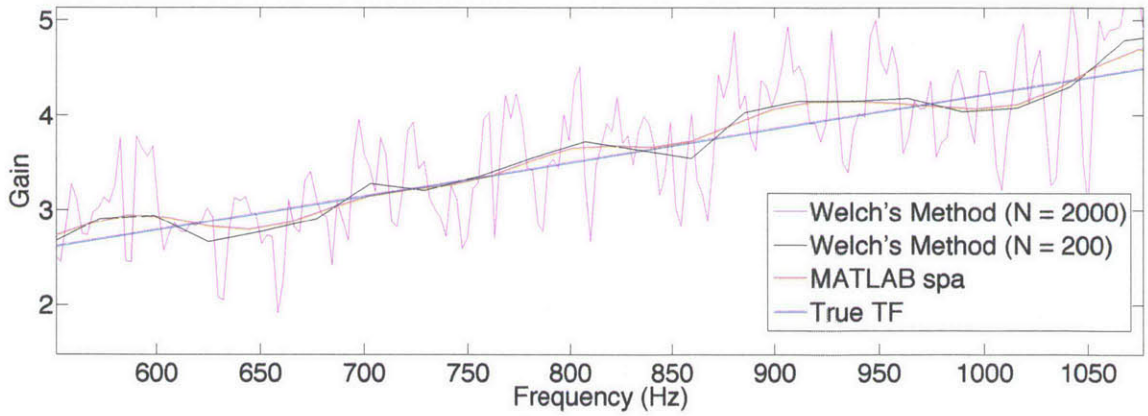

(b) Zoomed in, range from 600 Hz to 1000 Hz.

Figure 5-5: Comparision of reduced sample window Welch method with true TF and "spa."

the 2000 sample Welch method. From the simple tests conducted, it was concluded that the number of samples to use per window depended heavily on the amount of noise present in the signals and that the "spa" function seemed to perform very well no matter the amount of noise. For most realistic cases, the signal-to-noise ratio is expected to be much lower than the 1000% used in comparison testing. For the test conditon under consideration, it is expected that the Welch method can be employed reliably with window lengths exceeding 2000. Determination of the optimal window length is determined on a case-by-case basis.

5.3 Experimental Test Results and Discussion

For the experimental static tests, the expected HR frequency was 3250 Hz, based on estimated speed of sound. The acoustic actuators were driven with a linear chirp signal from 2500 Hz to 4000 Hz over 30 seconds and run at their maximum output of 95 dB each. Chirp signal time was chosen to be large enough to provide an adequate data signal length for signal processing purposes. The calculated frequency response using Welch's method with a window size of 50,000 samples, along with coherence for the first pressure transducer in the converging nozzle is shown in Fig 5-6. Additionally, by assuming the HR dynamics could be represented by a 2nd order system, the damping ratio of the HR was calculated from the phase roll-off. The HR exhibits a peak in gain and a phase roll-off at the expected resonance frequency. Along with the high coherence in the region of the acoustic sweep, the exhibited frequency response dynamics suggested resonance was achieved in the first HR in the converging nozzle during the static high pressure air test. From the phase-roll off rate shown in Fig 5-6, the damping ratio of the HR was calculated to be 0.04. To verify that the gain behavior of the pressure transducer was consistent the phase behavior, a 2nd order system was constructed with the measured resonance frequency and damping ratio. The model and the estimated HR dynamics are compared in Fig 5-7. The agreement between measured HR dynamics and TF model verified the damping ratio of the HR was 0.04 and the previous analysis. The calculated damping ratio was added to Fig 4-

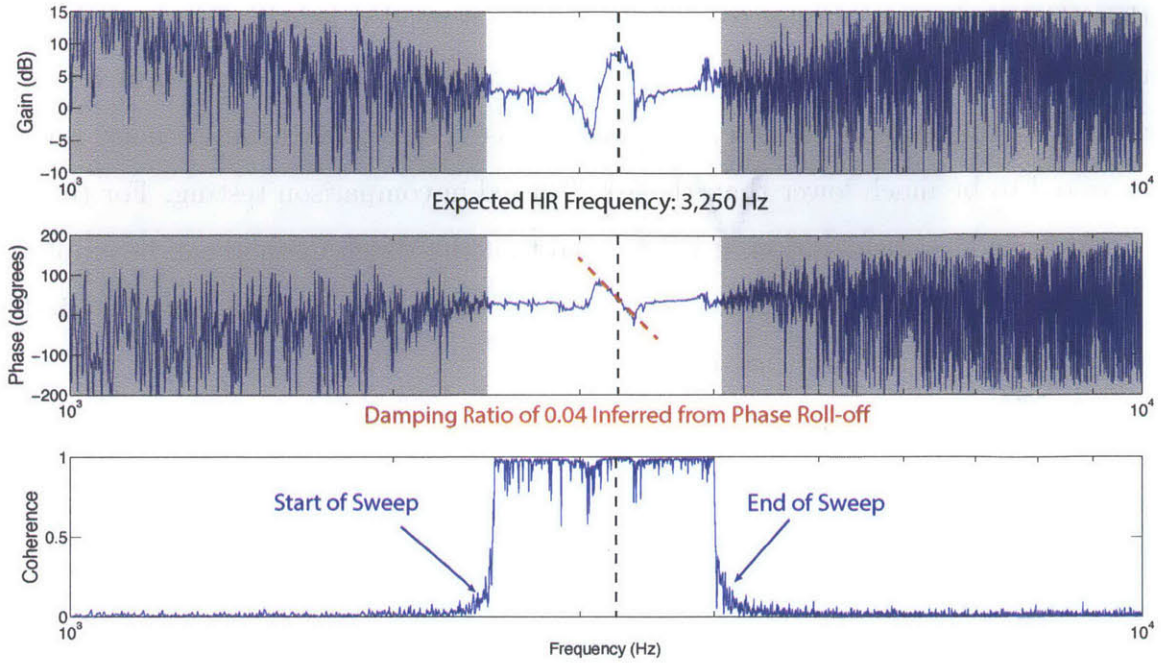

Figure 5-6: Frequency response dynamics for first pressure transducer.

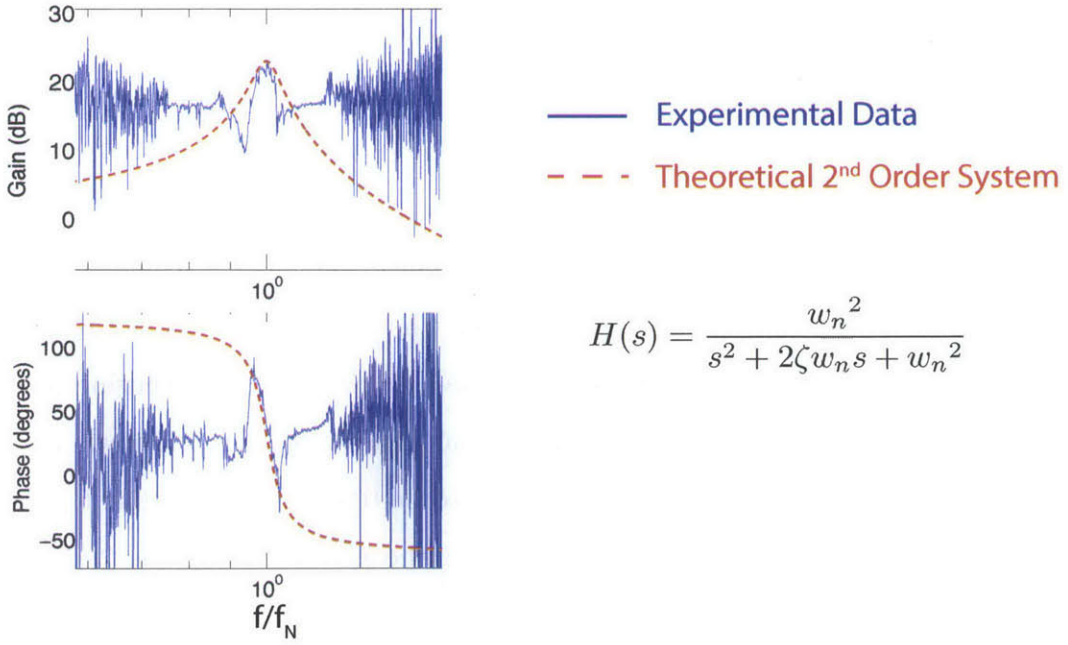

Figure 5-7: Comparison between traditional second order model and HR frequency response dynamics.

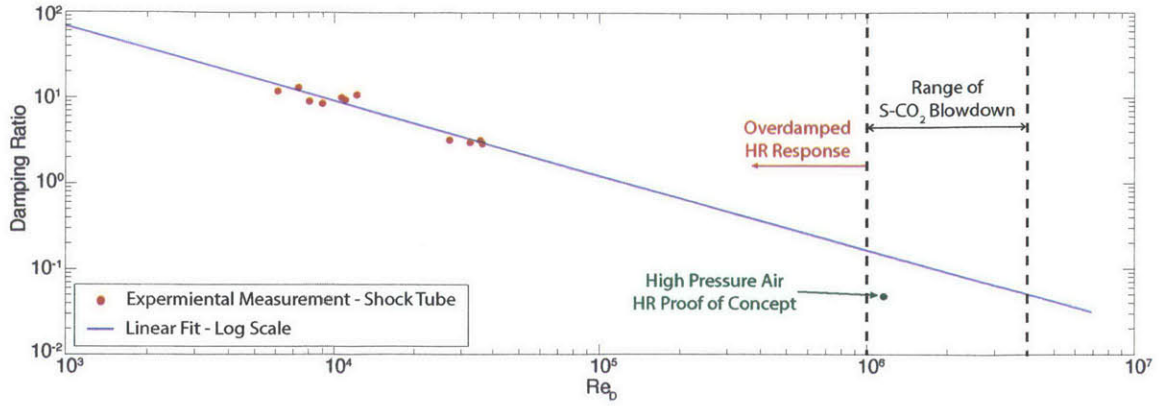

Figure 5-8: HR damping ratio as a function of Reynolds number with high pressure air test.

10 and the resulting figure is shown in Fig 5-8. The difference between the estimated scaling curve and damping ratio from the high pressure tests was 0.07, corresponding to a relative error of 63%. The comparison shows that the previous scaling analysis was conservative and suggests that the HR response would remain underdamped at a lower Re.

While Welch's method performed adequately in capturing the HR dynamics for the first HR, it was in an environment where the magnitude of noise was relatively low, as evidenced by the high coherence throughout the chirp frequency range. A comparison with the MATLAB "spa" function was conducted to verify that "spa" captured the same dynamics in the event that a low coherence environment was encountered, as it was shown that "spa" performs better in a high noise environment in the previous analysis. The comparison can be seen in Fig 5-9. Fig 5-9 verifies that "spa" captures the primary features of the HR frequency response dynamics near the HR frequency in a high coherence environment.

For the high pressure air static test, it was observed that the coherence decayed along the converging nozzle, with minimum coherence reached at the nozzle throat. The measured coherences for HR #1 and HR #7 are compared in Fig 5-10. The root cause for the coherence drop is investigated in Section 5.4. Despite the drop in coherence, the Welch method and "spa" function were applied to the throat HR

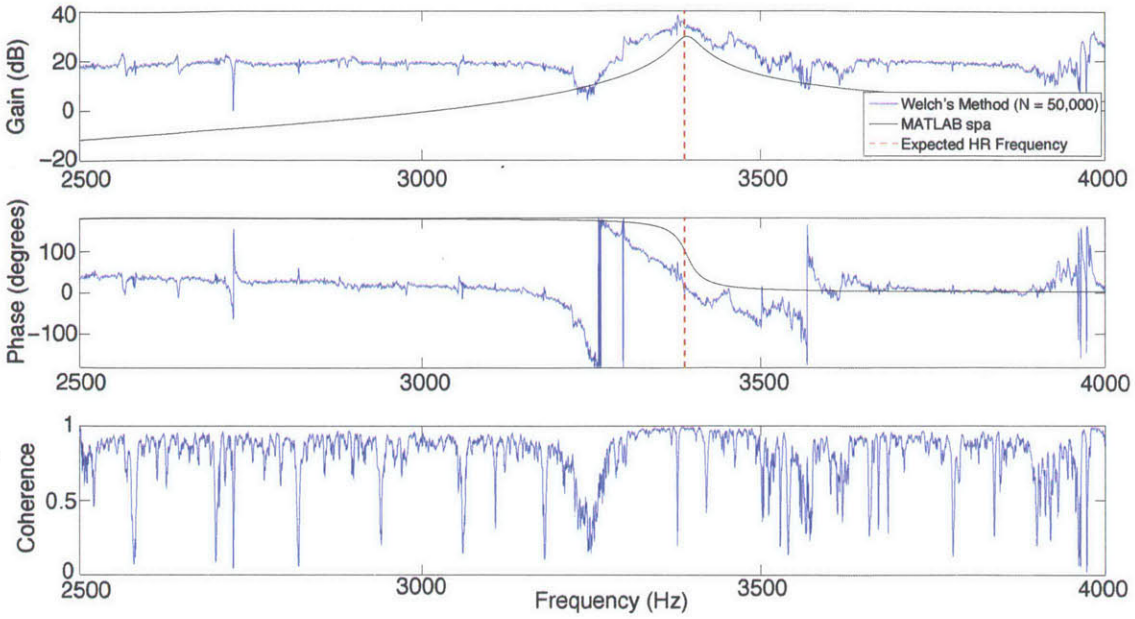

Figure 5-9: Comparison between "spa" and Welch's method for first HR in converging section.

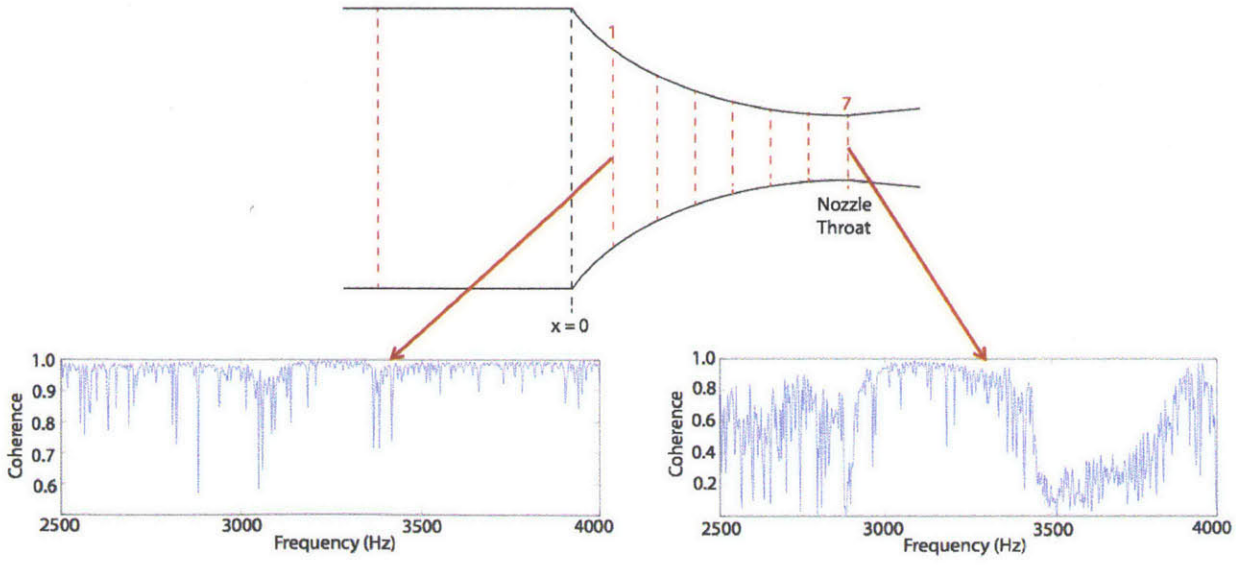

Figure 5-10: Coherence drop along the converging nozzle.

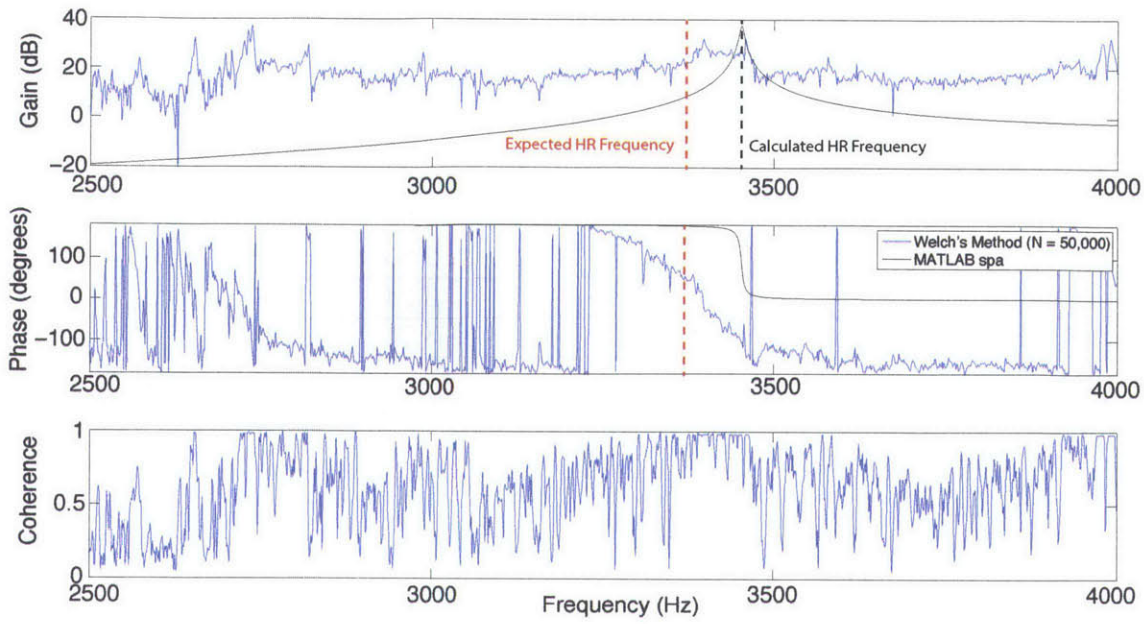

Figure 5-11: Throat HR frequency dynamics calculated with Welch's method and MATLAB "spa" function.

in order to determine if the HR dynamics could still be captured despite the low coherence. The two methods for HR #7 are compared in Figure 5-11. Examination of Fig 5-11 revealed that the drop in coherence greatly affected the calculated HR frequency response dynamics. For the HR #7, Welch's method shows a phase roll-off, but not an evident peak in gain, such that it cannot be confirmed that resonance was achived in the HR. The "spa" function performed slightly better, showing both a phase roll-off and gain peak, but offset from the expected HR frequency. The relative error between the HR frequency calculated by "spa" and the expected HR frequency,

$$Error = \frac{|f_{spa,calculated} - f_{HR,expected}|}{f_{HR,expected}}, \tag{5.13}$$

are tabulated in Table 5.1 for each HR. The average error of the "spa" function, and thus speed of sound, was 1.85 percent, with error increasing through the converging nozzle. The increase in "spa" error corresponds to coherence drop through the nozzle and further investigation of the relationship between error and coherence is required.

While the "spa' function showed potential in capturing the HR dynamics despite low coherence, the lack of agreement between the two methods suggests that further

Helmholtz Resonator	Relative Error (%)
0	0.89
1	0.28
2	0.62
3	1.34
4	1.92
5	2.85
6	3.24
7	3.71

Table 5.1: Relative error of the MATLAB "spa" function for HR frequency calculation.

investigation is required it can be reliably employed in low coherence enviroments.

5.4 Investigation of Coherence Reduction in Nozzle Test Section

An investigation into the drop of coherence along the converging nozzle was conducted in order to determine a) if the coherence drop could be mitigated and b) the root cause of coherence drop for future nozzle designs. The primary cause for coherence drop was deemed to be inadequate forcing of HR. With forcing accomplished by an acoustic actuator (speaker), the acoustic properties of the full nozzle test section geometry were the primary focus of the investigation, with special consideration placed on the possibility of attenuated frequencies as a result of discontinuities in the geometry. Several sources of attennuation were identified, including acoustic reflections, coupled geometric effects, and attenuation characteristics of individual components. Nozzle geometry and sources of acoustic attenuation are identified in Fig 5-12. To investigate the acoustic attenuation properties of the geometry and the effect of changes in geometry on the acoustic transmission properties of the piping, the transmission matrix approach described in [7] is taken. The following assumptions and model simplifications were made:

- Flow through the model and perturbation transmission assumed to be a 1-D

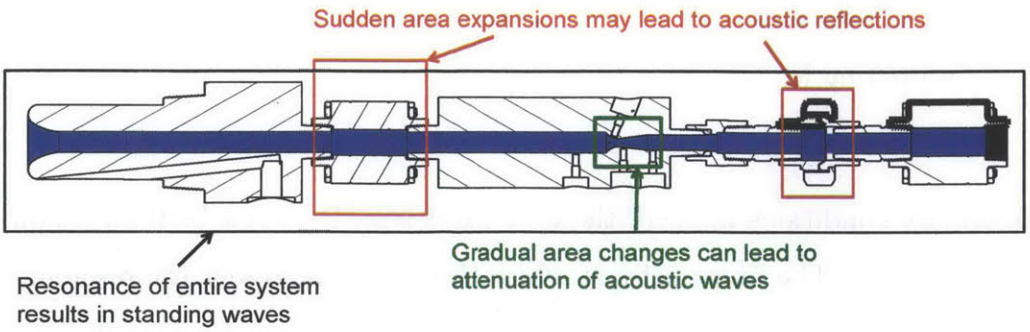

Figure 5-12: Geometric focus of acoustic transmission investigation.

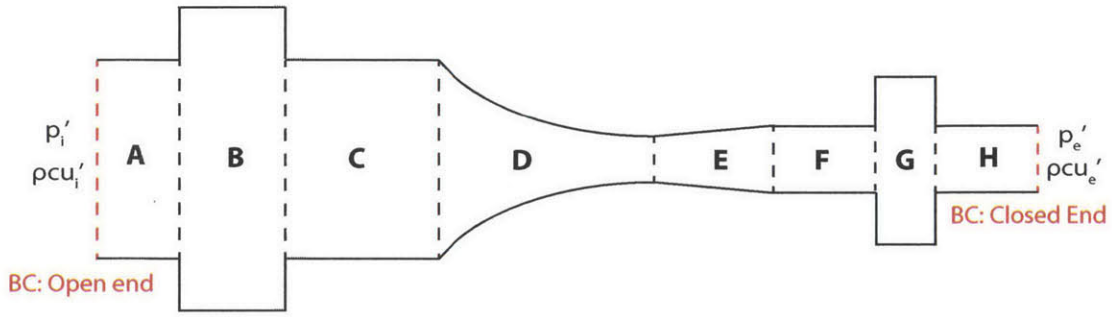

Figure 5-13: 1-D transfer matrix model of piping and boundary conditions.

- Second order terms are neglected
- Converging nozzle area change is approximated by an inverse exponential area decrease with axial distance:

$$A(x) = A_0 e^{-\alpha x}. \tag{5.14}$$

A transmission matrix was constructed for each of the individual sections and the frequency-dependent properties of the resulting transfer matrix for the piping was investigated. The transfer matrix model, boundary conditions and sections modeled are shown in Fig 5-13. The resulting transfer matrix is denoted as P and the resulting

equation balance for pressure and velocity perturbations with boundary equations applied is represented by Eq 5.15.

(5.15)

With the boundary conditions applied, the first coefficient, P_{11} must be 0 for a non-trivial solution to exist. The frequencies at which this occurs represent the resonance frequencies of the system. From the formulation of Eq 5.15, it can be seen that frequencies at which high values of P_{11} occur are attenuated by the system as small pressure perturbations at the inlet are reduced by the exit of the domain. The value of P_{11} over the frequency range of interest was investigated using actual values for area ratios and lengths. This P_{11} spectrum was also constructed for a straight, constant area duct of equal length for comparison. The P_{11} spectra for the straight duct model and actual geometry are compared in Fig 5-14. From Fig 5-14, it can be seen that while the real geometry model shares most of the resonance frequencies as the straight duct model, the peaks in magnitude of P_{11} are much greater within the 2000-4000 Hz frequency range (same range as the static high pressure air test), indicating that the pressure perturbations perceived by the HRs are much lower in this frequency range compared to other frequencies. Due to the muffling action of rapid area changes, it was hypothesized that the flow area discontinuities were responsible for the poor acoustic transmission of frequencies in the range of interest. In order to investigate the transmission properties of the area changes, the transmission coefficient spectra of each major area change (indicated by components B and G in Fig 5-13) was calculated. The transmission coefficient spectra for the upstream valve (B) and downstream area change (G) are shown in Fig 5-15. Fig 5-15 shows that the upstream area change (B) has a transmission coefficient that is close to unity across the frequency range of interest, indicating that it had a minor effect on acoustic transmission through the piping. In contrast, the downstream area change (G) has a low transmisson coefficient across the frequency range of interest, indicating that most of the acoustic energy is reflected instead of transmitted across the area change. The primary consequence of the acoustic reflection is possible interference

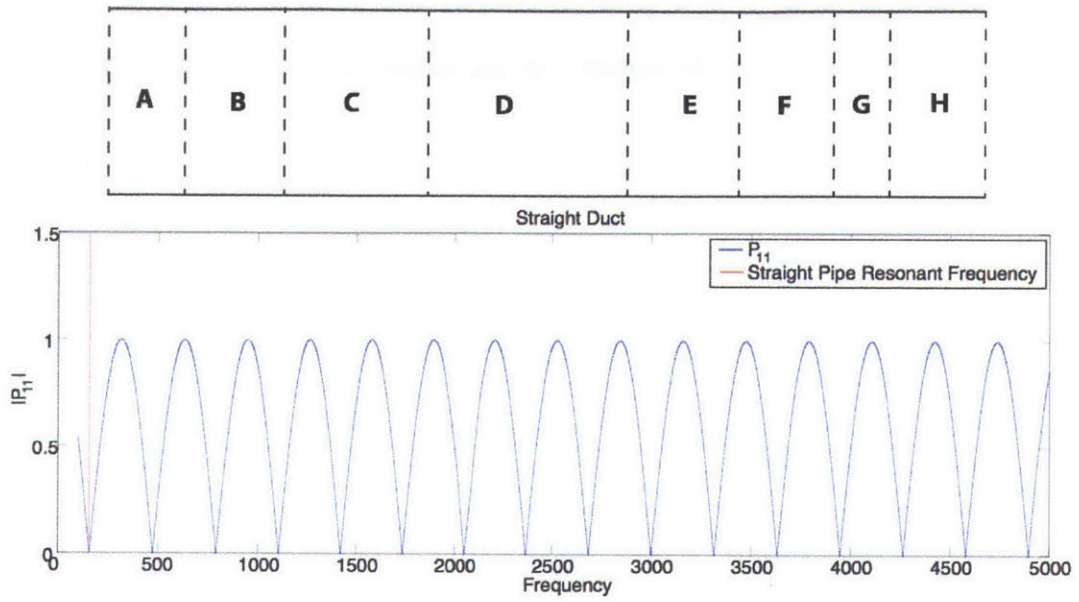

(a) P_{11} spectrum for straight duct model.

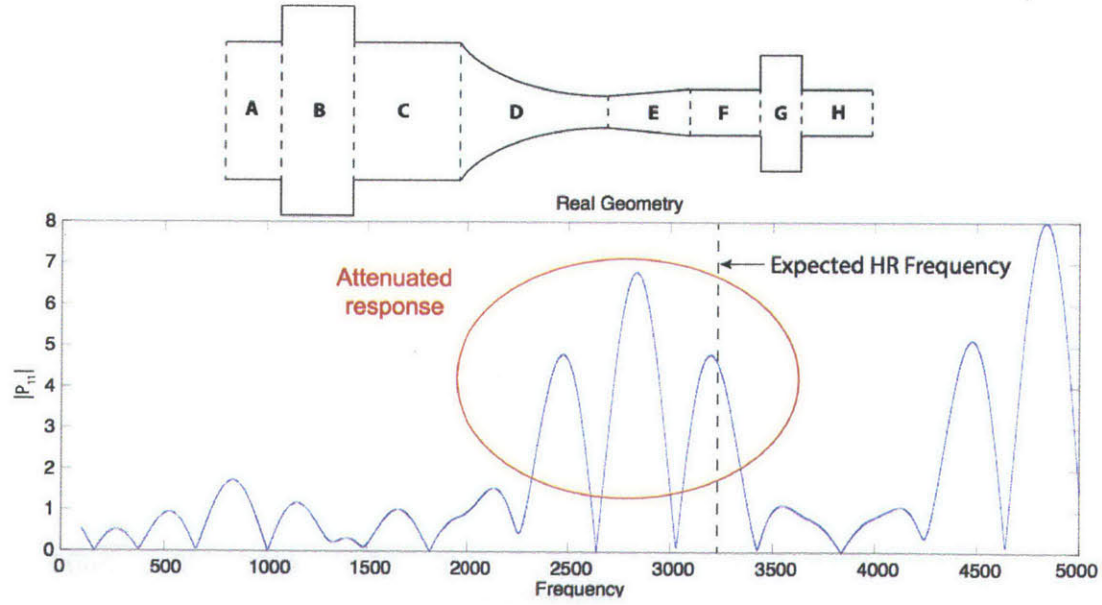

(b) P_{11} spectrum for actual geometry model.

Figure 5-14: P_{11} spectrum for straight duct and actual geometry models.

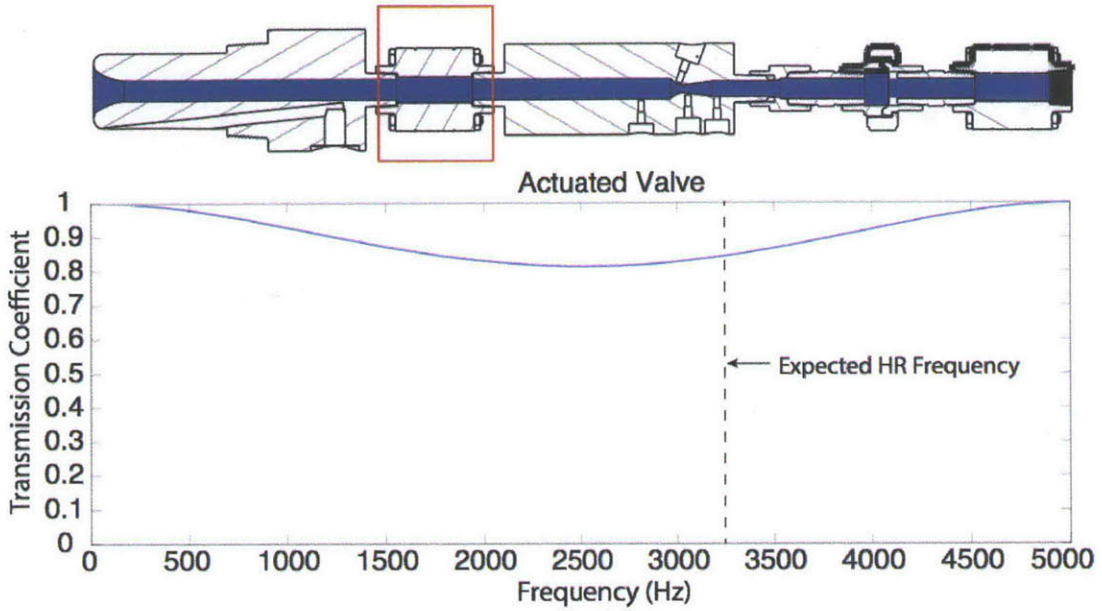

(a) Transmission coefficient spectrum for upstream valve (B).

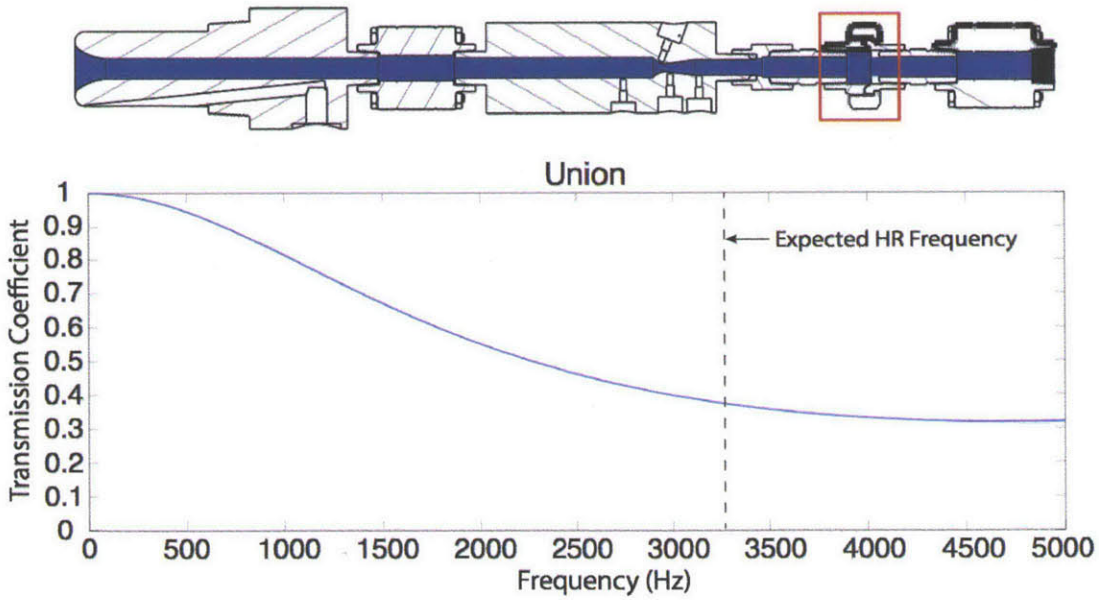

(b) Transmission coefficient spectrum for downstream area change (G).

Figure 5-15: Transission coefficient spectrum for components B and G.

of the generated acoustic signal in the converging nozzle, which may have lead to a decrease in acoustic power felt by the HRs and low coherence. Further experimental investigation, including removal of rapid area changes that result from geometric mismatches is required in order to conclude that the area changes are the source of low coherence in the signal felt by the HRs in the converging nozzle. This is part of future work.

5.5 Conclusion

The Helmholtz resonator speed of sound measurement method shows potential for use in high speed flow situations, however several important challenges remain before it can be successfully implemented. First, the acoustic transmission properties of the duct geometry where the HR method is being implemented must be investigated to ensure that the HR excitation signal can reach the HRs with sufficient power, or else they may not be excited sufficiently. Second, if a low signal-to-noise ratio is observed and low coherence is unavoidable, an effective and reliable method of signal processing must be found in order to implement the HR method. Welch's method and especially the Blackman-Tukey method show promise in low-coherence environments and may represent acceptable signal processing options, however further investigation is necessary. Finally, the HR must be designed to ensure that its response will be underdamped within the frequency range of interest, with the Reynolds number being the key factor affecting the HR damping ratio.

Chapter 6

Experimental Assessment of Condensation Effects in Supercritical CO_2

Currently, there is a lack of experimental studies on the condensation of supercritical CO_2 at high speed. Purely numerical studies are insufficient in determining the effects of condensation of a fluid during high-speed expansion because inaccuracies in the metastable state characterization can result in poor estimation of condensation onset location and large departure from physical behavior. While several methods of modeling the thermodynamic properties of the CO_2 metastable state show promise, such as a cubic extrapolation of the thermodynamic fluid properties into the two-phase region [5], experimental verification of these models has yet to be demonstrated. An experimental investigation of condensation through blowdown tests was carried out at supercritical inlet conditions both away and near the critical point to determine condensation onset in high-speed flow of CO_2. Charge conditons were set to values representative of the inlet conditions in current and future S-CO_2 compressors and such that the two-phase region is reached by the nozzle throat at sonic conditions.

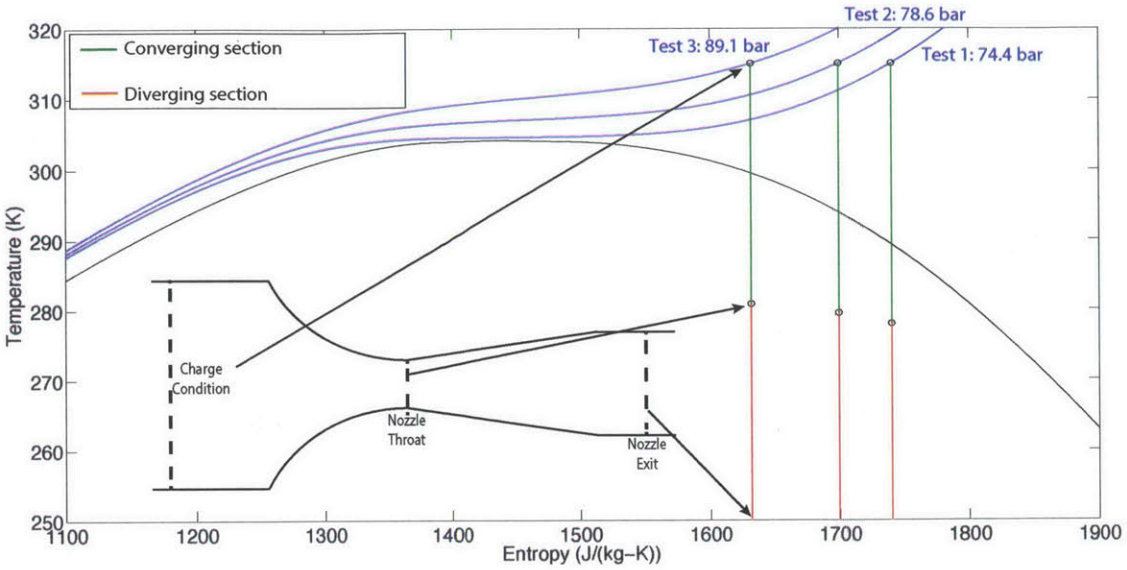

Figure 6-1: Charge tank, estimated nozzle throat, and estimated nozzle exit conditions for first three blowdown tests.

6.1 Experimental Test Cases

The charge conditions for the blowdown tests are shown in Table 3.1. Charge temperature was kept constant at 315 K and charge pressures were moved successively closer to the critical point, at 74.4 bar, 78.6 bar, 89.1 bar, and 95.7 bar, referred to as blowdown tests 1, 2, 3 and 4 respectively. Blowdown tests 1 - 3 were considered away from the critical point while test 4 was considered near the critical point. Inlet, throat, and estimated nozzle exit conditions for tests 1 - 3 are shown in Fig 6-1. Estimations of nozzle throat and exit conditions are determined via Eqn 3.1 and the real-gas, constant n_s, corrected mass flow relation,

$$\frac{\dot{m}\sqrt{Z_t R T_t}}{A p_t \sqrt{n_s}} = M(1 + \frac{n_s - 1}{2} M^2)^{\frac{-n_s-1}{2(n_s-1)}}, \tag{6.1}$$

with the value of n_s equal to the charge value used in the calculation. The assumption of constant n_s was shown have an error less than 1% away from the critical point, with the error increasing from 1% to over 7% near the critical point in [5]. Measured charge, throat, and estimated exit conditions for blowdown test 4 are shown in Fig

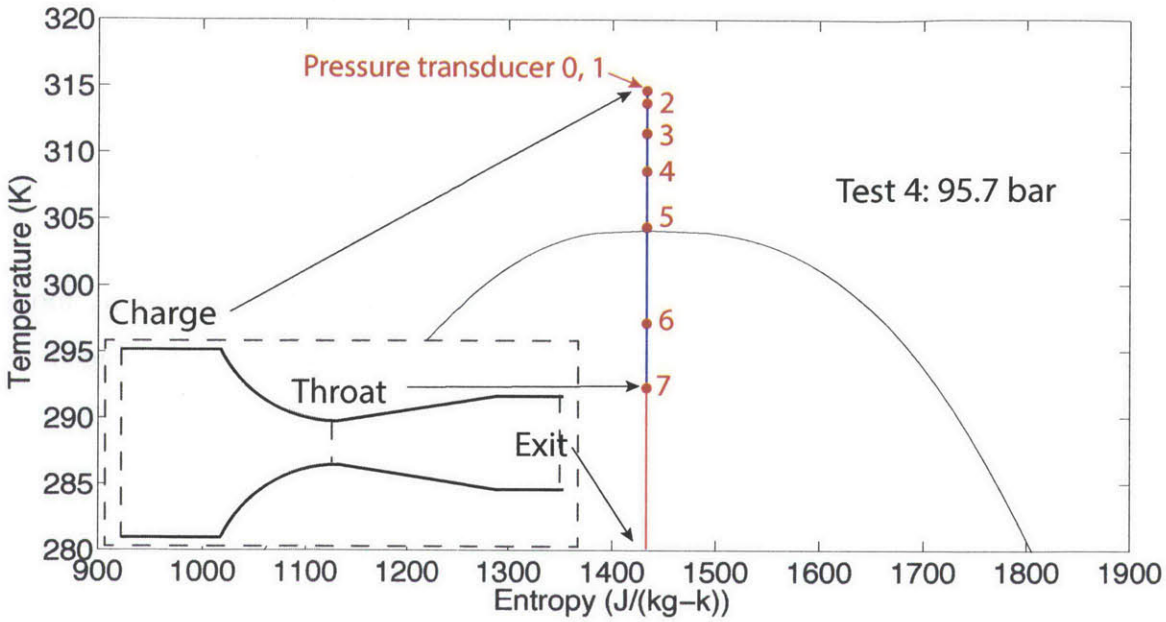

Figure 6-2: Expansion from charge conditions to throat conditions for blowdown test 4.

6-2. All charge conditions were set such that sonic conditions at the nozzle throat were reached in the two-phase region.

6.2 Isentropic Expansion Assessment

As mentioned in Section 1.4, condensation detection relies on detection of static pressure changes in nozzle pressure distribution when compared to the isentropic nozzle pressure distribution. Isentropic pressure distributions used in the analysis are estimated by the following models:

1. A constant n_s, 1-D theoretical model based on a combination of Eqs 3.1 and 6.1,

2. A variable n_s, 1-D numerical model based on Continuity and the First Law of Thermodynamics and utilizing the SW EOS,

3. Two-phase numerical calculations conducted in CFX with the SW EOS and its extrapolation scheme described in Section 2.3.

The simple constant n_s model is only applicable in regions where the change in n_s between charge and throat conditions is less than 6%, corresponding to an error of less than 1% [5]. In regions where the change in n_s is roughly 20%, the error of the model rises to more than 7% [5]. Thus, the use of the constant n_s model is limited to the blowdown tests away from the critical point (tests 1 - 3).

The variable n_s model was developed to improve upon the constant n_s model for blowdown test 4, where n_s changes exceeded 20%. The model leveraged the experimental measurements as much as possible and utilized the SW EOS when required. The following assumptions were made in the model

- Isentropic expansion from charge tank to nozzle throat,
- 1-D flow within the converging nozzle.

The model is governed by continuity and the first law of thermodynamics with a mass flow rate input for pressure distribution calculation. Input mass flow rate was derived from the experimental measurements. To calculate the mass flow rate through the nozzle, the flow velocity and density at each measurement location were required with flow velocity calculated through the first law with no heat transfer, such that,

$$h_{total} - h_{static} = \frac{v^2}{2}. \tag{6.2}$$

Enthalpy and density at the measurement locations were calculated through the SW EOS by utilizing the static pressure measurements and calculated charge tank entropy (which is constant throughout the nozzle). The mass flow rate through the nozzle,

$$\dot{m} = \rho v A, \tag{6.3}$$

was calculated for each measurement point, with the averaged mass flow rate value used in the model. Calculation of thermodynamic properties in the nozzle was accomplished by iteration of enthalpy and density (linked through the SW EOS) at each nozzle axial location until the mass flow value matched the input value within

0.1 %. Due to reliance on the SW EOS, the variable n_s model is only applicable up to the critical point.

The two-phase numerical calculation tools described in Chapter 2 were used separate 3-D flow effects as a result of nozzle geometry when compared to the 1-D, constant and variable n_s models. Due to reliance on an extrapolation scheme to provide the metastable properties of CO_2, the numerical calculations are limited by the regions in which the extrapolation scheme is valid. Away from the critical point, the extrapolation scheme is shown to perform adequately for small extrapolations into the two-phase region, while large extrapolations were found to result in numerical instabilities. Therefore numerical calculatioons are limited to the region away from the critical point while further assessment is required near the critical point. Near the critical point, the metastable extrapolation is challenging due to sharp gradients in the thermodynamic properties at the critical point greatly influencing the cubic extrapolation scheme. The change in c_p and speed of sound along an isentrope from a temperature of 315 K to the critical point (304.1 K) are plotted in Fig 6-3. A comparison between the numerical calculation and experimental measurements up to the critical point is shown in Fig 6-4. Outside of the two-phase region, the numerical calculation shows good agreement with the experimental measurements, verifying that the numerical implementation of the SW EOS outside of the two-phase region near the critical point.

6.3 Blowdown Test Results

6.3.1 Away from the Critical Point

Due to the issues with the Helmholtz resonator speed of sound measurement method mentioned in Section 5.5., only static pressure measurements were taken along the converging nozzle during the blowdown tests. The static pressure distributions in the converging nozzle for blowdown tests 1, 2, and 3 are shown in Figs 6-6, 6-7 and 6-8 respectively, along with the 1-D, constant n_s theoretical model. A numerical simu-

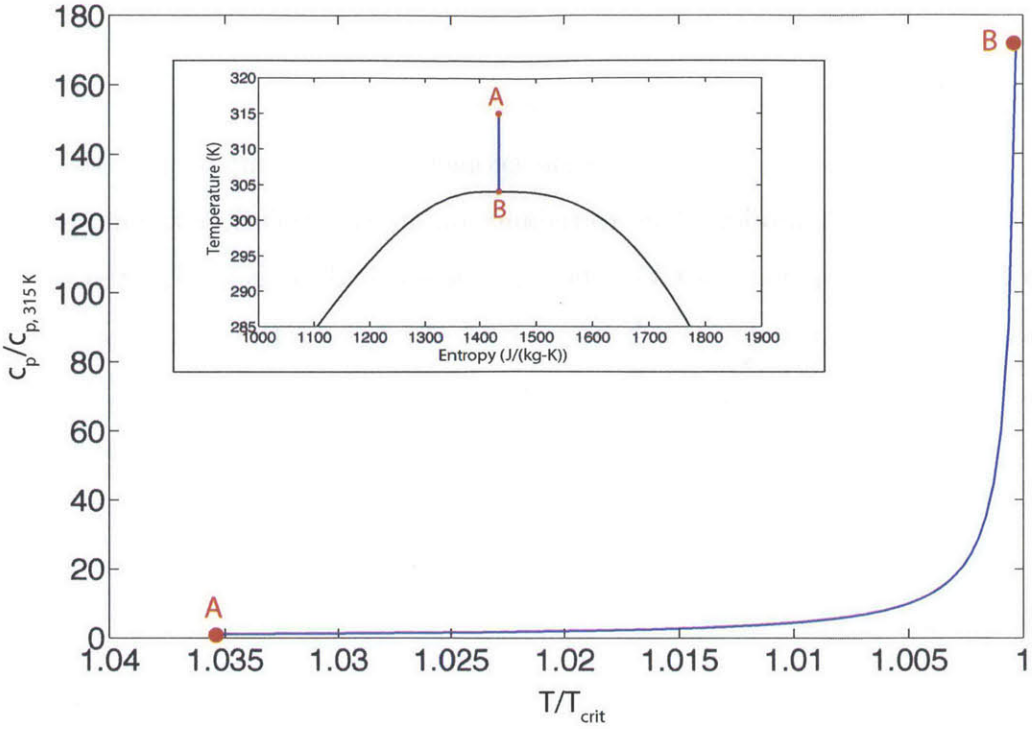

(a) Value of c_p approaching the critical point.

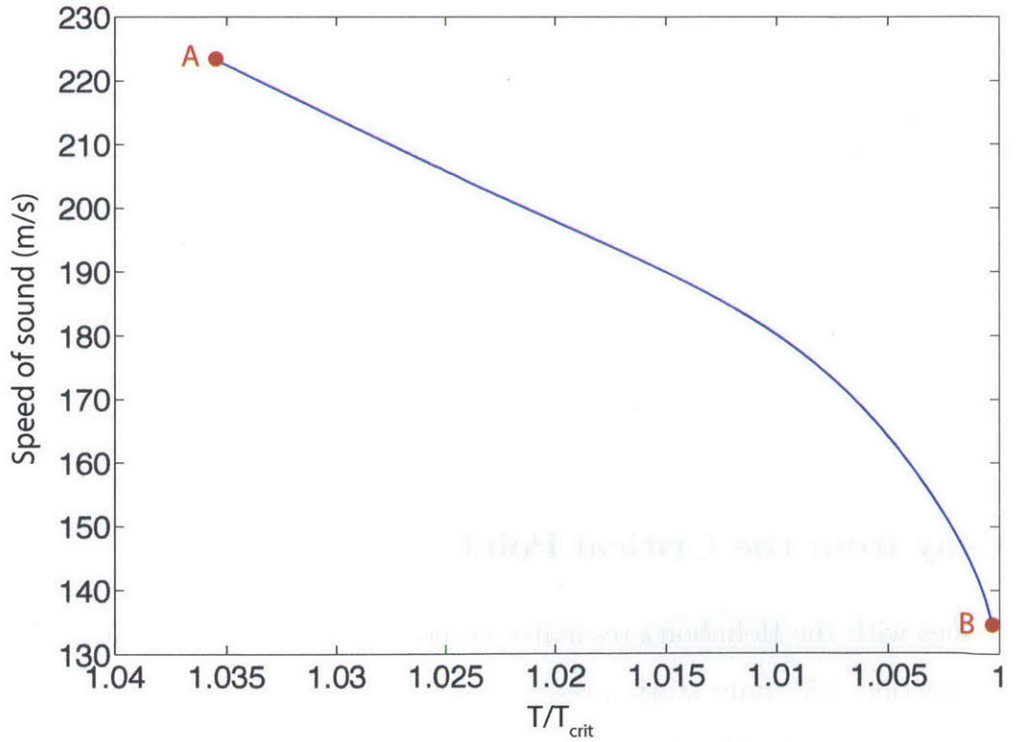

(b) Value of speed of sound approaching the critical point.

Figure 6-3: Value of c_p (a) and speed of sound (b) approaching the critical point.

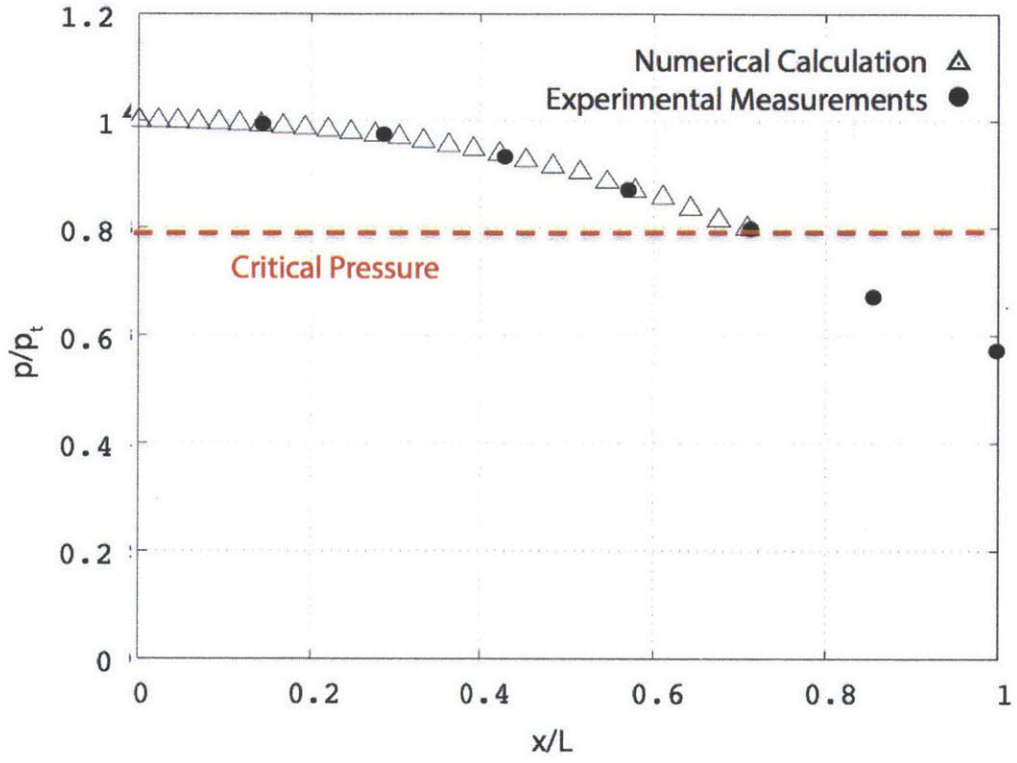

Figure 6-4: Comparison between the numerical calculation and experimental measurements for test 4. (Courtesy of Dr. C. Lettieri)

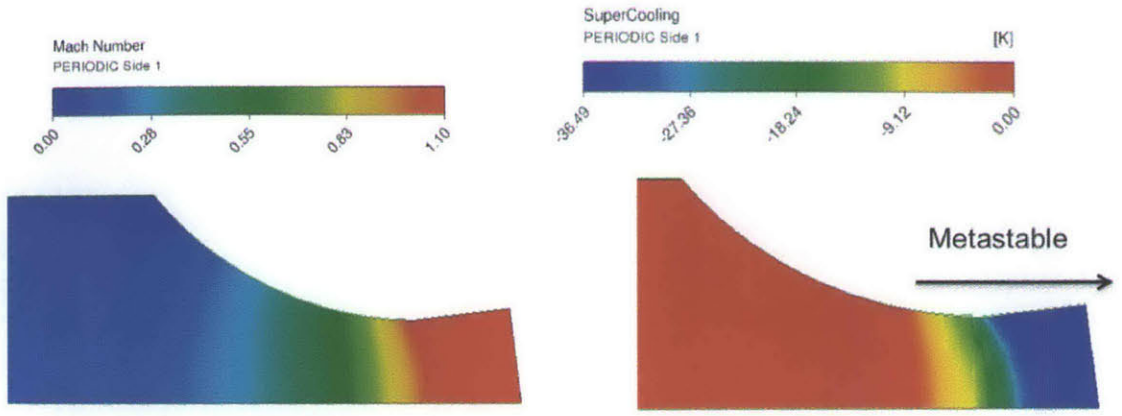

Figure 6-5: Numerical simulation of 89.1 bar blowdown test (3). (Courtesy of Dr. C. Lettieri)

lation of blowdown test 3 was conducted for comparison in Fig 6-8. The nozzle exit pressure was set to atmospheric conditions such that the CO_2 temperature drops below the triple point and outside the range of the SW EOS. For such values, the cubic extrapolation scheme yields significant challenges and possibly numerical instabilities. Therefore, the nozzle diverging section was intentionally truncated in the calculations to ensure convergence. The numerical calculation results for Mach number and supercooling, ($T - T_{saturation}$), are shown in Fig 6-5. The numerical simulation shows only a negligible fraction of liquid CO_2 despite up to 36 K of supercooling, suggesting that condensation is not expected in blowdown test 3. Furthermore, the absence of condensation is supported by investigation of the timescales in the numerical simulation, which revealed that $\tau_{cl} \sim 10^{-4}$ in the converging section, suggesting that the flow did not remain in the supercooled region long enough for nucleation to occur. The measured wall static pressure distributions are in good agreement with the theoretical 1-D estimates as well as the numerical calculation, with deviations of most measurements less than 0.5%, with the exception of the second pressure measurement, which has a deviation of about 3%. The larger deviation is likely a result of small differences in nozzle geometry and model used in the numerical calculation due to manufacturing tolerances. Additionally, the agreement between the numerical calculation and experimental measurements suggest that the metastable extrapolation

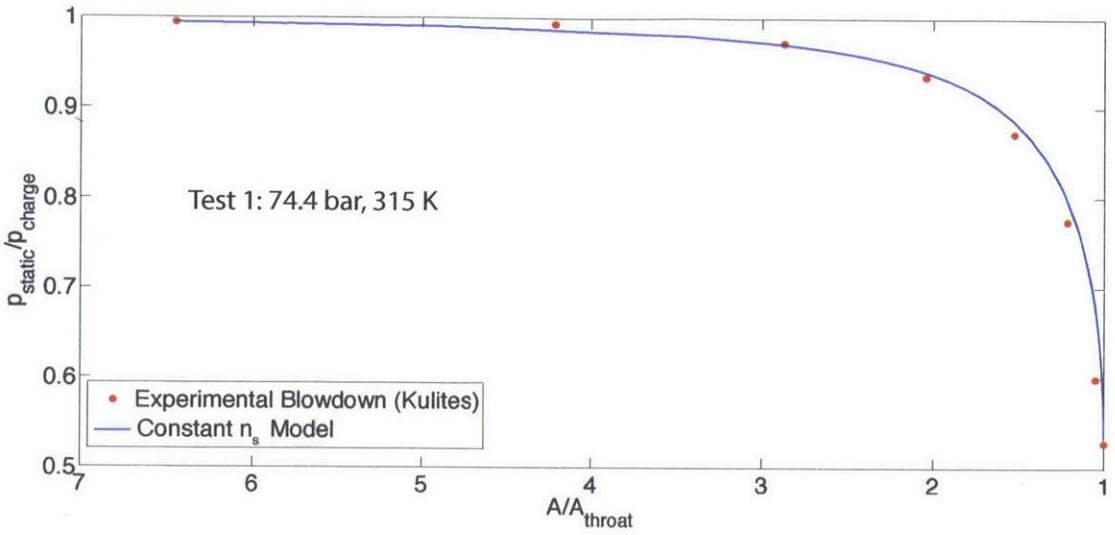

Figure 6-6: Experimental and theoretical 1-D pressure distributions for the 74.4 bar, 315 K blowdown test in the converging nozzle.

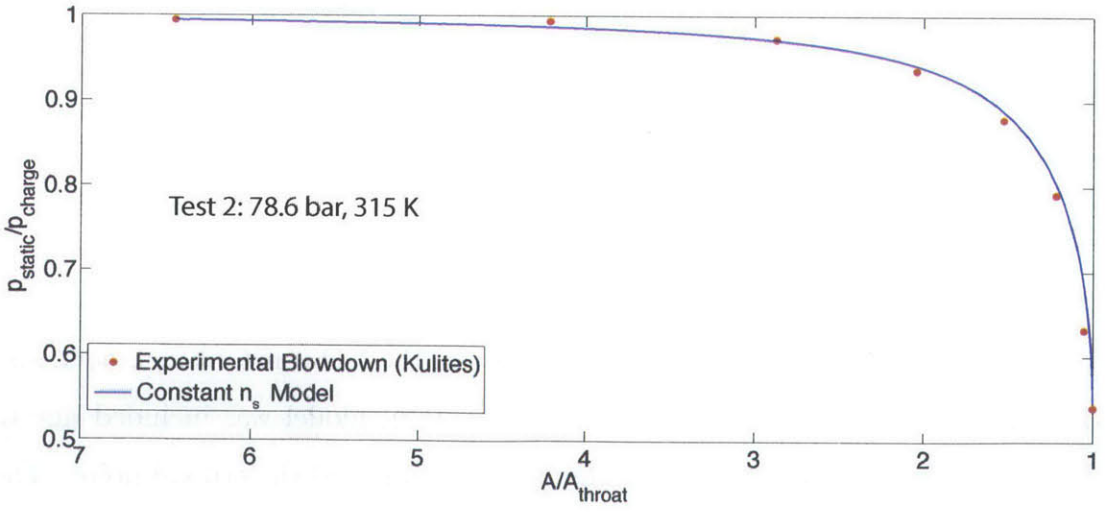

Figure 6-7: Experimental and theoretical 1-D pressure distributions for the 78.6 bar, 315 K blowdown test in the converging nozzle.

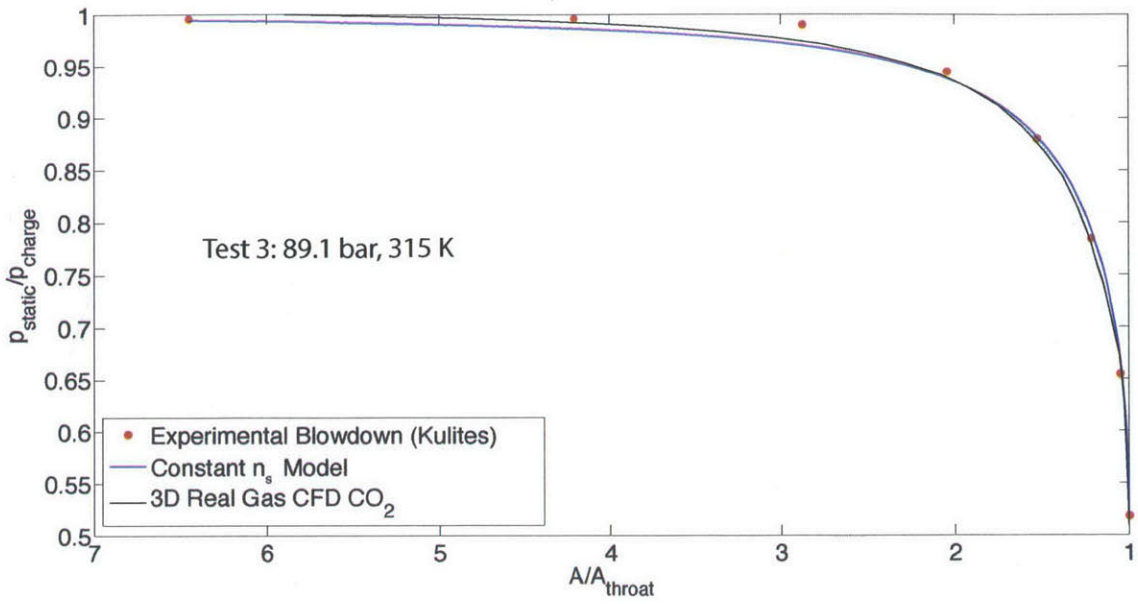

Figure 6-8: Experimental, numerical and theoretical 1-D pressure distributions for the 89.1 bar, 315 K blowdown test in the converging nozzle.

scheme performs well away from the critical point.

6.3.2 Near the Critical Point

Fig 6-9 illustrates the measured pressure distributon, the 1-D constant n_s model, and variable n_s model for blowdown test 4. The variable n_s model was included due to a difference of 1.8 (60%) in n_s between charge conditions and the critical point. The experimental measurements for the test near the critical point show poor agreement with the constant n_s model, with deviations of up to 10%, validating the findings in [5]. In contrast, the measurements show good agreement with the variable n_s model up to the critical point, with deviations of less than 3%.

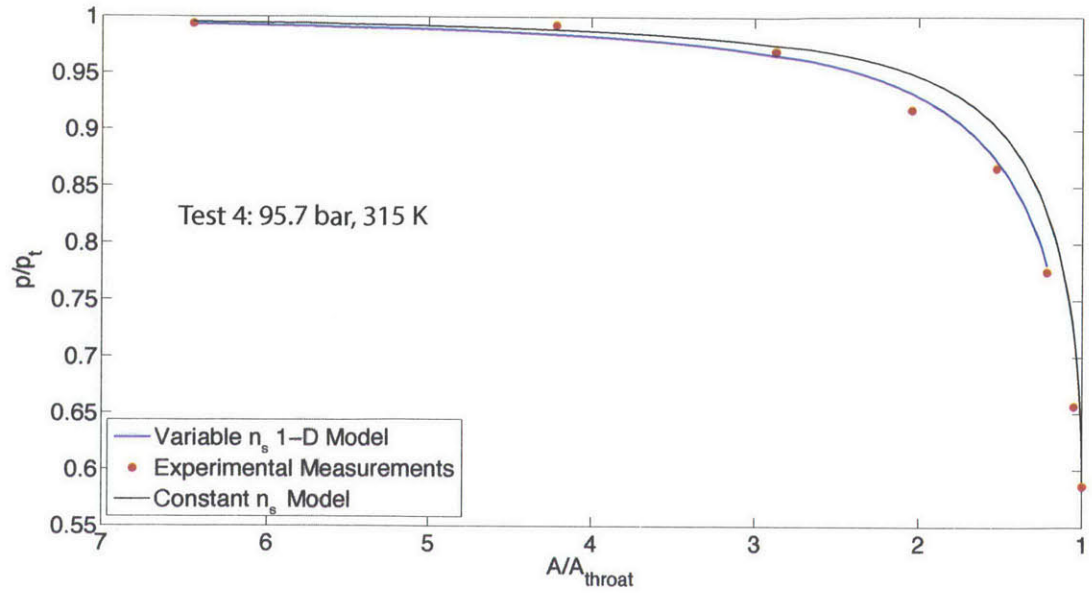

Figure 6-9: Real-gas 1-D model nozzle pressure distribution compared to experimental measurements for the 95.7 bar, 315 K, blowdown test.

6.4 Discussion

6.4.1 Expansion Away from the Critical Point

The close agreement between the 1-D estimates, numerical calculation, and experimental measurements suggest that CO_2 condensation onset does not occur during rapid expansion to sonic conditions away from the critical point, despite expansion into the two-phase region. To verify, and to quantify the potential changes in static pressure distribution due to condensation, a 1-D compressible flow analysis with heat addition was conducted with blowdown test 3. For the nozzle conditions in test 3, the equilibrium moisture content near the throat thermodynamic conditions is 30%. Thus it was safe to assume conensation onset of 30% moisture in the influence coefficient based approach. The compressible heat addition model, along with the previous findings are compared in Fig 6-10.

Heat addition due to to condensation with the above assumption, causes thermal choking of the flow before the throat and a corresponding 16% static presure drop near sonic conditions. With both isentropic model deviations and measurement errors

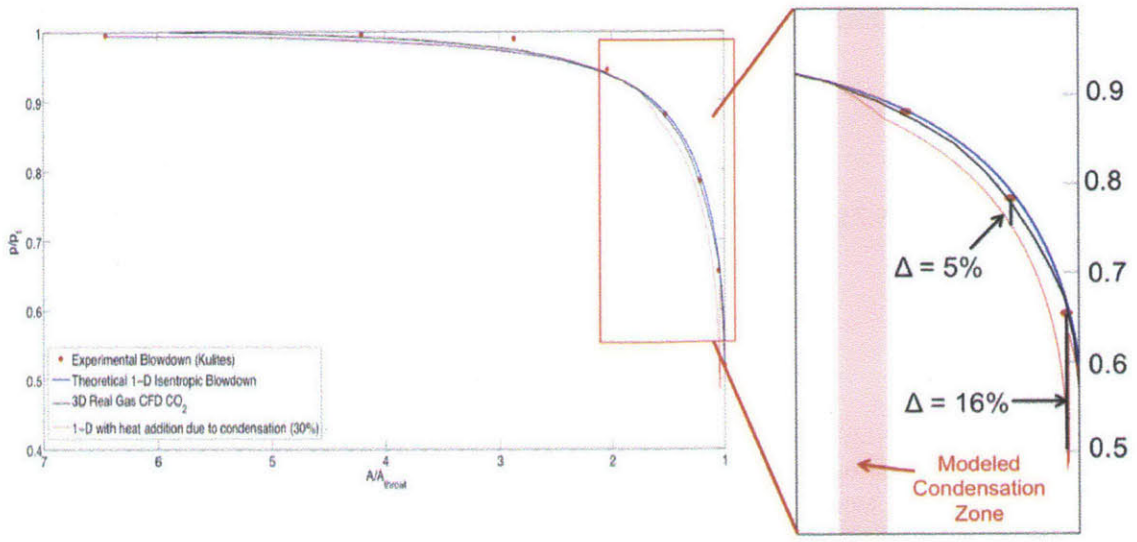

Figure 6-10: Pressure distributions of various models and measurements for blowdown test 3.

much lower than the expected static pressure drop, condensation in the converging section can be ruled out for tests 1 - 3.

With no detectable condensation in the converging nozzle, it is assumed that condensation occurs in the diverging section of the nozzle as supercooling increases further and τ_{cl} moves closer to unity. This assumption is consistent with similar experiments conducted with water steam, where condensation onset is commonly observed at Mach numbers from 1.3 - 1.5 [8]. Validation of this conjecture requires high-resolution measurements in the diverging section of the nozzle and is the subject of future work.

6.4.2 Expansion Near the Critical Point

Near the critical point, real gas effects and two-phase effects are important. Separation of the two effects is required before a condensation assessment can be conducted. The correct extrapolation of fluid properties into the metastable state would allow for quantification of real-gas effects and allow for a condensation assessment to be conducted. A first order estimate was calculated through Eq 3.1 with a linear n_s distribution in the two-phase region. The linear n_s distribution was calculated through

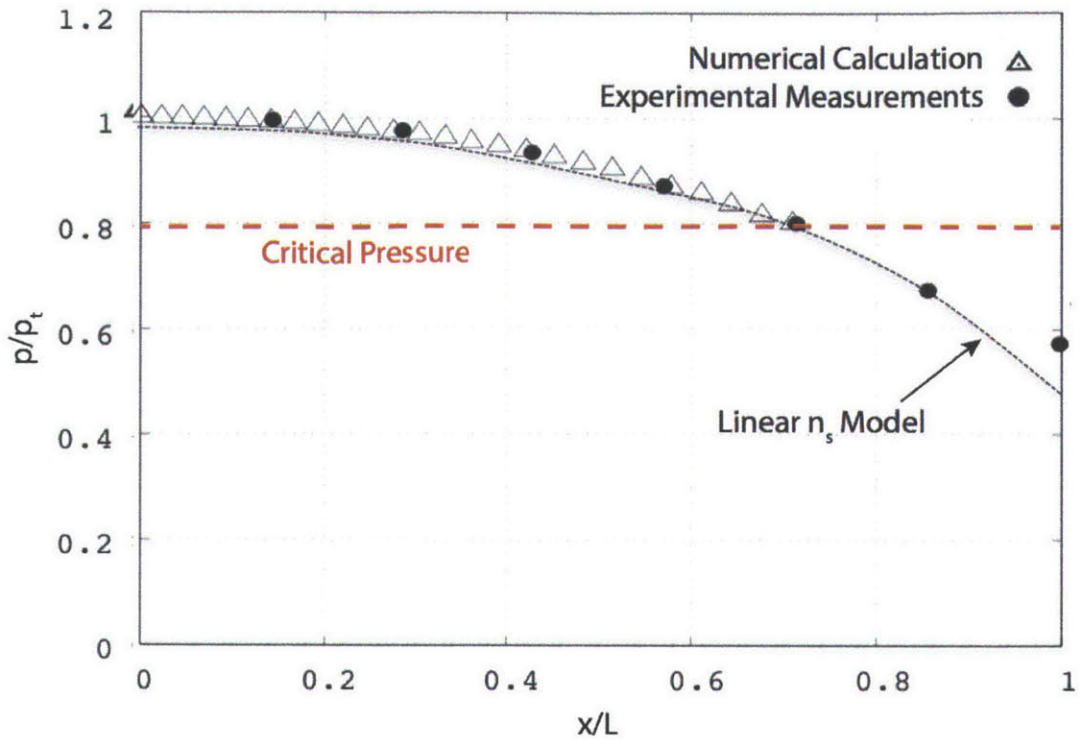

Figure 6-11: Comparison between numerical calculations and experimental measurements for blowdown test 4. (Courtesy of Dr. C. Lettieri)

extrapolation of n_s from outside of the two-phase region. The linear n_s model, experimental measurements, and numerical calculation are compared in Fig 6-11. Inside of the two-phase region, the linear n_s model leads to good agreement between the numerical calculation and experimental measurement for pressure transducer #7 and poor agreement for pressure transducer #8. While the good agreement for pressure transdcuer #7 suggests that the linear n_s model has potential, further experimental investigation is necessary to validate its use and potential implications. Validation requires that the model show good agreement with two thermodynamic properties in the metastable region and is the subject of future work.

Chapter 7

Conclusion and Future Work

This thesis presents a experimental assessment of the possibility of internal flow condensation of supercritical CO_2 during rapid expansion into the two-phase region. While the main focus was on investigation of condensation onset during rapid expansion, a secondary aim was to demonstrate speed of sound measurement through the use of Helmholtz resonators. Experimental investigations of both CO_2 condensation and HR speed of sound measurement method were conducted on a blowdown test-rig with a modular test-section, constructed at the Gas Turbine Laboratory at MIT. The major contributions of both investigations are summarized, followed by recommendations for future work.

7.1 Thesis Contributions

The contributions of this thesis can be summarized into experimental findings related to supercritical CO_2 condensation and methods related to experimental measurements and blowdown test-rig design. The key experimental findings include:

1. Away from the critical point, for S-CO_2 expansion to sonic conditions in the two-phase region, condensation was not observed. The measured pressure distribution showed good agreement ($< 3\%$ deviation) with both the 1-D isentropic, constant n_s model and 3-D, two-phase numerical simulation pressure distributions. Final confirmation of the condensation assessment requires more refined

measurements and confirmation of condensation in the diverging section of the nozzle.

2. For rapid expansion near the critical point, the measured nozzle pressure distribution shows only a small deviation ($< 2\%$) compared to the variable n_s 1-D isentropic model up to the critical point. The extrapolation of the model into the two-phase region is required for an assessment of condensation near the critical point.

3. Demonstration that numerical calculations utilizing SW EOS near the critical point show good agreement ($< 1\%$) with experimental measurements outside of the two-phase region.

The key findings related to experimental measurements, methods, and test-rig design are as follows:

1. The Helmholtz resonator speed of sound measurement method shows promise during high pressure static tests in air. The gain and phase behavior in the frequency domain agrees with the behavior of a underdamped 2nd order TF.

2. Special care must be taken to design the HR neck to ensure an underdamped response. The damping ratio of the HR is directly related to the Reynolds number of the flow within the HR neck, with an underdamped response requiring a Reynolds number of 10^6.

3. Acoustic forcing of the HRs requires sufficient acoustic power to be transferred to the HRs. Sufficient acoustic power transfer requires that the acoustic signal is not attenuated as a result of geometric discontinuities.

4. Demonstration of the viability of a blowdown test-rig to achieve rapid expansion of S-CO_2 over a wide range of charge conditions

7.2 Recommendations for Future Work

For the measured nozzle pressure distributions for the blowdown tests away from the critical point, no condensation was observed within the converging section. However, final confirmation of the findings requires either more refined pressure measurements or optical measurement/confirmation of condensation onset within the diverging section of the nozzle. It is recommended that the modular test section be replaced with a test section with improved measurement capability in order to confirm the condensation assessment presented in this thesis.

Near the critical point, the variable n_s model shows good agreement with the experimental measurements up to the critical point. A condensation assessment near the critical point requires a proper extrapolation scheme of the CO_2 properties into the two-phase region. With the lack of experimental data in this region, detailed experimental measurements of two thermodynamic properties in the metastable region are required to validate any extrapolation scheme. Future blowdown tests should employ a test section that allows for such measurements.

Bibliography

[1] C. F. Delale, G. H. Schnerr, and J. Zierep. Asymptotic solution of transonic nozzle flows with homogeneous condensation. ii. supercritical flows. *Physics of Fluids A (Fluid Dynamics)*, 5(11):2982–2995, 11 1993.

[2] Steven Chu. Carbon capture and sequestration. *Science*, 325:1599, 2009.

[3] Annual energy outlook 2014. Technical report, U.S Energy Information Administration, U.S Department of Energy, Washington, DC 20585, 2014.

[4] James J. Pasch Alan M. Kruizenga Brian D. Iverson, Thomas M. Conboy. Supercritical co2 brayton cycles for solar-thermal energy. *Applied Energy*, 111:957–970, 2013.

[5] Nikola D. Baltadjiev. An investigation of real gas effects in supercritical co2 compressors. Master's thesis, Massachusetts Institute of Technology, 2012.

[6] R. Span and W. Wagner. A new equation of state for carbon dioxide covering the fluid region from the triple-point temperature to 1100 k at pressures up to 800 mpa. *Journal of Physical and Chemical Reference Data*, (6):1509, 1996.

[7] E. M. Greitzer, Choon Sooi Tan, and M. B. Graf. *Internal flow : concepts and applications.* Cambridge, UK ; New York : Cambridge University Press, 2004., 2004.

[8] G. H. Schnerr. Unsteadiness in condensing flow: dynamics of internal flows with phase transition and application to turbomachinery. *Proceedings of the*

Institution of Mechanical Engineers, Part C (Journal of Mechanical Engineering Science), 219(C12):1369–1410, 12 2005.

[9] K.M. Duff. Non-equilibrium condensation of carbon dioxide in supersonic nozzles. Master's thesis, Massachusetts Institute of Technology, 1964.

[10] Klaus H. Lüdtke. *Process Centrifugal Compressors.* Springer-Verlag, 2004.

[11] R.T. Jacobson, S.G. Penoncello, E.W. Lemmon, and R. Span. *Equations of state for fluids and fluid mixtures; Multiparameter Equations of State.* Amsterdam ; New York : Elsevier, 2000., 2000.

[12] Yuri A. Ryzhov, Ul'yan G. Pirumov, and Vladimir N. Gorbunov. *Nonequilibrium Condensation in High-Speed Gas Flows.* Gordon and Breach Science Publishers, 1989.

[13] M.O McLinden E.W Lemmon, M.L Huber. Nist standard reference database 23: Reference fluid thermodynamic and transport properties - refprop. Technical report, National Institute of Standards and Technology, 2010.

[14] W. C. Reynolds and W. M. Kays. Blowdown and charging processes in a single gas receiver with heat transfer. *Transactions of the American Society of Mechanical Engineers*, 80:1160–1168, 07 1958.

[15] Oleg Grigorevich Martynenko and Pavel P. Khramtsov. *Free-convective heat transfer.* Berlin ; New York : Springer, c2005., 2005.

[16] B. S. Petukhov. Heat transfer and friction in turbulent pipe flow with variable physical properties. *Advances in Heat Transfer*, 6:503–564, 1 1970.

[17] W. Melvin Cahoon Gordon P. Blair. Best bell.

[18] Steam turbine performance test codes (ptc 6). Technical report, American Society of Mechanical Engineers, 2004.

[19] Pijush K. Kundu and Ira M. Cohen. *Fluid mechanics.* Amsterdam ; Boston : Academic Press, c2008., 2008.

[20] J. R. Womersley. Method for the calculation of velocity, rate of flow and viscous drag in arteries when the pressure gradient is known. *The Journal of Physiology*, 127(3):553–563, 1955.

[21] Hermann Schlichting and K. Gersten. *Boundary-layer theory.* Berlin ; New York : Springer, c2000., 2000.

[22] Lennart Ljung. *System Identification: Theory for the User.* Prentice Hall PTR, 2 edition, 1999.

[23] P.D. Welch. The use of fast fourier transform for the estimation of power spectra: A method based on time averaging over short, modified periodograms. *IEEE Transactions of Audio Electroacoustics*, pages 70–73, 1967.

[24] Ralph Beebe Blackman and John Wilder Tukey. *The Measurement of Power Spectra.* Dover Publications, Inc., 1958.

[25] Petre Stoica and Randolph Moss. *Spectral Analysis of Signals.* Prentice Hall, 2005.